



# Determining Rare Earth Dopant Concentrations in Optical Fibres and Waveguides

by

**Thinh Bao Nguyen**

**B.Sc.(Hons) Victoria University of Technology**

Submitted for the degree of

**Doctor of Philosophy**

Optical Technology Research Laboratory

Victoria University of Technology

Australia

June, 2004

FTS THESIS

621.36920287 NGU

30001007903851

Nguyen, Thinh Bao

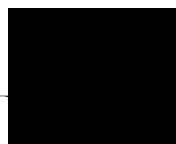
Determining rare earth  
dopant concentrations in  
optical fibres and

I, Think Bao Nguyen, declare that the thesis entitled

**“Determining Rare Earth Dopant Concentrations in Optical Fibres and Waveguides”**

is my own original work, except where specific reference to other authors has been made, and has not been submitted previously, in whole or part, in respect of any other academic award.

Signature \_\_\_\_\_



Date 26<sup>th</sup> July 2004

*For my family.*

*“If the Lord Almighty God had consulted me before embarking on creation I should have recommended something simpler”*

Alphonso X (Alphonso the Wise) 1221-1284

King of Castille and Leon

## ABSTRACT

### Determining Rare Earth Dopant Concentrations in Optical Fibres and Waveguides

by Thinh Bao Nguyen

B.Sc.(Hons) Victoria University of Technology

Principal Supervisor:

Dr. Gregory Baxter

The fluorescence lifetimes of rare earth-doped fibres and waveguides were studied in this thesis to determine whether the fluorescence lifetime could be used as a means for determining the rare earth concentrations. The performance of rare earth-doped devices is dependent on many parameters, including the dopant concentration. Accurate modelling of such devices require knowledge of the dopant concentrations and/or dopant distribution. Current techniques for determining dopant concentration are applicable to bulk samples and fibre preforms but can not be applied to fibres due to fibre size and resolution limits.

A technique was proposed by researchers within this research group that used the fluorescence lifetimes of praseodymium-doped fibres. Their work found that the lifetime of the lifetime of praseodymium-doped ZBLAN fibre increased linearly with praseodymium concentration. These results showed promise in the use of fluorescence lifetimes as a method for determining both the absolute concentration as well as imaging the concentration profile using confocal microscopy. This technique is explored further in this work to see if it could be applied to other rare earths. The technique relies on the change in the fluorescence lifetime as a function of concentration due to cooperative energy transfer between neighboring ions. Rate equations were used to model the behavior of the fluorescence lifetime. Three dopant sample sets were investigated; erbium-doped silica fibres, ytterbium:erbium-codoped silica fibre preforms and praseodymium-doped fluoride glass was revisited.

In erbium-doped silica fibre, the 1535 nm and 540 nm fluorescence was investigated. For the 1535 nm fluorescence, a model based on rate equations was developed that described the lifetime of this fluorescence as a function of both the concentration and pump power. The cooperative up-conversion coefficient that described the concentration dependence was obtained and ranged from  $1.8 \times 10^{-24}$  to  $9.97 \times 10^{-23}$  m<sup>3</sup>/s for erbium concentrations from  $1.83 \times 10^{24}$  to  $7.92 \times 10^{25}$  ions/m<sup>3</sup> respectively. It was found that the fluorescence lifetime did not change with concentration for concentrations below  $5 \times 10^{25}$  ions/m<sup>3</sup>. However there was a logarithmic decrease in the lifetime at higher concentrations, above  $5 \times 10^{25}$  ions/m<sup>3</sup>. The model also found a similar dependence of the fluorescence lifetime on pump power. The lifetime was not affected by pump power at low concentrations but was reduced with pump power at high concentrations. It was concluded that the 1535 nm fluorescence lifetime in erbium-doped silica could not be used as a means for determining concentration as the lifetime did not vary as a function of concentration for all concentrations of interest.

For the 540 nm fluorescence, experimental results indicated no correlation between the fluorescence lifetime and erbium concentration. Spectroscopic inspection of the energy levels of erbium-doped silica showed no appreciable cooperative energy transfer effects involving the  $^4S_{3/2}$  excited state where the 540 nm fluorescence originates from, and thus, no concentration-dependent effects on the fluorescence lifetime.

In ytterbium:erbium-codoped silica fibre preforms, the 1032 nm ytterbium fluorescence was investigated. The investigation found that the 1032 nm fluorescence lifetime exhibited quadratic behavior with concentration by firstly increasing at low concentrations then decreasing at high concentrations. This is the first time that such a process has been observed in a silica host- to the best of the author's knowledge. The increase in the lifetime was attributed to self-absorption of the fluorescence. Self-absorption is dominant at low concentrations owing to the strong

absorption in ytterbium. As the dopant concentration increased, cooperative energy transfer from ytterbium and erbium ions and other quenching mechanisms reduce the lifetime. This quadratic behavior makes the 1032 nm fluorescence lifetime unsuitable for determining concentration as a single lifetime could correspond to two different dopant levels.

Finally, the 635 nm fluorescence lifetime in praseodymium-doped fluoride glass was investigated. Fluorescence from two thermally coupled excited states, the  $^3P_0$ ,  $^3P_1$  states, was studied which found that the 635 nm fluorescence lifetime decreased with concentration over the entire concentration range studied. While the fluorescence lifetime decreased with concentration, there was also a strong dependence on temperature. It was found that at low concentrations, the fluorescence lifetime increased with temperature while at high concentrations, the fluorescence lifetime decreased with temperature. A model was developed to accurately describe the influence of both the concentration and temperature on the fluorescence lifetime. The model predicted that at  $1.30 \times 10^{26}$  ions/m<sup>3</sup> the fluorescence lifetime should be independent of temperature.

Of the samples studied in this work, only the 635 nm fluorescence lifetime in praseodymium showed suitability for determining concentration. The fluorescence lifetime in praseodymium had a monotonic change with concentration over the entire concentration range studied.

# Acknowledgments

In the course of my studies I have been very fortunate to have received assistance and support from many people to whom I would like to express my thanks.

I would firstly like to thank Dr. Gregory Baxter and Dr. Peter Farrell, my supervisors, for giving me the opportunity to undertake this project.

I would like thank past and present members of the Optical Technology Research Laboratory group for whom I have had the pleasure of knowing and working with. In particular, I would like to thank Steven Trpkovski, my partner in crime, and David Simpson for their friendship and helpful discussions.

Of the staff members of the Physics Section, I would like to thank Mr. Donald Ermel, Mr. Alex Shelamoff, Mr. Abdurrahman Kuzucu and Mr. Hayrettin Arisoy for their technical support. Thanks to Dr. Jakub Szajman for his assistance with L<sup>A</sup>T<sub>E</sub>X.

During the course of my PhD program, I was fortunate to be closely associated with the Victoria University Postgraduates Association (VUPA). I would like to thank the VUPA Council for their time and tireless commitment to a worthwhile cause. In particular I would like to thank Tony Doss, the VUPA Development Officer. His commitment and integrity is much admired.

I would like to thank the Laboratoire de Physique de la Matière Condensée (LPMC), University of Nice, France, for their hospitality and support during my stay in France. In particular I would like to thank Dr. Gerard Monnon, Director of the

LPMC, for his generous support and valuable discussions.

I would like to thank the School of Communications and Informatics, Victoria University, for the financial support through the provision of the School Research Scholarship. I would like to thank the Australian Research Council for their financial support in the project through the provision of the ARC Large Grant. I would also like to acknowledge the financial support of the French Government through the French Government Scientific Fellowship.

Finally, I would like to thank my family for their faith, encouragement and support during the course of this PhD program. To my dad, Gieng, my mom, Thom, my sister, Thao, and my brother, Thien. This thesis is dedicated to you guys.

# Contents

<b>1</b>	<b>Introduction</b>	<b>1</b>
1.1	Introduction . . . . .	1
1.2	Applications of Rare Earth-doped Fibres . . . . .	2
1.3	Significance of the dopant concentration . . . . .	5
1.4	Techniques for Determining Concentration . . . . .	7
1.5	Scope of Thesis . . . . .	15
<b>2</b>	<b>Spectroscopy of Rare Earths</b>	<b>20</b>
2.1	Relaxation Processes . . . . .	22
2.1.1	Radiative Relaxation . . . . .	23
2.1.2	Phonon Relaxation . . . . .	23
2.1.3	Energy Transfer and Cooperative Effects . . . . .	24
2.2	Erbium . . . . .	27
2.3	Praseodymium . . . . .	30
2.4	Ytterbium . . . . .	32
<b>3</b>	<b>Fabrication of Rare Earth-Doped Optical Fibres</b>	<b>34</b>
3.1	Fabrication of Rare Earth-doped Fibres . . . . .	36
3.1.1	Deposition . . . . .	36
3.1.2	Solution doping . . . . .	38
3.1.3	Fusing and collapsing . . . . .	39
3.1.4	Drawing . . . . .	40
3.2	Fibre Characteristics . . . . .	42
3.2.1	Rare earth concentrations . . . . .	43
<b>4</b>	<b>Erbium-doped Fibres</b>	<b>50</b>
4.1	1550 nm Fluorescence . . . . .	50
4.1.1	1550 nm Fluorescence Lifetime Modelling . . . . .	51
4.1.2	Limitations to the Model . . . . .	56
4.1.3	Experimental Arrangement . . . . .	59
4.1.4	Experimental Results . . . . .	61
4.2	550 nm Fluorescence . . . . .	69
4.2.1	Modelling . . . . .	71
4.2.2	Experimental arrangement . . . . .	72
4.2.3	Experimental results . . . . .	74
4.3	Conclusion . . . . .	75
<b>5</b>	<b>Yb:Er-codoped Fibre Preforms</b>	<b>76</b>
5.1	Modelling . . . . .	77
5.2	Experiment . . . . .	79

5.3	Results . . . . .	81
5.4	Mechanisms Affecting the Lifetime . . . . .	83
5.4.1	Spontaneous Emission . . . . .	84
5.4.2	Self-absorption . . . . .	84
5.4.3	Resonant Energy Migration . . . . .	86
5.4.4	Phonon Decay . . . . .	87
5.4.5	Concentration Quenching . . . . .	87
5.4.6	Cooperative Luminescence . . . . .	87
5.5	Limitations Of This Work . . . . .	88
5.6	Conclusion . . . . .	88
<b>6</b>	<b>Praseodymium-doped glass</b>	<b>90</b>
6.1	Modelling . . . . .	91
6.2	Experimental Arrangement . . . . .	92
6.3	Results . . . . .	93
6.4	Temperature Dependence . . . . .	95
6.5	Concentration-Dependent Processes . . . . .	97
6.6	Conclusion . . . . .	100
<b>7</b>	<b>Conclusion</b>	<b>101</b>
7.1	Summary of Findings . . . . .	101
7.1.1	Fluorescence lifetime in Er-doped fibres . . . . .	101
7.1.2	Fluorescence lifetime in Yb:Er-codoped fibre preforms . . . . .	102
7.1.3	Fluorescence lifetime in Pr-doped bulk glass . . . . .	103
7.2	Concentration Determination and Imaging . . . . .	103
	<b>Bibliography</b>	<b>106</b>
	<b>Appendices</b>	<b>119</b>
<b>A</b>	<b>Publications</b>	<b>119</b>
A.1	Regular Journal Publications . . . . .	119
A.2	International Conference Proceedings . . . . .	119
A.3	Australian Conference Proceedings . . . . .	120
A.4	Others . . . . .	120
<b>B</b>	<b>List of Abbreviations</b>	<b>121</b>

# List of Figures

2.1	Periodic table of the elements . . . . .	21
2.2	Examples of energy transfer . . . . .	26
2.3	Er <sup>3+</sup> energy level diagram . . . . .	28
2.4	Cross-relaxation in erbium . . . . .	30
2.5	Pr <sup>3+</sup> energy level diagram . . . . .	31
2.6	Yb <sup>3+</sup> energy level diagram . . . . .	33
3.1	Preform deposition . . . . .	38
3.2	Fibre drawing tower . . . . .	41
3.3	Refractive index profile of Er3 fibre preform . . . . .	43
3.4	Experimental arrangement for measuring fibre absorption . . . . .	44
3.5	Absorption spectrum of fibre Er3 . . . . .	45
3.6	Experimental arrangement for measuring preform absorption . . . . .	46
4.1	Er <sup>3+</sup> energy level diagram of the <sup>4</sup> I <sub>13</sub> state . . . . .	52
4.2	Fluorescence lifetime vs. dopant concentration and initial excited state population . . . . .	57
4.3	Schematic diagram of the experimental arrangement for measuring the 1550 nm fluorescence lifetime . . . . .	60
4.4	1550 nm fluorescence spectra of Er4 pumped at 20 to 50 mW. . . . .	62
4.5	Pump saturation level for Er1 . . . . .	63
4.6	Comparison of model fit to exponential fit . . . . .	64
4.7	The 1535 nm fluorescence lifetime vs. initial population and concentration . . . . .	65
4.8	Fluorescence lifetime of Er2 and Er6 . . . . .	65
4.9	Radiative decay rate vs. initial population and concentration . . . . .	67
4.10	Energy transfer coefficient vs. initial population and concentration . . . . .	68
4.11	Energy transfer coefficient vs. concentration . . . . .	69
4.12	Energy transfer transitions involving the <sup>4</sup> S <sub>3/2</sub> excited state . . . . .	71
4.13	Experimental arrangement for measuring the 540 nm fluorescence lifetime . . . . .	73
4.14	540 nm fluorescence lifetime vs. dopant concentration . . . . .	74
5.1	Energy transfer between Yb <sup>3+</sup> and Er <sup>3+</sup> . . . . .	77
5.2	Absorption and emission spectra of Yb <sup>3+</sup> . . . . .	79
5.3	Fluorescence decay of YbEr5 . . . . .	81
5.4	Fluorescence lifetime of Yb <sup>3+</sup> as a function of pump power . . . . .	82
5.5	Fluorescence lifetime of Yb <sup>3+</sup> as a function of dopant concentration . . . . .	83
5.6	Self-absorption and resonant energy migration with Yb <sup>3+</sup> . . . . .	85
5.7	Evidence of self-trapping . . . . .	86

6.1	Experimental arrangement for measuring $\text{Pr}^{3+}$ lifetime . . . . .	92
6.2	$\text{Pr}^{3+}$ fluorescence lifetime as a function of temperature . . . . .	93
6.3	Decay rates $\Gamma_{10}$ and $\Gamma_{20}$ vs. dopant concentration. . . . .	94
6.4	The fluorescence lifetime of $\text{Pr}^{3+}$ as a function of temperature. . . . .	95
6.5	The fluorescence lifetime of $\text{Pr}^{3+}$ as a function of concentration. . . . .	96
6.6	Sensitivity of the $\text{Pr}^{3+}$ lifetime with temperature . . . . .	97
6.7	Simplified energy level diagram and cross-relaxation processes in $\text{Pr}^{3+}$	98

# List of Tables

2.1	Phonon parameters . . . . .	24
2.2	Phonon decay rates for erbium . . . . .	29
3.1	Fibre and bulk sample characteristics . . . . .	48
3.2	Atomic weight of ZBLAN . . . . .	49
4.1	Comparison of the up-conversion coefficient . . . . .	70
6.1	Fitted values for modelling Pr <sup>3+</sup> fluorescence lifetimes. . . . .	96

# Chapter 1

## Introduction

### 1.1 Introduction

The field of fibre optics is now over forty years old, none-the-less it still attracts considerable and growing interest. This is demonstrated by the accelerated rate of development and commercialization of fibre optics-based technology [1]. The primary driving force behind this growth of interest has been the benefits that optical fibres provide in telecommunications. These benefits include larger bandwidth, lower attenuation and the ability to carry data at higher rates than other transmission media.

Nowhere has fibre optics been applied more than in long haul and transoceanic links connecting various continents around the world. One of the latest is the Southern Cross cable which opened in November 2000 linking Australasia and the United States. This cable transmits at 130 Gb/s, or an equivalent of 2 full length motion pictures every second. A single optical fibre is capable of carrying over a billion telephone calls simultaneously. Compare this with the first electrical submarine link in 1956 between the United Kingdom and the USA capable of transmitting only 48 telephone calls simultaneously [2].

In optical telecommunications, optical fibres do not just provide the medium by which data is transmitted. They also play an active role in the regeneration of optical signals as the signals undergo attenuation along the fibre link. This is achieved through the use of optical amplifiers and repeaters made from special optical fibres that have been doped with rare earth elements to alter the properties of the fibres.

The introduction of the erbium-doped optical fibre amplifier in 1987 brought about a revolution in optical telecommunications [3].

## 1.2 Applications of Rare Earth-doped Fibres

The rare earths are a group of elements classified in one of two groups. The first group of rare earths are known as the lanthanide series, with atomic numbers 57 to 71, and have similar chemical properties to the element lanthanum. The second group of rare earths are known as the actinide series having atomic numbers 89 to 103 and chemical properties similar to that of the element actinium. Actinides are relatively unstable elements making them unsuitable in most practical applications. The term rare earth has become synonymous with the lanthanides in many areas of science. In this thesis, the term rare earth will describe the lanthanide elements. Rare earth-doped optical fibres are optical fibres which incorporate these elements in the core region of the fibre so as to alter the fibre's response to the light as it propagates along the doped fibre.

Rare earths have interesting optical properties and many exhibit energy structures that are ideal for applications requiring stimulated emission and laser action. Their excited state lifetimes are long and their quantum efficiencies high. The possibility of obtaining new laser transition wavelengths for specific applications (such as biomedical, surgery, sensing and data storage) has driven the investigation of laser materials made with rare earths. Laser action has been demonstrated in optical fibres doped with neodymium [4], erbium [5], ytterbium [6], thulium [7], praseodymium [8], samarium [9] and holmium [10]. Laser action at multiple wavelengths within the same fibre species has also been demonstrated [11, 12].

Fibre lasers offer the advantage of higher efficiencies and superior heat dissipation due to their large surface area compared to conventional bulk solid-state lasers. Conversion efficiencies of over 80% can be achieved in fibre lasers [13]. They are compact, stable and easy to build and operate. Ytterbium has shown to be a very successful

rare earth element for fibre lasers because of its relatively simple energy structure, high quantum efficiency and high absorption coefficient. Diffraction-limited ytterbium fibre lasers are now commercially available with output powers in excess of 100 W continuous-wave. US-based IPG Photonics Corp recently announced the launch of a record breaking 2 kW continuous-wave diode-pumped ytterbium-doped fibre laser to the market [14]. The availability of high power ytterbium-doped fibre lasers have made possible the economical development of Raman fibre amplifiers leading to the deployment of long-haul and ultralong-haul networks as well as optical amplification of the S-band (1460-1530 nm) for dense wavelength division multiplexing [15]. In addition to their use as lasers, superfluorescent or superluminescent sources have been developed using rare earth-doped fibres allowing for broadband light sources with tunability over 40 nm for pumping and sensing applications [16, 17].

The high quantum efficiencies and strong absorption of rare earths have also allowed rare earth-doped fibres to be used as optical fibre amplifiers. The most important and most developed of these is the erbium-doped fibre amplifier because of its transition at around 1550 nm corresponding to the third transmission window in the silica-based optical fibre communications system. Erbium-doped fibre amplifiers are used for amplification of wavelengths in the range 1530 - 1565 nm known as the C-band in optical communications. Thulium-doped fibre amplifiers are now being developed for amplification of wavelengths in the S-band at 1460 - 1530 nm where erbium-doped fibre amplifiers are less efficient [18]. Optical amplification has also been demonstrated with praseodymium-doped fibre at helium-neon laser wavelengths at 623.8 nm [19] and at 1300 nm for use in optical telecommunications [20]. High-powered ytterbium-doped fibre amplifiers operating around 1080 nm [21] and neodymium-doped fibres operating around 1060 nm [22] have also been studied.

Fibre optic technology using rare earth-doped optical fibres has also been developing in other areas, most noticeably in sensing. Their immunity to electromagnetic interference makes them the preferred choice over conventional electrical sensors for use in electromagnetically harsh environments. Their small size is advantageous in

places requiring small footprints or size restrictions such as in medical and biological applications. In many cases, the fibres are the sensing media and not just being passive signal carriers. As such, any section of the fibre can be used as a sensor making them candidates for high resolution distributed sensing applications [23]. Their long transmission capabilities allow for remote sensing at distances that may be many kilometers. Rare earth-doped fibre sensors may be used to measure such stimulus as temperature based on the change in their absorption [24], fluorescence intensity [25] or fluorescence lifetime [26].

The very strong, sharp absorption bands in rare earth-doped fibers can be applied as wavelength filters in which the absorption lines match the wavelengths to be filtered out [27]. Very high rejection optical filters can be constructed in this way.

Another novel application is optical cooling of a rare earth-doped fibre by a laser. Laser induced cooling is the process in which a rare earth-doped fibre is cooled when pumped with a laser whose wavelength is longer than the wavelength at which the fibre fluoresces. This effect is commonly termed anti-Stokes fluorescence and results in more energy being emitted by the fibre than the energy being absorbed through optical pumping, thus effectively cooling the fibre. Successful anti-Stokes fluorescence requires two energy levels to be sufficiently far apart such that decay from the higher energy level to the lower level is radiative and not through other non-radiative process which are heat-generating. That is, high quantum efficiency is desired [28]. Rare earths exhibit high quantum efficiencies and in particular, ytterbium has been a prime candidate for optical cooling of solids because of its higher quantum efficiency and relatively simple energy structure. Cooling by as much as 65 K, from room temperature, has been achieved using a ytterbium-doped fibre [29]. Rare earth-doped bulk samples have shown higher cooling efficiencies. Successful demonstrations of optical cooling of solids have made possible the realization of miniature optical refrigerators and cryocoolers for applications in cooling and temperature stabilizing of integrated circuits and microelectronics providing vibration-free and maintenance-free operation [30].

### 1.3 Significance of the dopant concentration

Fundamental to these applications are the type of rare earth elements, the number of rare earth ions, or dopant concentration, and dopant distribution within the active region of the fibre. The concentration profile of rare earth elements in optical fibres and waveguides is an important parameter in modelling and characterizing laser and amplifier performance. Calculations of the signal and pump power along the fibre length requires knowledge of the dopant distribution across the fibre core thus affecting such parameters as gain, saturation and efficiency [31]. The dopant distribution can not be easily controlled during the fibre fabrication process and distribution information is not usually provided by the fibre manufacturer. It is usual to assume that the dopant radial distribution follows a step profile [32] or a Gaussian profile [33].

Martín has shown that the gain of an erbium-doped fibre can differ significantly depending on erbium transversal distribution characteristics [34]. Martín showed that the gain for transverse distribution profiles that follow a step index varied in comparison to a Gaussian profile. It is common in the fabrication process of making rare earth-doped optical fibres to introduce a depression, or dip, at the centre of the fibre in the dopant distribution. Martín has shown that this depression also affects the amplifier gain. Furthermore, the gain is dependent on the overlapping factor between the signal mode-field area and the transverse dopant area [35]. Thus the radial dopant distribution, or dopant area, also affects the gain. In addition, the signal mode-field area is wavelength-dependent, hence it is not possible to achieve optimum gain using a single distribution profile for all common wavelengths. Variations in the amplifier gain due to the transverse mode field profile and dopant distribution have been reported as far back as 1992 [36] and tight confinement of the dopant within the core centre has shown to provide the best gain efficiency [37].

The gain and efficiency of erbium-doped fibre amplifiers and lasers are also strongly

dependent on the dopant level. For amplifier applications, the erbium concentration is only a few hundred parts per million (ppm). Erbium-doped fibre amplifiers operating in the L-band (1565 - 1610 nm) require significantly longer lengths of doped fibre than amplifiers operating in the C-band because of the lower gain in the L-band. L-band amplifiers use as much as 100 m of doped fibre costing several hundred to several thousand dollars. The erbium-doped fibre is a major cost component and can represent up to 30 % of the overall cost of the amplifier [38]. Increasing the dopant concentration can increase the efficiency of the device because more of the pump power is being absorbed. The result is better amplification for a given input power. Alternatively, less pump power, or shorter fibre lengths are required because of the higher gain per unit length resulting in lower material costs. The same is true for lasers and other applications. However, as the dopant concentration increases, the separation between adjacent ions decrease and ion-ion interactions begin to occur.

Ion-ion interactions are processes in which energy transfer occurs between neighboring ions. Energy transfer in rare earth-doped materials have been known for quite some time with studies of rare earth ions in solids dating back to the 1940s. Energy transfer is discussed in more detail in chapter 2. Because of the non-radiative nature of many energy transfer processes, this effect is often seen as parasitic as it competes with radiative transitions that take place from the same energy level during the lasing or amplification process. It is therefore not practical to increase the dopant concentration arbitrarily to increase gain and efficiency for this reason. Erbium-doped pure silica fibres without the addition of network modifiers (additional components incorporated to modify the structure of the glass) have shown deterioration of the gain characteristics for concentrations below 1000 ppm with optimum erbium concentrations being less than 100 ppm [39].

The ability to accurately determine the dopant concentration and distribution of the active dopants in optical fibres is fundamental to accurately predicting the performance and behavior, as well as improving performance and reducing cost, of

devices incorporating these rare earths. Thus a reliable method for determining these parameters is sought.

## 1.4 Techniques for Determining Concentration

Previous techniques for determining the dopant concentration and distribution have been borrowed from analytical chemistry and material science. These techniques include secondary ion mass spectroscopy [40, 41], inductively coupled plasma mass spectroscopy, inductively coupled plasma atomic emission spectroscopy [39, 41], x-ray microprobe analysis [42], electron probe microanalysis [43, 44], fluorescence-induced laser scanning microscopy [45], and neutron activation analysis [46]. These techniques can be placed into one of two groups. The first is mass spectroscopy in which the dopants are identified by measuring the relative mass and charge of the dopants present in the sample material. The second group of techniques is excitation in which the sample material to be analyzed is excited with an energy source. This excitation results in emissions of characteristic radiation that is used to identify the dopants in the sample.

Secondary ion mass spectroscopy (SIMS) involves the bombardment of high energy ions (primary ions) onto the surface of a solid sample placed in a vacuum chamber. The bombardment causes ions from the surface of the sample (secondary ions) to eject or sputter. These ejected ions are collected using a mass spectrometer and their mass to charge ratios are analyzed to allow identification of the ions in the sample. The amount of sputtered ions that is detected, or ion count, gives a measure of the concentration of that ion in the sample. SIMS is capable of identifying any ion, element or molecule. SIMS was first developed and built by the National Aeronautics and Space Administration (NASA) in the early 1960s to analyze moon rocks. This method uses a focused ion beam to bombard the sample surface. Using this technique it is possible to map the lateral distribution of the elements on the sample surface by raster scanning the primary ion beam across the sample surface. The ion intensity at each point in the raster scan is a function of the relative concentration of

the element at that point. The resolution of such an image depends on the primary ion beam diameter. Resolutions of the order of  $0.5 \mu\text{m}$  are possible. One of the drawbacks of this method is that it is destructive, the bombardment of the sample causes erosion and edging as it ablates the sample surface. Another drawback is the complicated and sophisticated arrangement of the instrument. The SIMS instrument requires an ultrahigh vacuum environment often produced by multiple high quality pumps. The quality of the vacuum environment is critical to the accuracy of the results adding to the complexity and cost of the instrument. The instrument is bulky and not suited for benchtop use. The SIMS technique uses bulk samples of size typically  $1 \times 1 \text{ cm}$  and only a few millimeters thick. Careful calibration of the detected ion intensity to the ion concentration is required for accurate determination of concentration.

Inductively coupled plasma mass spectroscopy (ICP-MS) and inductively coupled plasma atomic emission spectroscopy (ICP-AES) are techniques that require the sample under examination to be atomized using a plasma torch [47]. The high temperature of the plasma, ranging from  $5000 - 8000 \text{ }^\circ\text{C}$ , ensures that all molecules and particles are broken down to its constituent atoms or ions, although some molecules such as  $\text{N}_2$ ,  $\text{C}_2$  and  $\text{OH}$  can survive [48]. ICP requires the sample under examination to be vapourised into fine particles or aerosols before being introduced into the plasma. There are several methods to do this, one of which uses a high power laser to ablate the sample. In ICP-MS, the ions are collected and identified using a mass spectrometer in a manner similar to SIMS. In ICP-AES, radiative emissions from the plasma, usually argon which emits over a continuum of background radiation from the ultraviolet to the near-infrared, is used to excite the sample ions. Characteristic emissions from the ions resulting from this excitation are detected using a monochromator to identify the ions. The ICP techniques require a sample of the preform to be dissolved in a corrosive solvent into liquid form before being transported into the plasma zone for analysis. This is a destructive method of determining concentration. An additional disadvantage of such dissolution is the conversion of concentration units from the solution data to a solid basis i.e.; from units of grams

per milliliter (g/ml) to parts per million (ppm). This conversion lowers the sensitivity of detection by an order of magnitude or more [49]. These techniques are capable of detecting low absolute concentrations in the order of parts per billion, but is not capable of measuring the concentration distribution because of the dissolving nature of the technique. Like the SIMS spectrometers, ICP spectrometers are bulky and complicated instruments requiring high maintenance and trained operators.

Neutron activation analysis (NAA) involves the sample under analysis to be bombarded with neutrons. The bombarding neutrons are absorbed into the nucleus of the elements in the sample to produce a new nucleus with the same charge but an increased mass. This new nucleus is in an excited state due to the collision and quickly de-excites, or decays, to a more stable isotope by the emission of gamma rays that are characteristic of the element. These gamma rays are called prompt gamma rays and can be observed during irradiation. In most cases, the new isotope is radioactive and will de-excite by the emission of further characteristic gamma rays. These rays are called delayed gamma rays and can be observed after irradiation with neutrons. It is more common to measure the delayed gamma rays because of the slower rate of the radioactive half-life and the NAA technique generally refers to this type of measurement. NAA is one of the most sensitive of current techniques and can provide qualitative and quantitative analysis of elements down to parts per billion. Only about 70% of elements are suitable for analysis using NAA, however, it is capable of identifying rare earth elements. Neutron activation was first discovered by Hevesy and Levi in 1936 after observing certain samples containing rare earths became radioactive after being exposed to neutrons. The major drawback of this technique is the need for neutron sources typically requiring a nuclear reactor or cyclotron. In addition, the detection of gamma rays is usually performed using semiconductor detectors which operate at liquid nitrogen temperatures (77 K).

X-ray microprobe spectroscopy (XMS) involves using a finely focused x-ray microbeam to illuminate a sample under examination [50]. X-ray beams can be used to analyze data in one of two ways; diffraction or fluorescence analysis. Diffraction

analysis, or microdiffraction, uses the detection of scattered x-rays to give information about the structure and crystallography of the sample. X-ray diffraction is similar to other diffraction techniques such as electron or neutron diffraction with a few notable advantages; one of which being x-ray wavelength is similar to the atomic spacing of matter [50]. This method should allow for detection of clusters within rare earth-doped samples by measurement of x-ray absorption fine structures (XAFS) that provide localized structural information of the element of interest [51]. Fluorescence analysis, or microfluorescence, relies on using an x-ray to excite the sample causing emission of characteristic x-ray fluorescence that are used to identify elements within the sample in a manner similar to ICP-AES. XMS is inherently non-destructive. However, its use requires an x-ray source which normally require radioactive material. High intensity x-rays are only possible from synchrotrons which are large, public facilities normally shared amongst many users requiring advance booking. Access to such facilities is often a hinderance. XMS instruments require special x-ray focussing optics adding to the complexity and cost, which until recently have lacked quality and efficiency.

A similar technique to x-ray microfluorescence analysis is electron probe microanalysis (EPMA). EPMA works by illuminating, or probing, the sample with a finely focused electron beam. Characteristic x-rays are emitted from the sample as a result of excitation from the electron beam and elements can be identified from the emitted x-ray spectra. This technique is non-destructive. It is a more compact and simpler instrument compared to XMS and electron guns for illumination are readily available. Concentration distributions can be determined by scanning the electron probe over the surface of the sample. However resolution is limited by the electron beam limiting image resolution to about  $5 \mu\text{m}$ , which is insufficient for rare earth distribution in fibres as core diameters in fibres is typically  $9 \mu\text{m}$  for single mode fibre.

Fluorescence-induced laser scanning microscopy (LSM) is another excitation technique in which a laser beam, tuned to one of the absorption bands of the dopants,

is used to excite the sample under investigation. In LSM, the laser beam is focused onto the sample causing local excitation and emission of fluorescence with characteristic wavelengths which can then be detected. In most cases the intensity of the emitted fluorescence is proportional to the dopant concentration. The laser beam is scanned across the sample surface to provide information on the dopant distribution and profile. This technique is the simplest of the techniques thus far described and implementation is rather straight forward without requiring complicated or specialist equipment. The spacial resolution of this technique is limited to the excitation wavelength and the numerical aperture of the focusing optics. However, this method of imaging produces a large depth of field caused by interference from fluorescence of dopants that are out of focus and away from the focal region [52]. This reduces the contrast of the signal from the focal region and increases the resolution to orders of a few  $\mu\text{m}$ . This limits the technique to imaging bulk samples and preforms.

The techniques described above may be applied to bulk samples or fibre preforms but are not easily applied to drawn fibres. Resolution and practical limits prevent them from being used to determine the concentration profile in fibres. It is common to use preform concentration data and scale the data down to fibre dimensions after drawing. This assumes that the profile remains unchanged during the drawing process. Huntington *et al* has shown this to be invalid in their direct measurements of diffusion of dopant materials in a biconical fibre coupler [53]. Huntington *et al* found that the dopants have diffused from the core into the cladding during fibre drawing. Thus the appropriateness of this assumption may be questioned. Huntington's technique involved a cleaved fibre end being placed in hydrofluoric acid. The presence of dopants change the solubility of the fibre, hence changes the rate of etching by the acid. Thus the topographic structure caused by the etching is directly related to the dopant distribution. This technique is suitable for indicating dopant locations but provides little other information. It does not readily discriminate between different dopant species and thus could not distinguish between rare earths and other dopants such as germanium, although diffusion is more likely to occur with the smaller dopant species than the rare earths which are much larger.

Further, the etch rate for various dopants may vary with some dopants dissolving at a much greater rate than others. This technique also favours sites with structural defects which accelerate the rate of etching so producing inaccurate results.

A non-destructive method for measuring the concentration of rare earth-doped fluoride glasses was proposed by Fornoni *et al* [54]. This method has also been applied to erbium-doped optical fibres [55]. The method is based on the comparison of intensity of a fluorescence line emitted by the rare earth ion with the intensity of the Raman line from the host matrix. The ratio of the fluorescence signal to the Raman signal is proportional to the dopant concentration. A calibration curve is required from samples of known concentrations in order to deduce concentration information from an unknown sample from the measured intensity ratio. The intensity ratio varies not only with the host composition and dopant type but also with different fluorescence bands within the dopant emission spectra. Calibration curves are required for selected transitions in each dopant and each host. This calibration curve is found to be approximately linear at low concentrations but deviates from linearity above 2000 ppm and is no longer monotonic at very high concentrations greater than 7 % [56]. This makes the technique useful in many applications such as amplifiers where dopant concentrations are low and typically in the order of a few hundred ppm. Careful choice of the excitation wavelength is required to ensure that the Raman signal does not overlap with the fluorescence signal since the Raman signal wavelength is dependent on the excitation wavelength, while at the same time ensuring the excitation wavelength falls within the absorption band of the dopant. This technique is better suited to hosts such as crystalline, phosphate or fluoride glasses where Raman gains are high. The technique requires that the host exhibit Raman active vibration modes and detection is done using Raman detectors. The method requires strict control of the depth of focus of the probing laser beam for reliable results due to re-absorption of the fluorescent signal, while the Raman signal remains constant over a large range of depth of focus [56]. This technique is limited to providing absolute concentrations rather than concentration distributions.

In 1994, Uttamchandani *et al* applied a variation of the fluorescence-induced laser scanning technique using a confocal microscope to map the relative concentration profile of erbium-doped fibres by measuring the fluorescence intensity of the 565 nm fluorescence when pumped at 488 nm [57]. In 1995, Othonos *et al* extended this technique by using a phase-sensitive detection method to improve sensitivity and obtain a better signal-to-noise ratio [58]. The use of confocal microscopy reduces the depth of field allowing for sub-micron resolution, a great improvement over the conventional wide-field LSM. In both experiments the intensity profile was obtained by scanning across the centre of the fibre core. The profile obtained by this one-dimensional scan assumes a radial symmetry of the dopant distribution. In these two papers, it was assumed that the fluorescence intensity is proportional to the local dopant distribution. However, this assumption may be invalid for high doping concentrations where concentration dependent cooperative processes can alter the relaxation process, hence causing a decrease in the fluorescence intensity [59]. These techniques may thus be limited to the low concentration regime. In addition, concentration measurements made by the authors were based on reference concentration levels provided by the manufacturer, thus their techniques are not self-referencing. Fluorescence intensity detection is sensitive to alignment and the responsivity of the imaging system and is therefore prone to systematic errors such as heating effects, mechanical vibrations and beam drift.

A group of researchers at the Optical Technology Research Laboratory, Victoria University, developed a technique based on measurements of relaxation rates of the  $^3P_0$  excited state in praseodymium-doped fibres [60]. This represented the first time that lifetime measurements have been used to determine concentration profiles in optical fibres [61]. In this technique, Petreski *et al* measured the extent that cross-relaxation processes altered the relaxation rate of the  $^3P_0$  level. The images were resolved using a confocal microscope at 635 nm with the praseodymium-doped fibres being pumped at 476.5 nm. Unlike Uttamchandani *et al* and Othonos *et al*, who only scanned across the centre of the fibre end-face, Petreski *et al* imaged the entire fibre end-face to give a two dimensional image of the dopant concentration in the

fibre cross-section. Compared to the techniques demonstrated by Uttamchandani *et al* and Othonos *et al*, Petreski's technique was not dependent on the fluorescence intensity, hence did not rely on reference intensity levels from fibres of known concentrations. This technique is thus self-referencing. Since the concentration analysis based on lifetime measurements are not dependent on the intensity of the detected fluorescence, the technique is less sensitive to the optical properties of the imaging system.

There have been extensive studies on cooperative energy transfers in erbium [39, 62, 63] and erbium-codoped [64, 65, 66] fibres. But these effects have not been applied as a means of determining their concentration distribution in the fibres. However, energy transfer has been applied to produce scanning near-field optical microscopy (SNOM) images of dyed molecules in biological samples using Fluorescence Resonant Energy Transfer [67]. This method involves doping the tip of the SNOM probe with a donor dye which is then optically excited. The SNOM tip is made to contact with the sample which contains the acceptor dye and scanned across the sample surface. Energy is transferred from the donor to the acceptor if the donor comes to close proximity of the acceptor (typical distances required for resonant energy transfer are in the range 2 - 6 nm) [68]. This technique offers very high resolution imaging of regions of only a few tens of nanometers. This technique could also be applied to image rare earths in optical fibres by appropriate selection of donors to match resonant energy transfer to the acceptor samples.

Fluorescence lifetime has been used successfully and extensively in biology and biochemistry to study biological samples [69, 70, 71, 72]. The fluorescence lifetime spectroscopy of a photo-excited process can provide more information about that process than intensity spectroscopy alone. The fluorescence lifetime of organic molecules are dependent on the microenvironment in which the molecules and samples are placed and provides information about the rates of biochemical reactions and the kinetics of atomic and molecular processes [73]. Fluorescence lifetime spectroscopy is used in multilabelling of biological samples with dyes. Often the dyes have the same

emission wavelength when probed by a laser, but their emission lifetimes are usually different for different molecules within the labelled sample [69]. Fluorescence lifetime may be used to discriminate between different biological samples that have indistinguishable fluorescence spectra, such as collagen and elastin when excited with the same excitation source [74]. Fluorescence lifetime imaging also allows for the measurement of dye concentrations. High spatial resolution images have been obtained in the wide-field using a technique of structured illumination [75] (by selection of appropriate spacial modulation frequency), by confocal microscopy [76] (by selection of appropriately short excitation wavelength and pinhole size) or by near-field microscopy [77].

## 1.5 Scope of Thesis

Previous techniques have used spectrally-resolved spectroscopy to identify the dopant types and intensity measurements to determine the concentration levels. Spectral techniques remain the best way to identify the different dopant species. In developing a system for determining the absolute dopant concentration and imaging the dopant distribution of rare earth-doped optical fibres, it is desirable that the system be simple to use, compact and accurate. It is also desirable that the technique be non-destructive and be capable of measuring dopant distributions across the core of an optical fibre as well as its bulk preform. Such a system would be used by end users of doped fibres such as research organizations or product developers for characterizing and modelling of their rare earth-doped fibre-based products. Optical fibre manufacturers will also benefit.

In addressing the criteria for such a system, it is clear that bulk sample methods such as secondary ion mass spectroscopy and inductively-coupled spectroscopy cannot be used owing to the destructive nature of such techniques. While x-ray microprobe spectroscopy has the resolution to image optical fibres, it is not practical owing to the difficulties in handling small sample sizes and the complexity and cost of using x-rays. Electron probe and laser-induced scanning microscopy offer a non-

destructive and simple method for imaging dopant concentrations, but are limited to preforms because of resolution limits.

Of the techniques previously described, the laser-induced fluorescence intensity and lifetime confocal microscopy, as that used by Uttamchandani *et al* [57], Othonos *et al* [58] and Petreski *et al* [59], best match the desired criteria for an imaging system. They offer nondestructive and high resolution methods of imaging concentration that is suitable for direct imaging of optical fibres. Scanning confocal microscopes are now commercially available for intensity imaging as well as lifetime imaging with up to 40 ps temporal resolution [78]. Fluorescence lifetime imaging systems using time-gated images have shown time resolutions of less 10 ps [74].

Of the two techniques described above for quantifying dopant concentration, the fluorescence intensity imaging technique is much faster compared to the fluorescence lifetime technique. However, the intensity method requires knowledge of the absolute intensities of the absorbed and emitted light and is sensitive to the response of the optics in the imaging system requiring constant calibration. The optical characteristics of all the optical components in the system needs to be known and any optical losses in the system need to be adjusted for. In addition, fluctuations in the fluorescence intensity, due to the excitation source, scattering or absorption by contaminants or heating effects will also affect the outcome of the quantification. On the other hand, the lifetime method is insensitive to the intensity of the fluorescence and fluctuations in the fluorescence intensity do not greatly affect the accuracy of the measurement. This negates the need for constant calibration and referencing.

The advantage of the non-intensity-dependence and successful implementation of the principle in biology and biochemistry provides the motivation for developing an imaging system based on the fluorescence lifetime of rare earth dopants in optical fibres. In this work, the properties of the fluorescence lifetime of rare earth-doped optical fibres and waveguides are studied to assess the possibility of developing such an imaging system. The research will look at how the dopant concentration af-

ffects the fluorescence lifetime of various rare earths. Optical material doped with erbium, praseodymium as well as erbium codoped with ytterbium will be studied. Erbium is studied for its significance and wide spread use in optical communications. Praseodymium has also been chosen because of interest in praseodymium for sensing and amplification applications by this research group. The same approach could, however, be applied to other rare earth-doped fibres or waveguides because of the similarities in their optical characteristics and properties.

This research is not concerned with different methods of lifetime imaging such as confocal and near-field microscopy or time-gated imaging. The technical aspects of these techniques and their limitations can be found elsewhere in literature [71, 75, 77, 79]. Rather, this research is concerned with the fluorescence lifetime properties of rare earth elements and whether these properties are useful for determining their concentrations in optical fibres using the imaging methods mentioned above. The approach taken is to search for unique concentration signatures in the measured fluorescence lifetime for the dopants that are studied. Analysis of rate equations that govern the time-dependent evolution of the fluorescence decay should reveal the physical mechanisms behind these concentration-dependent signatures. It is from these rate equations that concentration information can be extracted. While each dopant may emit radiation at many different levels, only certain emissions are investigated here. It would not be possible to investigate all of the observed emissions as this would be far too time consuming. Instead, only a select number of emissions are studied for practical reasons.

This thesis consists of seven chapters. The research begins with a review of the spectroscopic properties of rare earths in chapter 2. Here the general properties of rare earths are discussed, particularly in solid hosts such as glass. Relaxation processes are described for both radiative and non-radiative relaxation. The properties specific to erbium, ytterbium and praseodymium are looked at in greater detail, in particular, with respect to their energy levels and radiative transitions. The review of the spectroscopic properties provide the background for developing rate equations

and models to help describe and understand the observed fluorescence lifetimes.

In chapter 3 the process of fabricating rare earth-doped preforms and fibres are discussed. The preforms and fibres used in this work were fabricated by the author using the techniques of modified chemical vapour deposition and solution doping. The limitations of these techniques are discussed with respect to control of doping levels and accuracy of dopant concentrations. The physical and optical characteristics of the samples are presented.

In chapter 4 the fluorescence lifetimes of the 1550 nm and 540 nm emission in erbium-doped silica fibre is studied. These two emissions are the dominant emissions found in a silica host. Theoretical modelling is derived using rate equations to describe the relationship between the erbium concentration and the lifetime of the fluorescence. Experimental data is obtained to support the proposed models.

In chapter 5 the lifetime of the 1032 nm fluorescence emission in ytterbium:erbium-codoped fibre preforms is studied to determine any relationship between the erbium and ytterbium concentration on the ytterbium lifetime. Ytterbium is a two-energy level system and does not typically exhibit energy transfer effects due to increased concentrations. However, when codoped with another dopant specimen, there is a concentration-dependent energy transfer between ytterbium and the second dopant. It is this property that is studied here in order to ascertain the use of this energy transfer to measure concentration.

In chapter 6 the fluorescence lifetime of the 635 nm emission in praseodymium-doped fluoride glass is studied. This emission has been used for temperature sensing because of the strong temperature dependence of the lifetime of this emission. Consequently, the temperature dependence is considered in the context of using the lifetime to measure concentration. A model is developed that describes the lifetime as a function of both concentration and temperature.

Chapter 7 concludes the thesis by summarizing the research outcomes from the previous three chapters. This chapter discusses the consequences of the findings with respect to the research aim and proposes future work leading from this research.

## Chapter 2

# Spectroscopy of Rare Earths

In modelling the fluorescence lifetime of rare earth-doped fibres, it is first necessary to understand some of their spectroscopic properties. This chapter reviews the spectroscopy of the rare earths of interest in this work. These include erbium, praseodymium and ytterbium. In particular, their energy structures and relaxation processes are reviewed.

The lanthanides class of rare earths are a group of elements as shown in figure 2.1. There are 15 elements in this group starting with lanthanum (La). The other fourteen elements, in order of increasing atomic weight, are cerium (Ce), praseodymium (Pr), neodymium (Nd), promethium (Pm), samarium (Sm), europium (Eu), gadolinium (Gd), terbium (Tb), dysprosium (Dy), holmium (Ho), erbium (Er), thulium (Tm), ytterbium (Yb), and lutetium (Lu). They are characterized by the electronic filling of the inner  $4f$  shell within the  $[Xe]4f^N5s^25p^66s^2$  electronic shells where the superscript  $N$  represents the number of electrons in the  $4f$  shell. Lanthanum has one electron while lutetium has fifteen electrons.

Rare earths have interesting optical characteristics because of their electronic configuration. Electronic transitions within the  $4f$  shell occur at optical frequencies and the number of electrons occupying the  $4f$  shell determines their optical characteristics. Rare earths are of particular interest in optoelectronic applications. They are most stable when in their triply ionised configuration. This occurs when one electron is removed from the  $4f$  shell and two electrons are removed from the  $6s$  shell. Their electronic configuration is thus  $4f^{N-1}5s^25p^66s^0$  and the ions are positively charged. The outer  $5s$  and  $5p$  shells remain filled. This has an effect of shielding

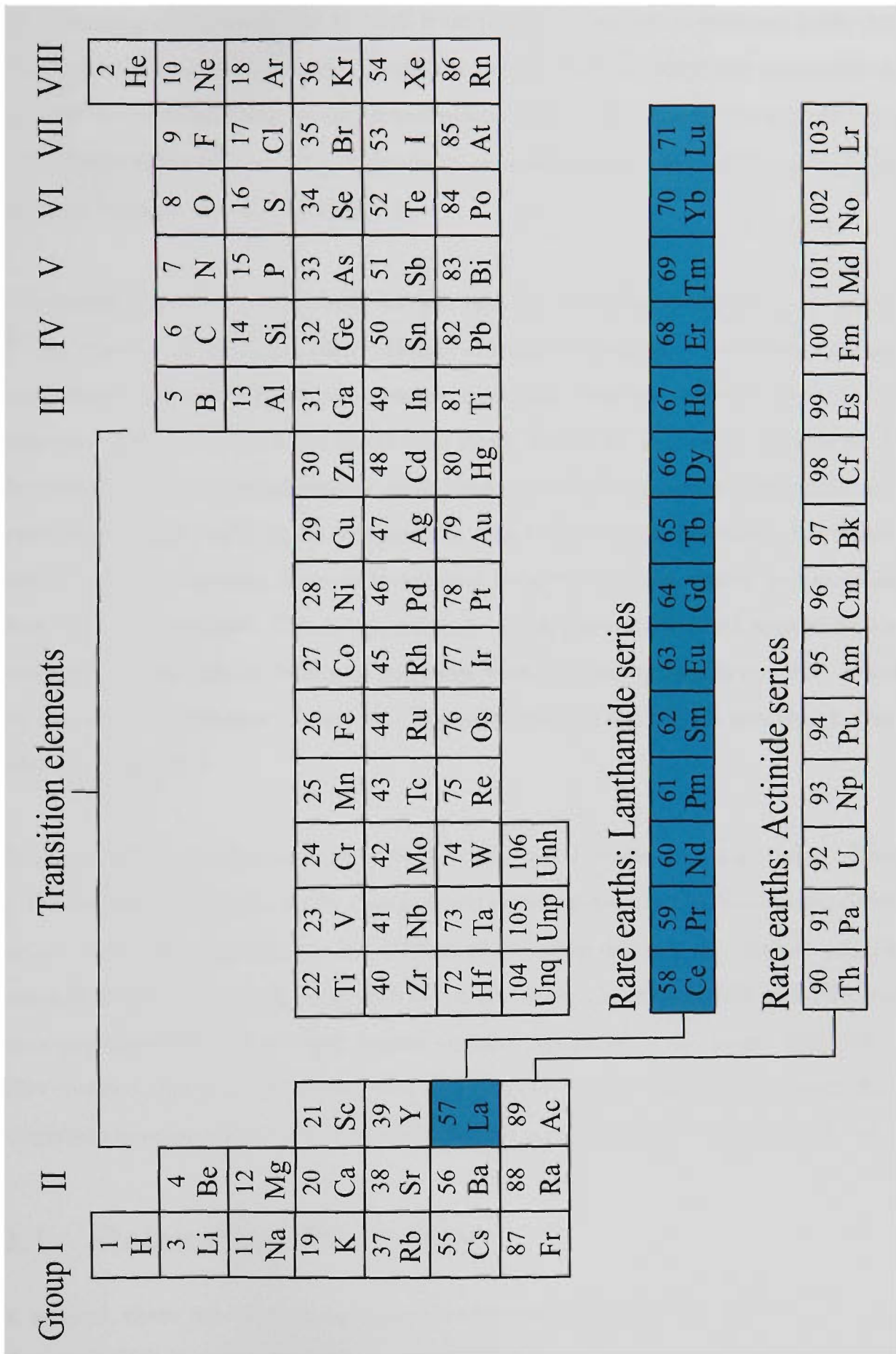


Figure 2.1: Periodic table of the elements.

the remaining electrons in the  $4f$  shell from perturbation due to external fields [80]. Consequently, electronic transitions within the  $4f$  shell are relatively insensitive to the host material and only weak perturbation occurs. The absorption and emission lines of rare earth ions are relatively sharp (in solid hosts) compared to most other elements because of this shielding [81].

The energy states of a rare earth ion are labelled with the spectroscopic notation  $^{2S+1}L_J$  where  $S$ ,  $L$  and  $J$  are the total spin angular momentum, total orbital angular momentum and total angular momentum quantum numbers respectively [82]. The quantum numbers define a set of electron states which are degenerate in energy. In the presence of an external electric field, these normally degenerate states split into a maximum of  $(J + 1/2)$  Stark components. Stark splitting occurs due to the crystal field of the host for most laser materials and broadens the absorption and emission lines of the energy level. The actual number of Stark levels observed depend on the symmetry of the crystal field and increases with decreasing symmetry [83]. Often not all the Stark levels are observed. The magnitude of such Stark splitting is typically  $10 - 100 \text{ cm}^{-1}$ .

The Stark levels are close enough to each other that they are thermally linked. That is, the relative population of the energy levels is determined by the Boltzmann distribution. The temperature-dependent thermal coupling changes the relative population within the Stark levels. As temperature increases, the upper Stark levels become more populated because of their higher energies compared to the lower Stark levels. This causes a change in the absorption and emission spectra. Rare earth-doped fibre temperature sensors have been developed using this temperature-dependence [84].

## 2.1 Relaxation Processes

In general, there are three main types of relaxation processes. They are radiative, phonon (which is non-radiative) and relaxation due to cooperative energy transfer (CET), which is also non-radiative. The total relaxation rate is the sum of these

three processes:

$$A^{Total} = A^{Radiative} + A^{Phonon} + A^{CET} \quad (2.1)$$

### 2.1.1 Radiative Relaxation

Radiative relaxation is characterized by the emission of a photon, and hence, produces fluorescence. When two energy levels,  $i$  and  $j$ , are sufficiently close they become thermally linked and their relative populations are determined by Boltzmann's distribution law:

$$\frac{N_i}{N_j} = \exp\left(-\frac{\Delta E_{ij}}{k_B T}\right) \quad (2.2)$$

$N_i$  and  $N_j$  are the populations of the upper and lower energy states respectively,  $\Delta E$  is the energy difference between the two levels,  $k_B$  is the Boltzmann constant and  $T$  is the absolute temperature. If  $\Delta E$  is sufficiently large, then the ratio of the population between the upper and lower states reduce to zero.

$$\frac{N_i}{N_j} = \exp\left(-\frac{\Delta E_{ij}}{k_B T}\right) \approx 0 \quad (2.3)$$

Where this occurs, the two energy levels are no longer thermally coupled and relaxation between the upper and lower levels can occur by the emission of photons. When in an excited state, the excited ion can lose its energy and revert to a lower state via two mechanisms. The excited ion can either spontaneously emit energy or be stimulated into emission by the presence of a photon of the appropriate energy. These mechanisms are known as spontaneous and stimulated emission respectively and result in the emission of a photon whose energy is equal to the difference in energy between the initial excited state and the final state.

### 2.1.2 Phonon Relaxation

Nonradiative phonon relaxation refers to the release of energy through the emission of phonons (e.g., vibration energy) into the host's crystal structure. Phonon decay is dependent on the energy spacing between the originating and terminating energy states and the vibration energy of the host's lattice structure. The phonon decay

rate from level  $i$  to level  $j$  is given by:

$$A_{ij}^{Phonon} = C[n(T) + 1]^p \exp(-\alpha\Delta E_{ij}) \quad (2.4)$$

where  $n(T)$  is the Bose-Einstein occupation and is given by:

$$n(T) = \frac{1}{\exp\left(\frac{\hbar\omega}{k_B T}\right) - 1} \quad (2.5)$$

where  $\hbar\omega$  is the maximum phonon energy for a given vibration mode and is host-dependent. The integer number of phonons,  $p$ , in equation 2.4, is given by the ratio of the energy gap  $\Delta E_{ij}$  to the phonon energy:

$$p = \frac{\Delta E_{ij}}{\hbar\omega} \quad (2.6)$$

The constants  $C$  and  $\alpha$  in equation 2.4 are host dependent constants and are insensitive to the rare earth energy levels.  $C$  increases with decreasing crystalline structure whilst  $\alpha$  decreases with decreasing crystalline structure as can be appreciated from table 2.1. Silica-based glass has greater phonon rates than fluoride-based glass. In addition, the phonon rate decreases with decreasing temperature due to the temperature dependence in  $n(T)$ .

Glass Host	$C$ (Hz)	$\alpha$ ( $10^{-3}$ cm)	$\hbar\omega$ ( $\text{cm}^{-1}$ )
Phosphate	$5.4 \times 10^{12}$	4.7	1200
Silica	$1.4 \times 10^{12}$	4.7	1100
Fluorozirconate	$1.59 \times 10^{10}$	5.19	500

**Table 2.1:** Comparison of host-dependent phonon parameters [85].

### 2.1.3 Energy Transfer and Cooperative Effects

Both radiative and phonon relaxation involve a single ion and are concentration independent. The third relaxation process involves two or more ions. At low con-

centrations, the average interionic distance between adjacent ions is sufficiently large that there is a low probability that an ion-ion interaction takes place. But as the concentration increases and the average separation between ions reduces, ion-ion coupling takes place resulting in cooperative energy transfer. In CET, an ion transfers some, or all, of its energy to a neighboring ion. The ion that gives up its energy is usually referred to as the donor and is demoted to a lower energy state. The ion that accepts the energy is referred to as the acceptor and is promoted to a higher energy state as a result of the energy transfer. CET takes place at very quick time intervals, in the order of nanoseconds (ns). There are two conditions that must be met for CET to take place. They are:

1. The energy gap between the originating and the terminating levels of the acceptor must equal the energy gap for that of the donor transition (within a phonon or two). Thus CET takes place only where there are resonant energy levels and there is overlap between the emission and absorption profile of the donor and acceptor respectively.
2. The physical separation between the donor and acceptor must be sufficiently close.

Examples of CET are shown in figure 2.2 for two-ion transfers. However, CET involving three or more ions are possible although the probability of multi-ion energy transfer decreases as the number of participating ions increase. CET may also involve different types of ions such as CET between ytterbium and erbium ions in a Yb:Er-codoped fibre.

The effects of CET may be considered as beneficial or detrimental depending on the application. In the case of sensitized luminescence, CET between a donor (also called the sensitizer) and an acceptor of another species (also called the activator) causes an observed emission by the activator which would otherwise not be observed under the same excitation conditions without the presence of the sensitizer. Sensitized luminescence may be used in codoped systems in which it is easier, or more efficient, to excite the sensitizer rather than direct pumping of the activator. Studies

of sensitized luminescence include such rare earth pairs as Yb:Er [86], Nd:Ho and Nd:Er [66] as well as multi-codopant systems such as Nd:Yb:Er [64]. CET in Yb:Er-codoped fibres is looked at in greater detail in chapter 5.

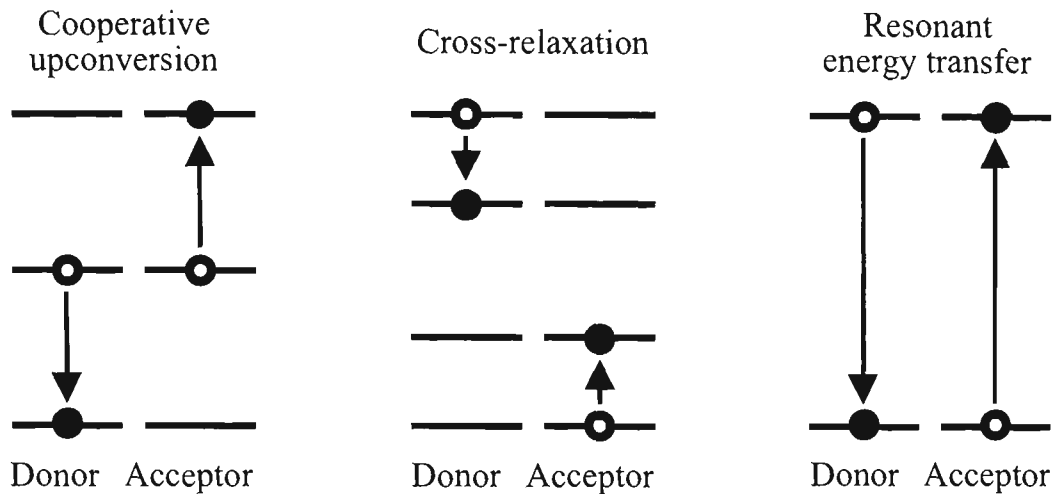


**Figure 2.2:** Examples of some cooperative energy transfer processes involving two ions. The white and black dots represent ions before and after CET respectively. Three ion process are also possible.

In many cases, CET processes compete with light amplification or lasing processes by reducing the population of the amplifier or laser level. This parasitic effect sets an upper limit on the rare earth concentration (often called concentration quenching), hence places a lower limit on the length of rare earth-doped fibres used in order to achieve the desired gain or performance.

In some cases, concentration quenching may also result in up-conversion fluorescence in which the wavelength of the observed fluorescence is shorter than the pump wavelength. Thus, emission in the UV may be observed with a visible or infrared pump source [87]. This particular case of energy transfer is known as cooperative frequency up-conversion (CFUC). CFUC often co-exists with excited state absorption (ESA). CFUC and ESA differs in that CFUC involves a non-radiative energy transfer between neighboring ions whereas ESA is the absorption of photons by individual ions in an excited state. ESA is concentration-independent while CFUC is concentration-dependent.

Energy transfer between two different ion types may result in fluorescence quenching. The term arises because the donor fluorescence is partially or completely suppressed by energy transfer to the acceptor. In this case, the acceptor does not emit fluorescence but decays non-radiatively. Fluorescence quenching may be used to suppress strong, unwanted fluorescence in order to promote weaker, more desirable transitions [66, 88, 89], and the acceptor is referred to as the deactivator.

In the case where energy levels are degenerate and the splitting of that energy level occurs, a broadening of the absorption and fluorescence spectra is observed. One Stark-split level may be more resonant to energy transfer or excited state absorption than another level, and energy transfer or excited state absorption may occur preferentially. Since the Stark levels are thermally coupled, their fluorescence properties also have a thermal dependence [90]. The thermal dependence on the gain in erbium-doped fibres have previously been studied [41].

## 2.2 Erbium

Erbium is the twelfth element in the lanthanide group with an atomic number of 68 and eleven electrons in the  $4f$  shell when in its triply ionised state ( $\text{Er}^{3+}$ ). With the advent of fibre optic communications, erbium has been of extensive interest because of its emission around 1550 nm corresponding to the third telecommunications transmission window. Erbium-doped fibres (EDFs) have brought about a revolution in communications systems with its use as amplifiers, repeaters and fibre lasers.

Figure 2.3 shows the energy level diagram for  $\text{Er}^{3+}$  indicating various absorption transitions. Erbium exhibits excited state absorption at many levels. Excited state absorption occurs when an ion that is already in an excited state absorbs a photon and is promoted to a higher energy level. In erbium there are many excited state absorption transitions that are resonant with ground state absorption transitions. These excited state transitions are normally seen as parasitic as they take away

pump or signal photons which may otherwise be used for pumping or causing stimulated emission.

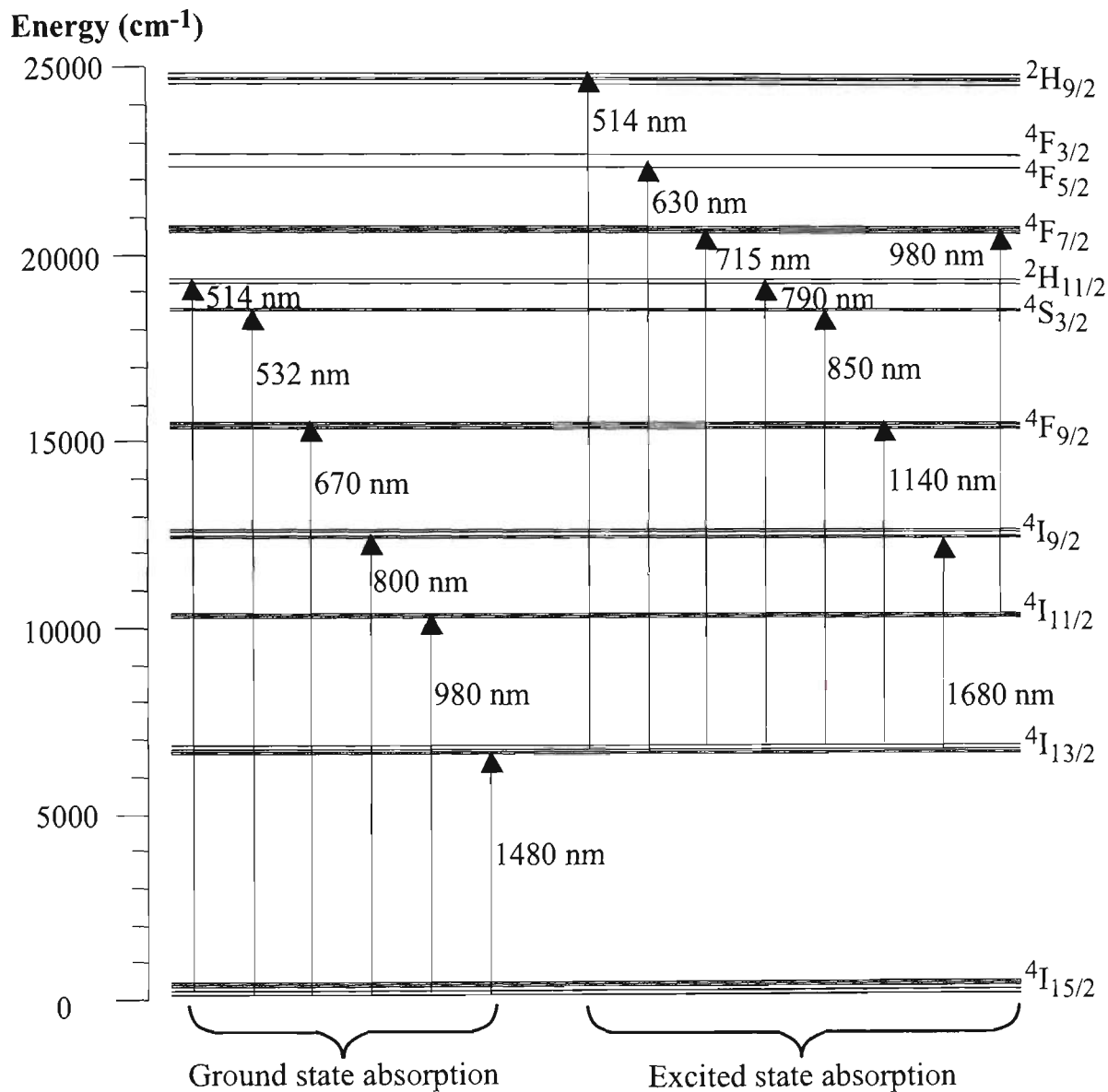


**Figure 2.3:** Simplified energy diagram of a triply ionised erbium ion showing possible ground state and excited state absorption transitions.

In silica hosts, decay from the excited states above the  $4I_{13/2}$  state is dominated by phonon relaxation due to the closeness of these levels and the high phonon relaxation rate in silica. Using the constants in table 2.1 for silica, the phonon decay rates can be calculated for erbium doped in silica glass. Table 2.2 shows the result of these calculations.

Transition	$A^{Phonon}(s^{-1})$	$\frac{1}{A^{Phonon}}(s)$
${}^4G_{11/2} \rightarrow {}^2H_{9/2}$	$2.67 \times 10^8$	$3.7 \times 10^{-9}$
${}^2H_{9/2} \rightarrow {}^4F_{3/2}, {}^4F_{5/2}$	$2.76 \times 10^7$	$3.67 \times 10^{-8}$
${}^4F_{3/2}, {}^4F_{5/2} \rightarrow {}^4F_{7/2}$	$1.76 \times 10^8$	$5.69 \times 10^{-9}$
${}^4F_{7/2} \rightarrow {}^2H_{11/2}$	$1.595 \times 10^{10}$	$6.27 \times 10^{-11}$
${}^2H_{11/2} \rightarrow {}^2S_{3/2}$	$6.37 \times 10^{10}$	$1.57 \times 10^{-11}$
${}^2S_{3/2} \rightarrow {}^4F_{9/2}$	$1.805 \times 10^4$	$5.54 \times 10^{-5}$
${}^4F_{9/2} \rightarrow {}^4I_{9/2}$	$1.57 \times 10^7$	$6.38 \times 10^{-8}$
${}^4I_{9/2} \rightarrow {}^4I_{11/2}$	$2.91 \times 10^7$	$3.44 \times 10^{-8}$
${}^4I_{11/2} \rightarrow {}^4I_{13/2}$	$4.64 \times 10^4$	$2.16 \times 10^{-5}$
${}^4I_{13/2} \rightarrow {}^4I_{15/2}$	0.0657	15.2

**Table 2.2:** Calculated phonon decay rates for  $Er^{3+}$  energy levels in silica.

The results show that apart from the  ${}^4I_{13/2} \rightarrow {}^4I_{15/2}$  transition, all other transitions have very fast non-radiative decay. The slowness of the  ${}^4I_{13/2} \rightarrow {}^4I_{15/2}$  decay arises due to the large energy gap ( $\approx 6500 \text{ cm}^{-1}$ ) between these two states. The radiative efficiency for the transition from level  $i$  to level  $j$  is defined as the ratio of the radiative decay rate to the sum of the radiative and non radiative decay rates and is given by (ignoring relaxation due to CET) [91]:

$$\eta_{ij} = \frac{A_{ij}^R}{A_{ij}^R + A_{ij}^{NR}} \quad (2.7)$$

With the radiative rate ( $A^R$ ) for the  ${}^4I_{13/2} \rightarrow {}^4I_{15/2}$  transition being approximately 100 Hz [83], the quantum efficiency for this transition is 99.9 % and the transition is essentially radiative. The predominant fluorescence that is observed in Er-doped silica glass is from  ${}^4I_{13/2}$  to ground corresponding to an emission wavelength around 1550 nm. The other emission normally observed is from  ${}^4S_{3/2}$  to ground corresponding to green fluorescence around 540 nm.

The complex energy structure of erbium permits many energy transfer transitions. Some examples of possible CET transitions in erbium are shown in figure 2.4 for two-ion and three-ion processes. There are many more possible combinations for CET. The probability of such combinations occurring will depend on the popula-

tions and the lifetimes of the participating levels.

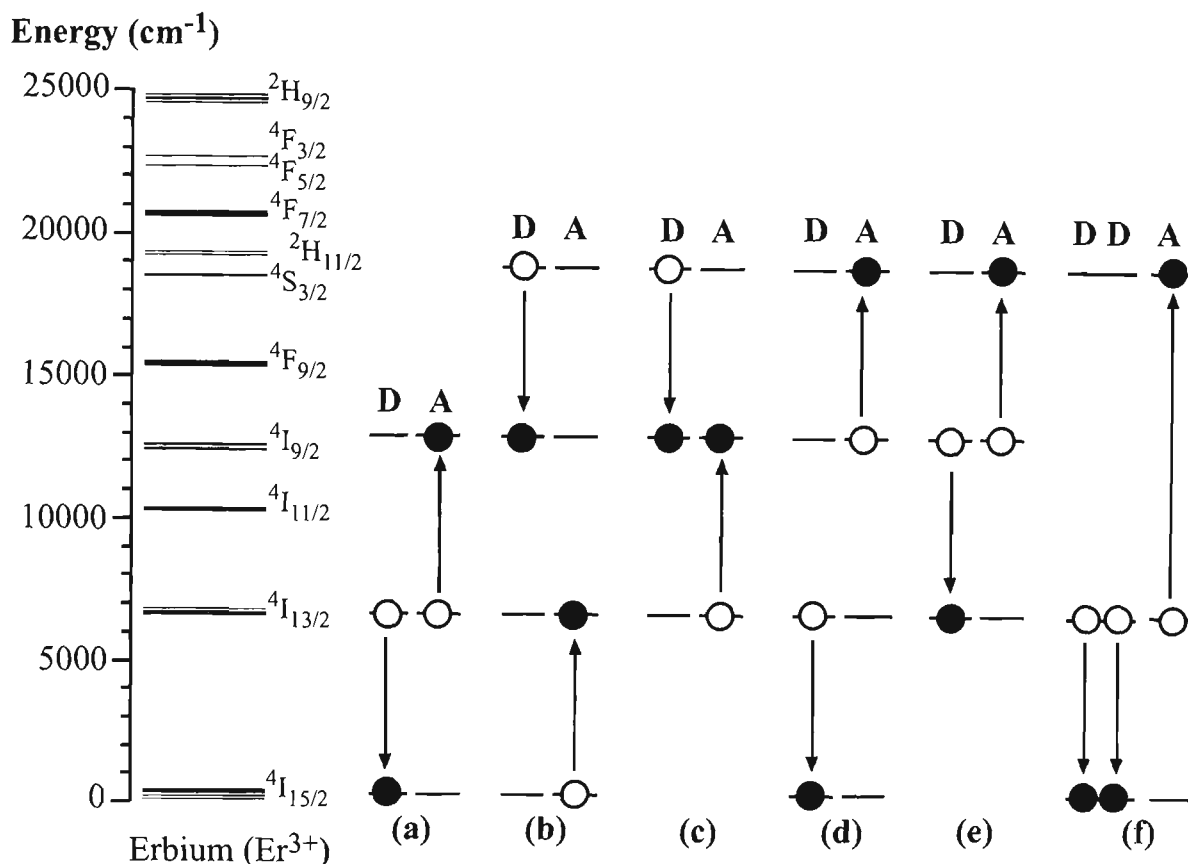


**Figure 2.4:** Simplified diagram of some possible cooperative energy transfer processes involving  $\text{Er}^{3+}$  ion pairs and triplets. The donor is labelled D and the acceptor is labelled A. Open dots represent ions before energy transfer while filled dots represent the same ions after energy transfer.

## 2.3 Praseodymium

Praseodymium is the third element in the lanthanide group of elements with an atomic number of 59 and two electrons in the  $4f$  shell when in its triply ionised state ( $\text{Pr}^{3+}$ ). Fluorescence emissions have been observed in the visible at 490, 520, 605, 633 and 695 nm [92] as well as in the infrared  $1.06 \mu\text{m}$  [93] and  $1.3 \mu\text{m}$  [94] in various host materials. Laser transitions have been observed at many of these wavelengths including multiple wavelengths within a single laser [95]. Many of these emissions originate from the  $^3P_0$ ,  $^3P_1$  and the  $^1I_6$  excited state. The  $^3P_1$  and  $^1I_6$  levels



## 2.4 Ytterbium

Ytterbium is the fourteenth element in the lanthanide group of rare earths with an atomic number of 70 and thirteen electrons in the  $4f$  shell when in its triply ionised state ( $\text{Yb}^{3+}$ ). Ytterbium has the simplest energy structure of all the rare earths consisting of only two energy levels in the optical spectrum, the  ${}^2F_{5/2}$  excited state and the  ${}^2F_{7/2}$  ground state. All other energy levels are in the ultraviolet region of the electromagnetic spectrum. However, the Stark splitting of the levels of interest are large, resulting in a broad absorption and emission band of about 200 nm with maximum room temperature absorption and emission at around 980 nm. This wavelength corresponds to transitions between the lowest Stark levels of each manifold [99]. The large splitting of the energy levels and the simple energy structure are ideal for optical cooling by anti-Stokes fluorescence because the pump and the peak emission wavelengths are sufficiently far from each other for increased cooling efficiency. The large emission linewidth also makes ytterbium suitable as broadband superfluorescent light sources [100]. Coupled with its strong absorption, ytterbium is an ideal specimen for sensitization and codoping with other dopants for improved pumping efficiency.

The thermal coupling between the Stark levels in each manifold are ideal for temperature sensing using the fluorescence intensity ratio (FIR) technique [101]. In this technique the intensity of fluorescence from two thermally coupled energy levels are compared to deduce the temperature. The large spacing between the Stark levels make the emission peaks easy to resolve.

The  ${}^2F_{5/2}$  excited state manifold and  ${}^2F_{7/2}$  ground state manifold are separated by about  $9000\text{ cm}^{-1}$  resulting in high quantum efficiencies. Ytterbium has a strong absorption coefficient at 980 nm of around  $2.5 \times 10^{-24}\text{ m}^2$  [paschotta97], up to an order of magnitude greater than other rare earths. The high quantum efficiency and strong absorption make ytterbium ideal as high power fibre lasers. In addition, because of ytterbium's two-level energy structure, there is an absence of any ESA

or CFUC. Also, its simple energy structure means ytterbium exhibits self absorption and resonant energy transfer, due to its strong absorption and the absence of any other decay process [102].

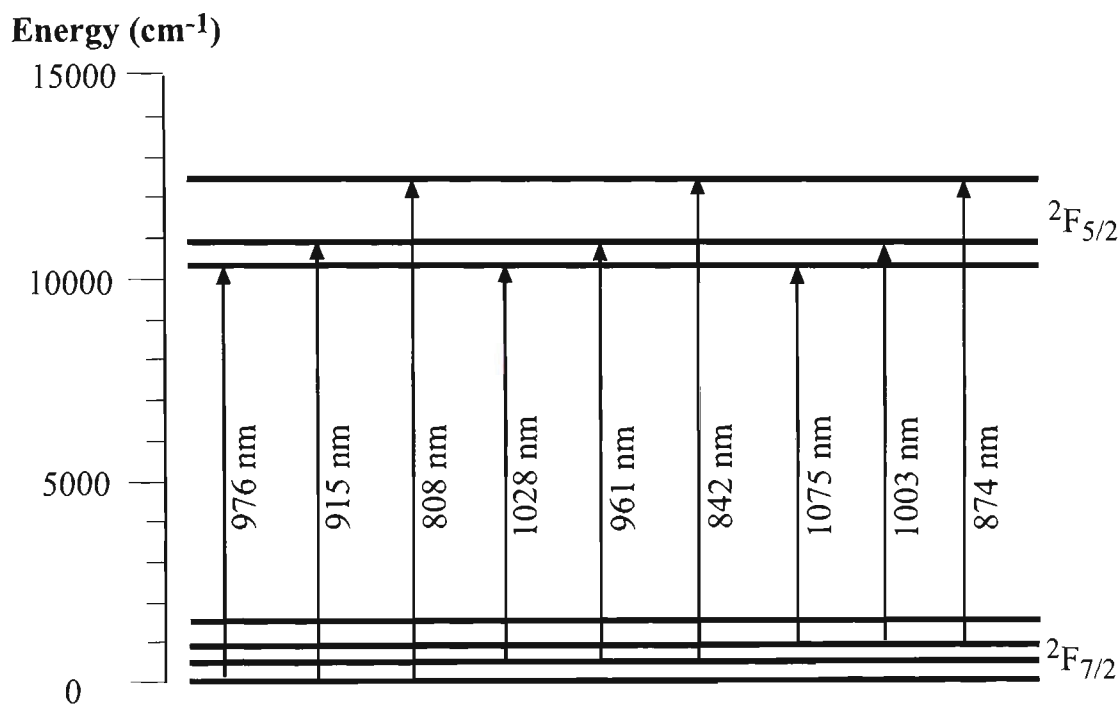


Figure 2.6: Simplified energy diagram of Yb<sup>3+</sup> in silica [103].

## Chapter 3

# Fabrication of Rare Earth-Doped Optical Fibres

In this work Er-doped silica fibres, Yb:Er-codoped silica fibre preforms and Pr-doped bulk fluoride glass were studied. Most of the fibres and preforms were fabricated by the author at the Laboratoire de Physique de la Matière Condensée (LPMC), Université de Nice (Nice, France). The Pr bulk samples were provided by the Telstra Research Laboratory (Melbourne, Australia). It is not known where these Pr samples came from prior to the Telstra Research Laboratory or how they were fabricated. The Pr samples are Pr<sup>3+</sup>-doped bulk fluoride glass. The fluoride composition consists of ZrF<sub>4</sub>(53%)-BaF<sub>2</sub>(20%)-LaF<sub>3</sub>(4%)-AlF<sub>3</sub>(3%)-NaF(20%), commonly referred to as ZBLAN [104]. Fluoride-based optical fibres were first developed as very low loss optical fibres for optical telecommunications in the infrared [49]. Rare earth-doped fluoride glass have some notable advantages compared to silica-based glass. Fluoride glass can be doped at higher concentrations compared to silica because the rare earths become a part of the glass network by replacing lanthanum in the glass matrix. In addition, fluoride glass have much lower phonon energies compared to silica glass (see section 2.1.2), thus allowing for additional radiative transitions to be observed in rare earth-doped fluoride glass compared to the same rare earths in silica-doped glass [105].

Optical fibres are waveguides that guide light through the process of total internal reflection within a thin strand of fibre, typically made of glass. The basic material requirements for making optical fibres are that the material be optically transparent and capable of being drawn into thin, uniform and durable fibres. Silica-based

glass has shown to be the most suitable material for optical fibres. It is relatively transparent at wavelengths between  $0.4\ \mu\text{m}$  to  $2\ \mu\text{m}$  with lowest losses at  $0.85\ \mu\text{m}$ ,  $1.3\ \mu\text{m}$  and  $1.55\ \mu\text{m}$ . These three wavelengths are commonly termed the three optical telecommunications windows.

Plastic fibres are also in widespread use for short-range applications. They are most transparent in the visible wavelength range, but attenuation is much greater than that of glass fibres. Plastic fibres are subject to temperature degradation limiting its use to operating temperatures typically below  $85^\circ\text{C}$ . However, they are cheap, light, flexible and easy to handle, making them an inexpensive alternative for transmitting visible light over short distances for illumination. Other variations of optical fibres include liquid-core fibres and hollow-core fibres.

Glass fibres, in particular silica, have been found to be the most suitable material for optical communications. Glass has various advantages compared to other solid state materials. These include high optical quality and high transparency at optical wavelengths. Glass is an amorphous material without a regular structure. It is defined as a frozen undercooled liquid. By this definition, glass has no fixed density or long range regular structure. One can then modify its properties and structure by certain treatments (e.g. by heat treatment or mechanical stress) or by incorporation of additional components to the glass. The first rare earth-doped fibre was made from a  $\text{Nd}^{3+}$ -doped barium crown glass core with a soda lime silicate glass cladding which led to the first observation of laser action in glass fibre [4].

Optical fibres are made by first realizing a fibre preform. The preforms are long glass rods that can be considered a macroscopic version of the fibres. The preforms are heated and softened in a furnace then pulled into a thin filament. The glass filament quickly cools in the air and solidifies into a fibre. The fibres are then coated with a coating such as silicone or plastic for added mechanical strength and protection. The fabrication of the silica fibres by the author is discussed in more detail below.

## 3.1 Fabrication of Rare Earth-doped Fibres

Fabrication of fibre preforms can be divided into three main groups. The first group is the vapor phase method [106] commonly known as chemical vapour deposition (CVD) and has derivatives such as modified chemical vapour deposition (MCVD), vapour axial deposition (VAD) and outside vapour deposition (OVD). These techniques principally involve the creation of cladding and core layers by depositing layers of glass that have been formed by vapour reactions onto a glass tube or a seed rod. The second group is a liquid phase, melt/casting process [107] where the preform is made by drawing molten core and cladding glass from a cast or mould. This group of techniques are primarily used for fabricating fluoride glass fibres [108]. The third group of techniques is the solid phase method [109], namely the 'rod in tube' (RT) and modified rod in tube (MRT). These principally involve inserting a rod of core glass into a cladding glass tube with a lower refractive index. The silica fibres used in this work were fabricated using the MCVD technique with the rare earths being incorporated via solution doping. This method is a four stage process. The stages are:

1. deposition of the cladding and core layers,
2. solution doping,
3. consolidating and collapse,
4. drawing.

These stages are discussed in further detail below.

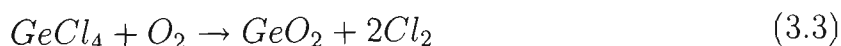
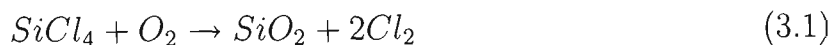
### 3.1.1 Deposition

The basic principle behind the MCVD method of fabrication is that the core and cladding layers are produced by depositing oxides of silica onto the inner walls of a silica glass tube, or substrate. The core layers include other dopants such as germanium (Ge) and phosphorus (P) to adjust the optical and thermal properties of the glass. In particular, both Ge and P increases the refractive index of the glass but

P is used principally to soften the glass allowing it to collapse and melt at a lower temperature.

Figure 3.1 is a schematic of the fabrication process. Oxygen ( $O_2$ ) is pumped into chambers containing the chloride bases of silica ( $SiCl_4$ ) and phosphorus ( $POCl_3$ ) to produce chloride and oxygen vapours. This mixture is carried into a silica glass substrate in the form of a tube which is rotating on a lathe. The traversing burner provides the heat allowing the chlorides and oxygen to react by thermal oxidation according to the reactions shown by equations 3.1 and 3.2. Fine particles of oxides are produced and deposited onto the substrate wall. The oxides are fused onto the glass due to the high temperature ( $1400^\circ C$ ) and layers of glass accumulate as the burner traverses back and forth along the substrate to form the cladding.

The core layers are deposited in the same manner but at a lower temperature ( $1000^\circ C$ ) so that the core layers are not fully sintered. The resulting deposited layers are 'sooty' and porous and appear white. The porosity of the core layers allow the rare earths to be absorbed into the core at the solution doping stage. During the deposition of the core layers, care must be taken to ensure that the reaction temperature remains constant over all the core layer deposits and along the fibre preform. Varying temperatures result in varying porosity of the deposited layers. This alters the absorption of the rare earth ions during the solution doping stage, hence concentrations may vary with layers and along the preform length. During deposition of the core layers, germanium is also added according to equation 3.3 to increase the refractive index of the core layers.



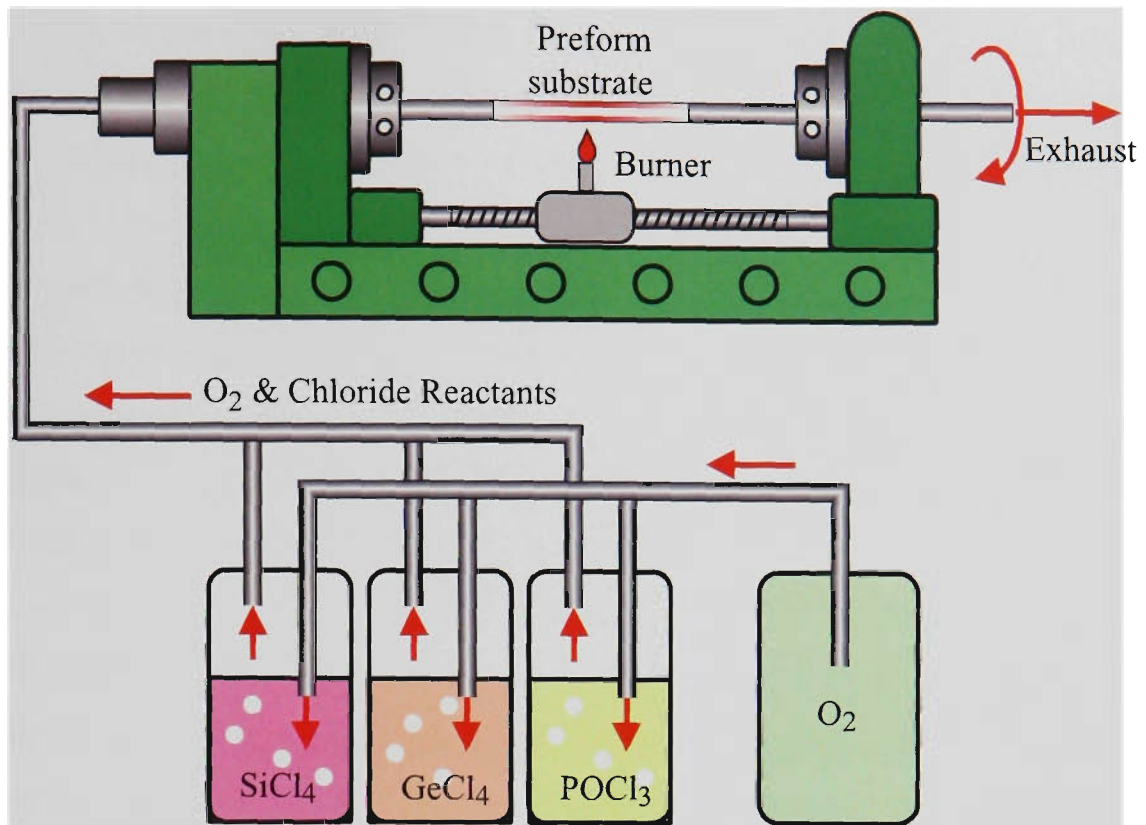


Figure 3.1: Schematic diagram of the preform deposition lathe.

### 3.1.2 Solution doping

Once the cladding and core layers have been deposited, the substrate is removed from the lathe and filled with a methanol solution containing rare earth salts (e.g.  $\text{ErCl}_3$ ). The solution is then left for two to three hours to allow the rare earths to impregnate into the pores. It has been found that the rare earth concentration within the drawn fibre under constant conditions is directly proportional to the rare earth chloride concentration in the alcohol solution for concentrations up to  $10^4$  ppm [109]. Thus dopant concentrations can be adjusted by varying the rare earth chloride concentration in the alcohol solution. It is important to note that such direct relationships can only be achieved under the same fabrication conditions with a consistent fabrication process where the burner temperatures and chamber temperatures are kept constant from preform to preform as well as keeping solution doping times constant.

Aluminium (Al) is also added during the solution doping process to increase the

solubility of the glass to prevent clustering of the rare earth ions. Glass is made up of network formers such as  $\text{SiO}_2$  and  $\text{GeO}_2$  in a covalently bonded structure. In multi-component glass, the glass may also contain network modifiers, such as  $\text{Na}^+$  and  $\text{Ca}^{2+}$ , that break up the bonds in the network. Rare earths are trivalent (e.g.  $\text{Er}^{3+}$ ) and can replace the modifiers in the network allowing for the incorporation of rare earth concentrations of a few percent by weight [110]. However, in pure silica-based glass, used for optical fibres, there is an absence of network modifiers resulting in a structure that is rigid and lacking in solubility. This lack of solubility makes the coordination of rare earth ions difficult leading to clustering of the rare earths in the glass. It has been suggested that, without the addition of network modifiers, the optimum  $\text{Er}^{3+}$  concentration in silica glass is less than 100 ppm before clustering occurs, causing deterioration of amplifier properties [39]. To increase the solubility of the glass, it is necessary to incorporate modifier ions that will break up the network and improve solubility, even for low doping concentrations. Aluminium is incorporated as an aluminium salt ( $\text{AlCl}_3$ ) dissolved in the alcohol solution along with the rare earth salts. The  $\text{AlCl}_3$  solution concentrations that were used in this work were 0.05 - 0.5 mol/l for the six erbium-doped fibres fabricated by the author. Aluminium also acts to increase the refractive index of the core [107].

After the solution has been left to impregnate and absorb into the soot, the remaining solution is carefully drained out of the substrate tube. The doped substrate is then vigorously dried with a burner to remove any remaining solvent. This is a necessary procedure in the solution doping process as incomplete drying results in the creation of air bubbles during the fusing stage and increased losses due to  $\text{OH}^-$  absorption.

### 3.1.3 Fusing and collapsing

Once dried, the substrate is then heated gradually from  $1000^\circ\text{C}$  to the fusing temperature of  $1400^\circ\text{C}$  to fuse the core layers and make the tube substrate transparent. The substrate is then heated further to  $1500^\circ\text{C}$  to collapse into a solid rod known as a preform.

### 3.1.4 Drawing

Once the preform has been fabricated it is drawn into fibre using a drawing tower as shown in figure 3.2. The preform is held above the furnace in a mount that feeds the preform into the furnace at a predetermined speed ( $\approx 1$  mm/min). The preform is initially lowered into the furnace such that the end of the preform is just below the hot zone of the furnace. As the furnace heats up to  $1900^{\circ}\text{C}$ , the preform softens at the hot zone and begins to neck and elongate. The resulting ‘teardrop’ falls under gravity and further elongates the neck to the desired fibre diameter. The teardrop is then cut off and the fibre is fed into the capstan and the fibre take-up drum.

Below the furnace is a non-contact diameter monitor that measures the diameter of the drawn fibre. This measured diameter is compared with a set value, or desired diameter, and the difference is used to control the speed of the capstan at the bottom of the tower. The capstan is sped up to reduce the diameter or is slowed down to increase the diameter.

Immediately below the diameter monitor is the coating applicator. The applicator is simply a well with a hole  $250\ \mu\text{m}$  in diameter and contains softened silicone. As the fibre is drawn through the hole, it is coated by the silicone which is then cured as it passes through an ultra-violet (UV) curing oven. The coated fibre then passes through the capstan and finally onto a take-up drum.

It is likely that during the drawing stage, the drawn fibre experiences stress as it is pulled under high temperature and then quickly cooled. This stress is frozen into the fibres during drawing and can affect the refractive index profile of the fibre [111]. One can then expect some physical properties of the fibre to be different to the preform that it was drawn from. Indeed, Huntington *et al* has verified that diffusion of dopant materials in a fibre coupler has occurred after drawing [53].

Drawing Tower

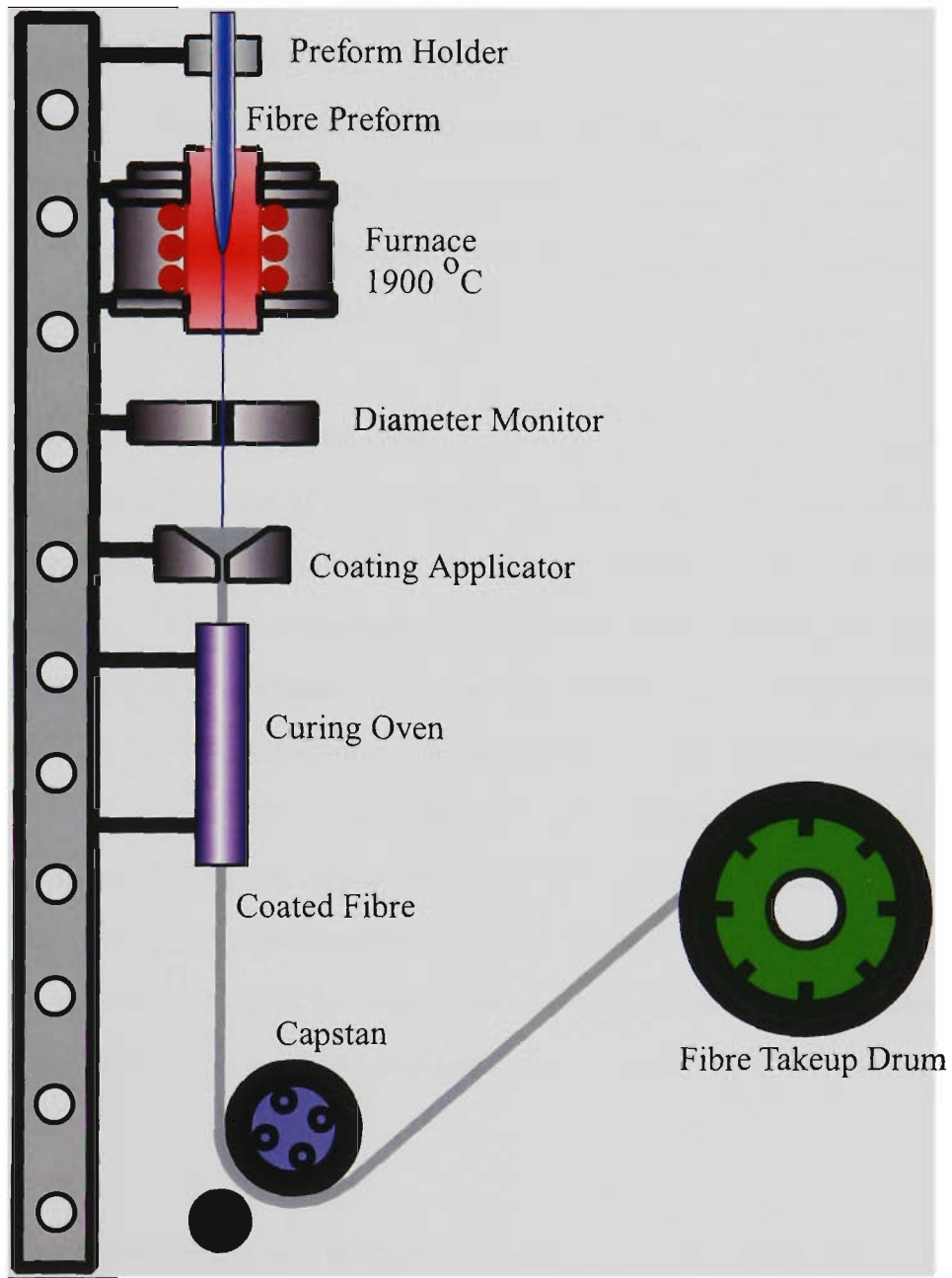


Figure 3.2: Schematic diagram of the fibre drawing tower.

## 3.2 Fibre Characteristics

A total of eleven preforms and their fibres were fabricated and used in this work. These include six Er-doped fibres and five Er:Yb-codoped fibres. They are identified as Er1 to Er6 and YbEr1 to YbEr5 for the Er-doped and Er:Yb-codoped fibres respectively (refer to table 3.1). Of the six Er-doped fibres, two were fabricated by other members of the LPMC. They are Er1 and Er4. These fibres varied slightly in composition and deposition procedure to the fibres made by the author. These differences may cause variations in the spectroscopic properties between individual fibres (e.g. changes in absorption and emission). The Er:Yb-codoped fibres were each doped with equal concentrations of  $\text{Er}^{3+}$  and  $\text{Yb}^{3+}$ .

The refractive index (RI) profiles of the preforms were measured using a commercially available refractometer (P101 Preform Analyser by York Technology). A typical RI profile is shown in figure 3.3. The RI is measured relative to the RI of an index-matching liquid that surrounds the preform in the Preform Analyser. The index-matching liquid is aliphatic hydrocarbon hydrogenated terphenyl which has a RI of 1.4587 at 25°C. The RI of the index-matching liquid varied with temperature at a rate of  $\frac{dRI}{dT} = -3.88 \times 10^{-4}/^\circ\text{C}$  at 580 nm. The vertical scale in figure 3.3 represents the RI difference between the preform and the index-matching liquid measured at 21°C. There is a noticeable depression in the refractive index at the centre of the core. This depression is caused by evaporation of germanium and phosphorus at the inner surface of the preform during collapse due to their instability at high temperatures.

Complications arose during the fabrication of Er6. The high aluminium concentration caused noticeable crystallization in the core. The subsequent collapse resulted in a non-circular preform with an erratic refractive index profile. Only a small section of the preform, that was not visibly crystallised, was drawn into fibre.

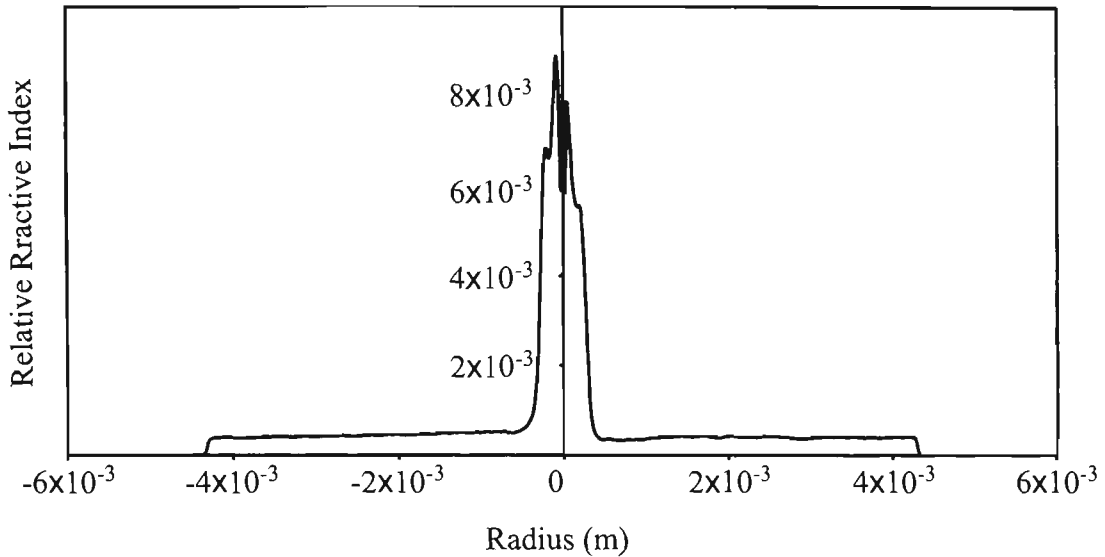


**Figure 3.3:** The RI profile of preform Er3 measured using the P101 Preform Analyser. The vertical scale represents the difference in RI between the preform and the index-matching liquid at 21°C. The RI of the index-matching liquid at 21°C was 1.4603. The small lack of symmetry about the core centre is due to focusing of the preform analyzer rather than asymmetry in the RI profile.

### 3.2.1 Rare earth concentrations

The dopant concentrations of the fibres were calculated by first measuring their absorption spectra. Fibre absorption was measured using the cut-back method and was performed at the LPMC. In this method a length of fibre is probed with a tunable broad bandwidth light source. This tuning source was achieved using white light from a tungsten globe and a monochromator of 1 nm resolution. The light source was modulated with a mechanical chopper at 27 Hz. The probe light was coupled into one end of the doped fibre via a microscope objective. The other doped fibre end was butt-coupled to a germanium detector. The output of the detector was passed into a lock-in amplifier tuned to the mechanical chopper frequency. The output of the lock-in amplifier was acquired by a data acquisition system on a computer. The computer also controlled the output wavelength of the monochromator. A schematic diagram of the setup is shown in figure 3.4.

The monochromator was tuned in 1 nm steps across a known absorption peak of the doped fibre and a depression in the intensity of the transmission spectra was

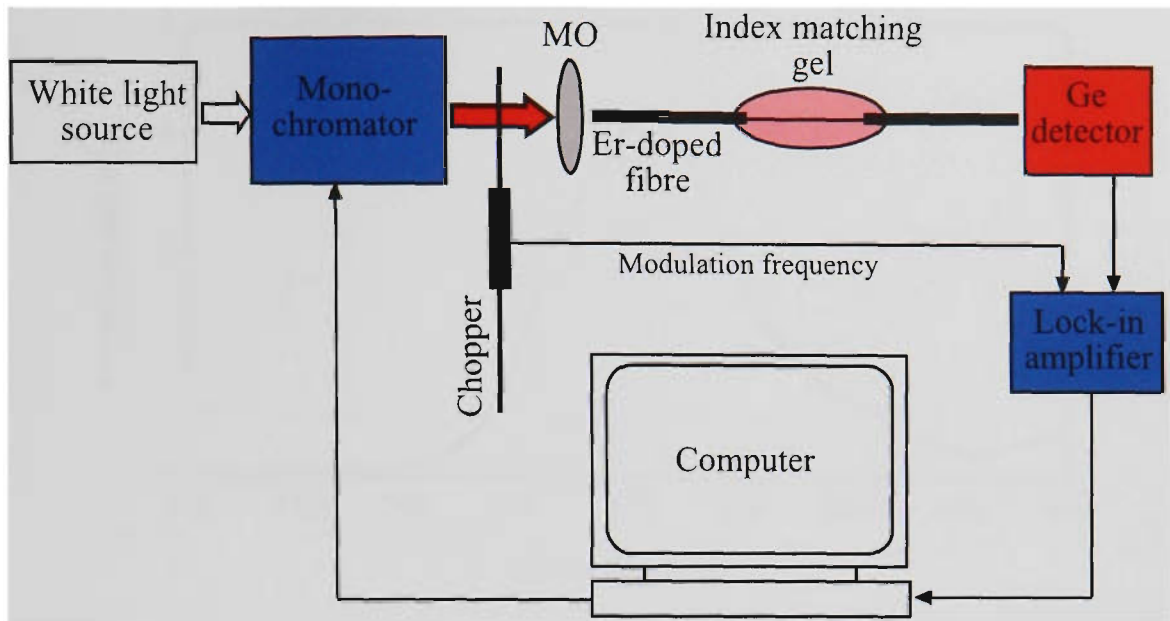


**Figure 3.4:** Experimental arrangement for measuring the fibre absorption spectra.

observed. The strength of the depression, or absorption, is dependent on the dopant concentration and the length of the fibre. The absorption of a fibre was measured for two lengths of the fibre, the difference in absorption between the two fibre lengths gave the attenuation for the difference between the two lengths. The attenuation is expressed in dB/m. A typical spectrum for erbium is shown in figure 3.5 showing absorption from the ground state to the  $^4I_{9/2}$  excited state centered around 800 nm. This wavelength was chosen because of the relatively low absorption at this wavelength compared to other wavelengths [112]. This allows for measurements to be made over longer fibre lengths for increased accuracy and ease of measurement for high dopant concentrations.

In measuring the absorption of the fibres, it is important to ensure that the detected signal has travelled through the core of the fibre only and not through the cladding. Light that is transmitted through the cladding does not experience absorption due to the dopants and is not affected by the cutback of the fibre. Cladding modes represent an offset in the detected signal power. In these experiments, the cladding modes were reduced by stripping a section of the doped fibre and covering it with index-matching gel as illustrated in figure 3.6. This reduces guiding of the

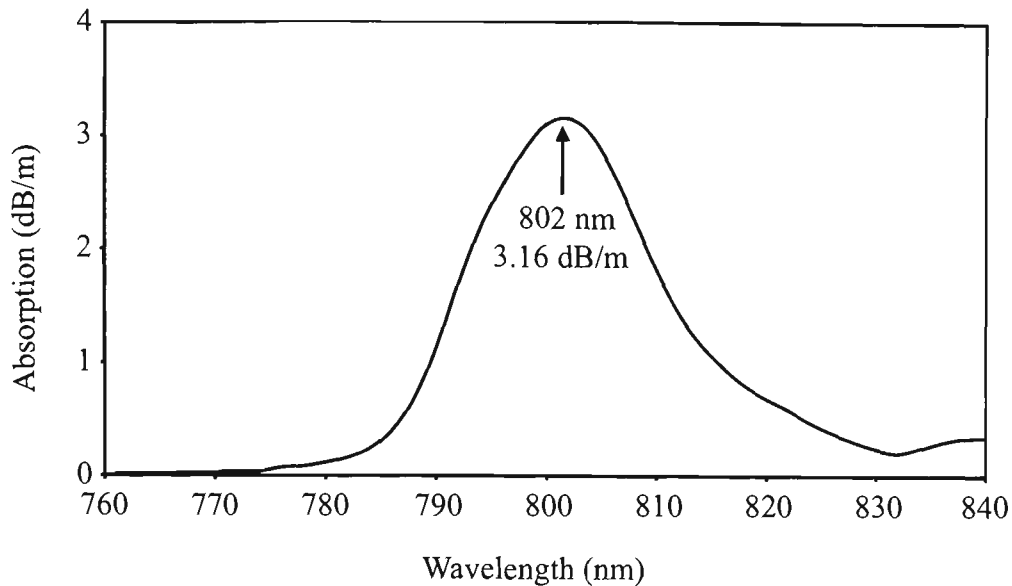


**Figure 3.5:** The absorption spectra of Er<sup>3+</sup> centered around 800 nm.

cladding modes beyond the index-matching gel. Cladding modes were further reduced by bending the fibre at the stripped section to introduce bending loss for the cladding modes.

It is important that there are no variations in the coupling and detection of the signal when using the cutback method so as to ensure that the data between two sets of experiments are consistent. Since the measurements are intensity dependent, it is important to ensure that the same amount of light is coupled into the fibre during each cutback. For this reason, the coupled end of the fibre was untouched during measurements, and the detection end was cut. The detected end was cleaved and butt-coupled to a large area detector rather than being coupled via connectors in order to eliminate variations in connector losses.

At very high dopant concentrations, where strong absorption occurs, there is substantial absorption of the launched light, even at very short fibre lengths. Consequently, no variations in the transmission spectra were observed from one fibre length to another. In practise the fibre lengths were limited to working lengths of about 10 cm. For the measurement of the concentration of sample Er<sub>6</sub>, absorption measurements were performed on the preform instead of a length of fibre. The experimental

arrangement for performing this is shown in figure 3.6. The modulated light from the monochromator was focused into the preform core using a  $\times 20$  microscope objective with a numerical aperture of 0.4. This gave a theoretical focused spot size of  $2.5 \mu\text{m}$  for a launched light wavelength at around  $800 \text{ nm}$ . The preform core diameter was approximately  $1 \text{ mm}$ , hence it can be assumed that all the launched light passed through the core of the preform. This is shown schematically in part (A) of figure 3.6. The launch light was then swept in wavelength across the  $800 \text{ nm}$  absorption spectrum to obtain a transmission spectra. The preform was then shifted such that the focus spot of the microscope objective passed through the preform cladding and a transmission spectra was obtained for the cladding propagation. The attenuation was again calculated from the difference between the two spectra given the length of the preform.

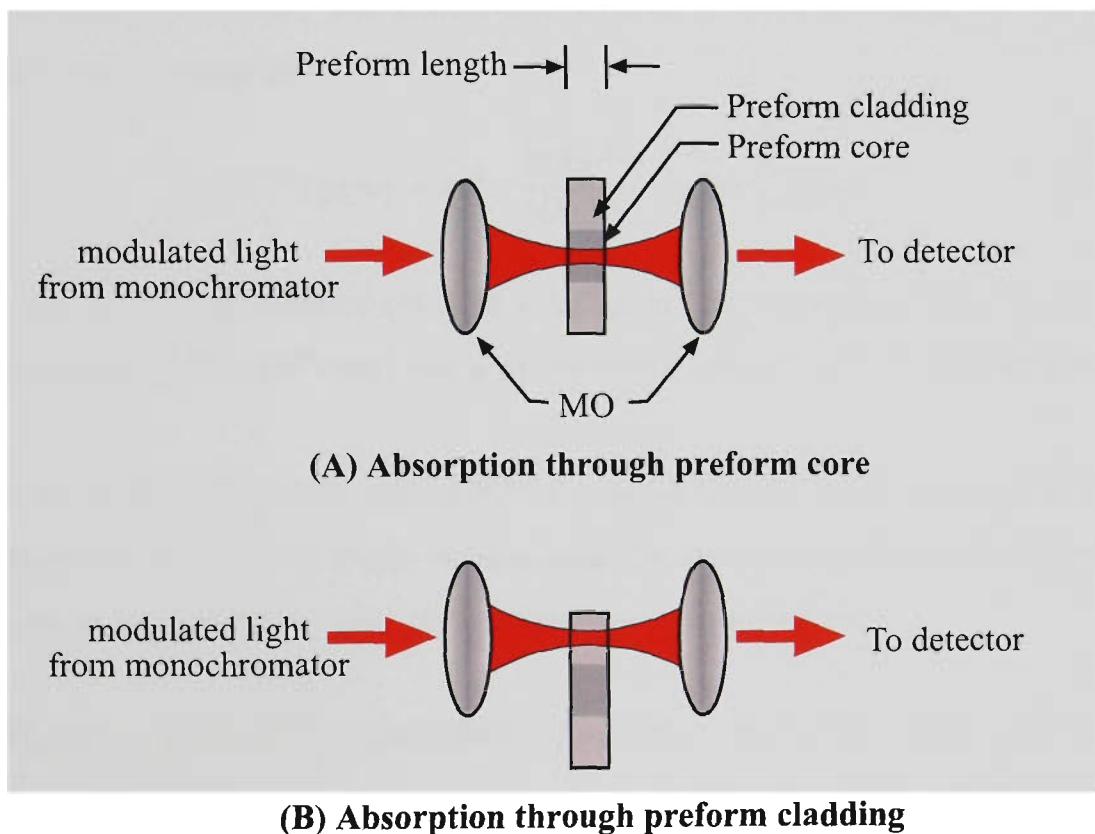


**Figure 3.6:** Experimental arrangement for measuring the preform absorption spectra. Attenuation is performed by first measuring the absorption through the core (A) then through the cladding (B). The attenuation is the difference between the two absorption spectra over the length of the preform section.

Once attenuation peaks were obtained for all samples, they were compared with a reference scale that has been calibrated for absorption at the same wavelength to obtain the dopant concentration of the fibre [113]. This reference scale takes into account the absorption cross section of the rare earth dopants. In this method of comparison, large systematic inaccuracies may arise if the composition of the fibres were not identical to the composition of the reference fibres used to make the calibration scale. Diffusion of dopants in the doping process changes with many variables including the amount of aluminium and other modifiers added, solution doping time and temperature at which the core layers were deposited.

The characteristics for all samples investigated in this thesis are listed in table 3.1 on the next page. The dopant concentrations are listed in units of ppm (%wt) as well as in units of ions/m<sup>3</sup>. The conversion between units of ppm and /m<sup>3</sup> for Er<sup>3+</sup> concentrations is given by

$$\rho(Er^{3+})[ppm] = 10^6 \cdot \frac{Z(Er^{3+})}{D_{Si} \cdot N} \cdot \rho(Er^{3+})[m^3] \quad (3.4)$$

where  $D_{Si}$  is the glass density ( $\approx 2.86 \times 10^6$  g/m<sup>3</sup> for silica glass [2]),  $N$  is Avogadro's number ( $6.02 \times 10^{23}$  mol) and  $Z$  is the atomic weight of Er<sup>3+</sup> (165.93 g/mol).

In the case of praseodymium, where Pr<sup>3+</sup> forms part of the glass matrix, the Pr<sup>3+</sup> concentrations are found by firstly determining the atomic weight of ZBLAN, which is the sum of the atomic weights of the constituent composition.

$$Z(ZBLAN) = ZrF_4(53\%) - BaF_2(20\%) - LaF_3(4\%) - AlF_3(3\%) - NaF(20\%) \quad (3.5)$$

Pr<sup>3+</sup> replaces La<sup>3+</sup> in the glass matrix. For example, a 1% doping concentration of Pr<sup>3+</sup> requires replacing  $LaF_3(4\%)$  in equation 3.5 with  $LaF_3(3\%) + PrF_3(1\%)$ . The atomic weight of the constituent atoms is shown in table 3.2. The number of

Pr:ZBLAN molecules per unit volume is given by

$$\rho(\text{Pr} : \text{ZBLAN}) = \frac{D_{\text{Pr:ZBLAN}} \cdot N}{Z(\text{Pr} : \text{ZBLAN})} [/\text{m}^3] \quad (3.6)$$

where  $D_{\text{Pr:ZBLAN}}$  is the density of Pr:ZBLAN ( $4.51 \times 10^6$  g/mol). The  $\text{Pr}^{3+}$  ion concentration in ppm is given by

$$\rho(\text{Pr}^{3+}) = (\%wt) \cdot \rho(\text{Pr} : \text{ZBLAN}) \quad (3.7)$$

Fluoride glass is typically fabricated using liquid phase, melt casting processes where the rare earth concentration can be tightly controlled during manufacture.

Sample label	Conc. (ppm)	Conc. (ions/m <sup>3</sup> )	Host comp.	Sample type	LPMC label
Er1	176	$1.83 \times 10^{24}$	Si, Ge, P, Al	fibre	Er26
Er2	313	$3.25 \times 10^{24}$	Si, Ge, P, Al	fibre	Er34
Er3	698	$7.24 \times 10^{24}$	Si, Ge, P, Al	fibre	Er33
Er4	3000	$3.11 \times 10^{25}$	Si, Ge, P, Al	fibre	Er6
Er5	4739	$4.92 \times 10^{25}$	Si, Ge, P, Al	fibre	Er36
Er6	7630	$7.92 \times 10^{25}$	Si, Ge, P, Al	fibre	Er35
YbEr1	125	$1.30 \times 10^{24}$	Si, Ge, P, Al	preform	YbEr30
YbEr2	250	$2.59 \times 10^{24}$	Si, Ge, P, Al	preform	YbEr29
YbEr3	500	$5.19 \times 10^{24}$	Si, Ge, P, Al	preform	YbEr28
YbEr4	1500	$1.56 \times 10^{25}$	Si, Ge, P, Al	preform	YbEr27
YbEr5	3000	$3.11 \times 10^{25}$	Si, Ge, P, Al	preform	YbEr26
Pr1	500	$9.43 \times 10^{24}$	ZBLAN	bulk	-
Pr2	2000	$3.77 \times 10^{25}$	ZBLAN	bulk	-
Pr3	4000	$7.54 \times 10^{25}$	ZBLAN	bulk	-
Pr4	10000	$18.86 \times 10^{25}$	ZBLAN	bulk	-

**Table 3.1:** Physical characteristics of the fibres and bulk samples used in this work. Note that for samples YbEr1 to 5, there is an equal amount of  $\text{Yb}^{3+}$  concentration to  $\text{Er}^{3+}$  concentration. The LPMC label represents the sample name as labelled by the Laboratoire de Physique de la Matière Condensée.

Element	Atomic weight (g/mol)
Pr	140.91
Zr	91.22
Ba	137.34
La	138.91
Al	26.98
Na	22.99
F	18.998

**Table 3.2:** Atomic weight of the elements that make up the fluoride glass ZBLAN.

## Chapter 4

# Erbium-doped Fibres

The investigation of fluorescence lifetime begins by looking at the fluorescence lifetime in erbium. It has been previously observed that the fluorescence lifetime is affected by concentration [33]. It is this relationship between erbium dopant concentration and its fluorescence lifetime that is studied in detail here. Of the possible radiative transitions that arise in erbium-doped silica fibres, the 1550 nm and 550 nm fluorescence are the most dominant. The 550 nm (green) fluorescence is well suited to imaging because of its short wavelength. Intensity imaging of the 550 nm fluorescence has been demonstrated by Uttamchandani *et al* and Othonos *et al* using confocal microscopy with sub-micron resolution [57, 58]. This chapter looks at the lifetime of both the 1550 nm and the 550 nm fluorescence. The 1550 nm fluorescence originates from the  $^4I_{13/2}$  excited state while the 550 nm fluorescence originates from the  $^4S_{3/2}$  excited state with both transitions terminating at the  $^4I_{15/2}$  ground state.

The fluorescence lifetime is determined using direct fluorescence decay measurements. In this technique, the excitation source is modulated with a square wave or a pulse. During the ‘on’ time of the modulation, the erbium ions are excited and the resulting fluorescence decays during the ‘off’ time of modulation. In most cases, the decay is a single exponential and the lifetime of the decay can be extracted by fitting the decay curve to an exponential function.

### 4.1 1550 nm Fluorescence

It is well known that the lifetime of the 1550 nm fluorescence is affected by dopant concentration and its effects on amplifier gain and performance have been studied

extensively [34, 39, 114]. The reduction in the fluorescence lifetime due to pump power has also been previously reported [62]. In this chapter, a consolidated model incorporating both concentration and pump power dependence is developed and then compared with the experimental data. This model was developed by the author and published in conference proceedings in 1999 [115, 116]. Since then an identical model was published in a refereed journal by others in 2000 who are not associated with the author [117]. Although the models are identical, the analysis of the models differed in that this work also models the lifetime's dependence on pump power as well as the erbium concentration. Hwang only noted that the lifetime decreased with pump power but did not model the behaviour.

#### 4.1.1 1550 nm Fluorescence Lifetime Modelling

The 1550 nm fluorescence is a particularly important transition because of its use in telecommunications. Figure 2.4 shows some possible cooperative energy transfer processes involving two and three ions. There are many CET processes that involve the  ${}^4I_{13/2}$  energy level. These processes are often seen as parasitic because they compete with the signal amplification. Rate equations can be written for all possible transitions arising from excitation from the ground state to the  ${}^4I_{13/2}$  excited state as are shown in figure 4.1.

$$\frac{dN_4}{dt} = \sum_{i=1}^3 \omega_{i4} N_i + \frac{1}{2} \alpha N_2^2 - \sum_{j=1}^3 (A_{4j} + \omega_{4j}) N_4 - \Gamma_{43} N_4 \quad (4.1)$$

$$\frac{dN_3}{dt} = R_{13} N_1 + \omega_{13} N_1 + \omega_{23} N_2 - \sum_{j=1}^2 (A_{3j} + \omega_{3j}) N_3 - (\Gamma_{32} + \omega_{34}) N_3 + (\Gamma_{43} + A_{43} + \omega_{43}) N_4 \quad (4.2)$$

$$\frac{dN_2}{dt} = \sum_{i=3}^4 (A_{i2} + \omega_{i2}) N_i + \omega_{12} N_1 - A_{21} N_2 - \sum_{j=1, j \neq 2}^4 \omega_{2j} N_2 - \alpha N_2^2 + \Gamma_{32} N_3 \quad (4.3)$$

$$\frac{dN_1}{dt} = \sum_{i=2}^4 (A_{i1} + \omega_{i1}) N_i - R_{13} N_1 - \sum_{j=2}^4 \omega_{1j} N_1 + \frac{1}{2} \alpha N_2^2 \quad (4.4)$$

where  $R$  is the pump rate,  $A$  is the spontaneous radiative emission rate,  $\Gamma$  is the non-radiative (phonon) relaxation rate,  $\alpha$  is the energy transfer coefficient,  $\omega$  is the

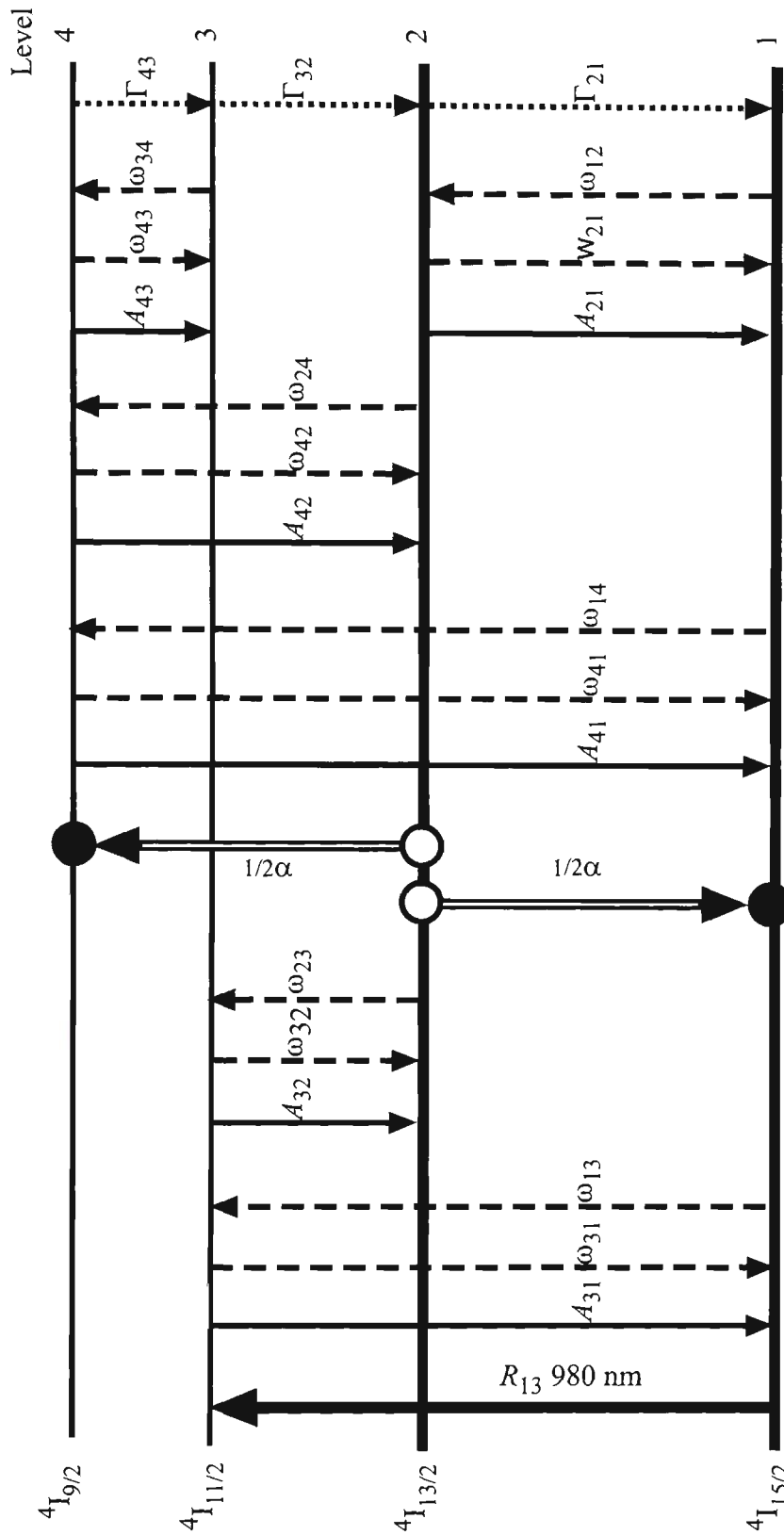


**Figure 4.1:** Schematic diagram of transitions arising from pumping of the ground to the  $4I_{11/2}$  state with a 980 nm laser. The solid lines represent spontaneous emission while the dashed lines represent stimulated emission or reabsorption. The dotted lines are non-radiative phonon decay. The double-lined arrows represent transitions due to energy transfer. The subscripts denote the originating and terminating energy states respectively.

stimulated emission or absorption rate and  $N$  is the dopant population. The subscripts,  $ij$  represent the originating and terminating levels respectively. In other literature, the  $\alpha$  in equations 4.1, 4.3 and 4.4 includes a factor of two to reflect a two-ion process [118].

These rate equations assume no ESA. This assumption may be justified as there is no excitation during the 'off' time of modulation to cause ESA. In addition, the 980 nm pump transition exhibits negligible ESA in silica-based hosts owing to the short lifetime of the  $^4I_{11/2}$  pump state. The pump that is absorbed into this state rapidly decays to the long-lived  $^4I_{13/2}$  metastable state. Under low pump conditions, only this metastable state and the ground state is appreciably occupied [119]. Furthermore, the pump wavelength can be detuned slightly away from the ESA resonance wavelength to reduce the effect of ESA. The following modelling could also be applied to pumping at 1480 nm where no pump ESA is observed.

Table 2.2 shows the phonon (non-radiative) decay rates for various energy levels of erbium in silica. It can be seen that apart from the  $^4I_{13/2} \rightarrow ^4I_{15/2}$  transition, all other energy levels are dominated by very fast non-radiative decay, thus their lifetimes are short. From this, it may be assumed that ions excited to level 3 and level 4 in figure 4.1 will quickly relax via phonon relaxation down to level 2. Experimentally, no fluorescence was observed from levels 3 and 4 when pumped using 975 nm radiation. For the purpose of simplifying the modelling, radiative relaxation from these levels may be neglected and  $A_{43}, A_{42}, A_{41}, A_{32}$  and  $A_{31}$  can be approximated to zero. At low pump powers, below pump saturation, it is assumed that there is no stimulated emission or reabsorption.

With the pump off ( $R=0$ ), the short lifetimes of levels 3 and 4 result in their populations being instantly depopulated, and equations 4.1 and 4.2 approximate to zero. Equation 4.3 reduces to;

$$\frac{dN_2}{dt} = -A_{21}N_2 - \alpha N_2^2 + \frac{1}{2}\alpha N_2^2 \quad (4.5)$$

That is, all up-conversion due to energy transfer from level 2 to level 4 end up back at level 2. Equation 4.5 simplifies to;

$$\frac{dN_2}{dt} = -(A_{21}N_2 + \frac{1}{2}\alpha N_2^2) \quad (4.6)$$

The dopant concentration,  $\rho$ , can be explicitly added to the rate equations through the relation;

$$\rho n_i = N_i \quad (4.7)$$

where  $n_i$  is the normalised population of level  $i$  with  $n_1 + n_2 + n_3 + n_4 = 1$ . Equation 4.6 becomes;

$$\frac{dn_2}{dt} = -(A_{21}n_2 + \frac{1}{2}\alpha\rho n_2^2) \quad (4.8)$$

Derivation of this rate equation, or similar, have been performed by a number of authors and the assumptions and limitations of this modelling is well understood [114, 120, 118, 117]. The solution to this equation has the form;

$$n_2(t) = \frac{2A_{21}n_2(0)}{2A_{21}\exp(A_{21}t) + \alpha\rho n_2(0)\exp(A_{21}t) - \alpha\rho n_2(0)} \quad (4.9)$$

where  $n_2(0)$  is the initial population of level 2 after the pump has been turned off. As expected, it can be seen from equation 4.9 that the decay  $n_2(t)$  falls as a single exponential in the limit of zero concentration. As the concentration,  $\rho$ , increases the influence of the second exponential becomes stronger and reduces the lifetime of the decay. This is also true for an increase in  $n_2(0)$ , which is a function of pump power. The reduction in the overall lifetime is not due to a faster decay rate of the second exponential, as might be expected in a double exponential decay.

The lifetime is defined as the time taken for the decay to reduce to  $1/e$  of its maximum value.

$$n_2(t_e) = \frac{n_2(0)}{e} \quad (4.10)$$

The solution for the lifetime for equation 4.9 then takes the form;

$$t_e = \frac{1}{A_{21}} \ln \left( \frac{2eA_{21} + \alpha\rho n_2(0)}{2A_{21} + \alpha\rho n_2(0)} \right) \quad (4.11)$$

The solution shows that the fluorescence lifetime of the  ${}^4I_{13/2}$  state has a dependence on both the dopant concentration initial population of the level. The initial population,  $n_2(0)$ , is dependent on the pump power. As expected, the lifetime in equation 4.11 reduces to  $1/A_{21}$  in the limit of zero concentration. Figure 4.2 is a plot of the lifetime as a function of both the initial population and dopant concentration based on this model. The plot shows a region in the low concentration regime where the lifetime is not affected by either concentration or pump power. However, at high concentrations the pump rate becomes more influential decreasing the lifetime with pump power.

In fitting the measured lifetimes to equation 4.11, it is necessary to calculate the normalised initial excited state population,  $n_2(0)$ . This may be done by solving the steady state solution to the rate equation for the  ${}^4I_{13/2}$  level with the pump on to obtain the fluorescence saturation level. The steady state solutions for the four energy levels shown in figure 4.1 are;

$$\frac{dN_4}{dt} = \frac{1}{2}\alpha N_2^2 - \Gamma_{43}N_4 = 0 \rightarrow \frac{1}{2}\alpha N_2^2 = \Gamma_{43}N_4 \quad (4.12)$$

$$\frac{dN_3}{dt} = RN_1 + \Gamma_{43}N_4 - \Gamma_{32}N_3 = 0 \rightarrow RN_1 + \Gamma_{43}N_4 = \Gamma_{32}N_3 \quad (4.13)$$

$$\frac{dN_2}{dt} = \Gamma_{32}N_3 - \alpha N_2^2 - A_{21}N_2 = 0 \rightarrow \Gamma_{32}N_3 = \alpha N_2^2 + A_{21}N_2 \quad (4.14)$$

$$\frac{dN_1}{dt} = \frac{1}{2}\alpha N_2^2 + A_{21}N_2 - RN_1 = 0 \rightarrow \frac{1}{2}\alpha N_2^2 + A_{21}N_2 = RN_1 \quad (4.15)$$

Substituting equations 4.12 and 4.13 into equation 4.14 yields

$$RN_1 = A_{21}N_2 + \frac{1}{2}\alpha N_2^2 \quad (4.16)$$

The total dopant population is

$$\rho = N_1 + N_2 + N_3 + N_4 \quad (4.17)$$

The fast lifetimes of level 3 and 4 means that their populations,  $N_3$  and  $N_4$ , are always near zero. The total population is then approximated by

$$\rho = N_1 + N_2 \quad (4.18)$$

Applying equation 4.18 to equation 4.16 yields

$$\frac{1}{2}\alpha\rho N_2^2 + (A_{21} + R)N_2 - R\rho = 0 \quad (4.19)$$

Equation 4.19 is a quadratic and has solutions of the form

$$N_2 = \frac{-(A_{21} + R) \mp \sqrt{R^2 + (2A_{21} + 2\alpha\rho)R + A_{21}^2}}{\alpha} \quad (4.20)$$

The physically correct solution is

$$N_2 = \frac{-(A_{21} + R) + \sqrt{R^2 + (2A_{21} + 2\alpha\rho)R + A_{21}^2}}{\alpha} \quad (4.21)$$

### 4.1.2 Limitations to the Model

The model developed above assumes that energy transfer occurs between ion pairs only, and does not take into account energy transfer between more than two ions such as that shown as process f in figure 2.4. Three-ion process becomes more probable only at very high pumping which increases the population of the excited state and the likelihood of three ions interacting with each other.

In addition, the model also assumes the dopants to be homogeneously distributed in the host. The effects of clustering have not been considered. Clustering occurs

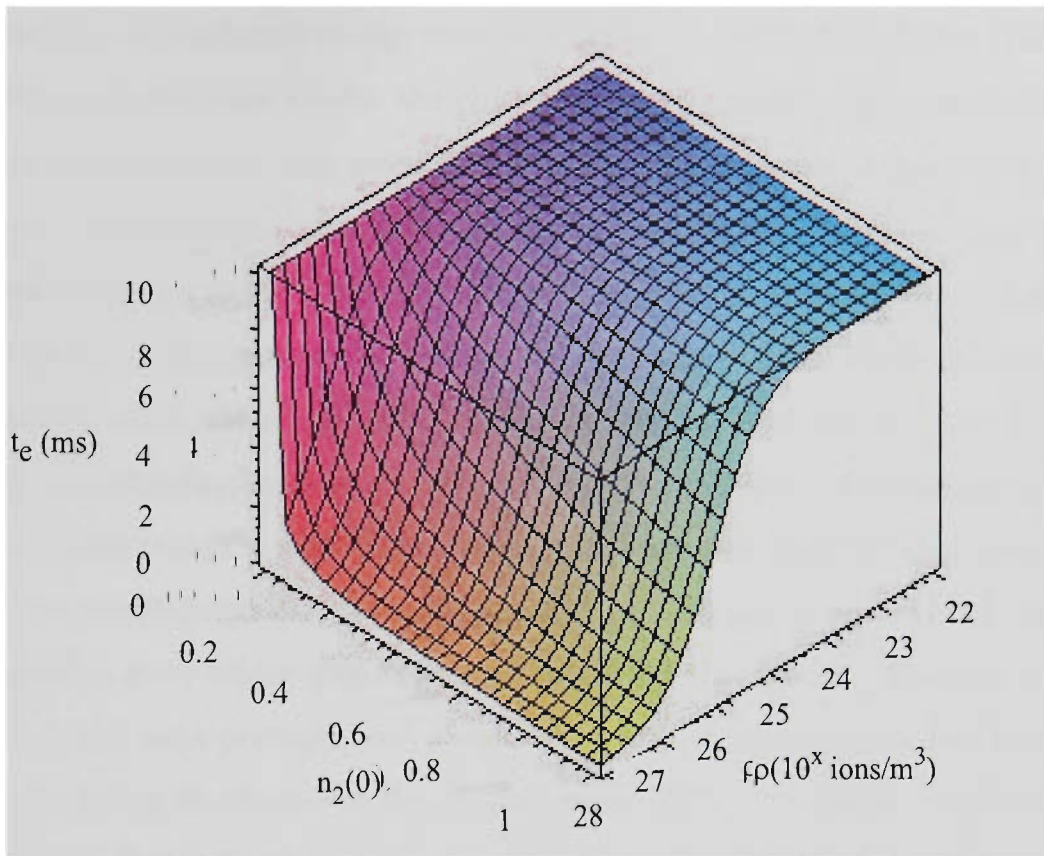


**Figure 4.2:** Plot of the 1550 nm fluorescence lifetime as a function of dopant concentration and initial excited state population. The value for  $\alpha$  was approximated as  $4 \times 10^{-24}$   $m^3/s$  based on the Forster/Dexter ion-ion exchange model [86].

when there are high dopant concentrations and there are not enough available sites in the host for the dopant ions to diffuse into. As a result, the dopant ions tend to aggregate in groups called clusters. Each cluster contains large numbers of ions closely grouped together. This close spacing allows the ions to exchange energy readily and strong energy transfer occurs within the cluster.

Clustering phenomena have been studied previously with early modelling being based on the ion-pair model [33, 62]. This is similar to the ion-pair energy transfer in the model proposed in this work. However, this approach does not fully describe the observation of non-saturable absorption of the 980 nm pump or increased green fluorescence caused by excited state absorption or up-conversion.

More recent modelling of clustering assumes large groups of ions in the clusters

where one ion can exchange energy with any other ion within the cluster [118, 121]. Each pair of excited ions within the cluster exchanges energy instantaneously and the donor is demoted to the ground state while the acceptor is promoted to the  $^4I_{9/2}$  state. The acceptor may then do one of two things. Firstly, it can quickly relax back down to the  $^4I_{13/2}$  state by phonon decay where it participates in another energy transfer with another excited ion in the same cluster which is also in the  $^4I_{13/2}$  excited state. Secondly, the subsequent relaxation of the acceptor from the  $^4I_{9/2}$  state is cascading and occurs via the  $^4I_{11/2}$  excited state. Because of the large number of ions within a cluster, there is an increased probability that ions in the  $^4I_{11/2}$  state can undergo excited state absorption with a pump photon to promote it to the  $^4F_{7/2}$  level where green fluorescence could then occur. The first of these processes is the most probable and a succession of these energy transfers lead to all but one ion being de-excited to the ground state. This total rapid de-excitation of all ions in the cluster leads to non-saturable absorption (NSA) of the 980 nm pump [121, 120]. This is catastrophic for population inversion and stimulated emission and leads to degradation of laser or amplifier performance.

Measurement of NSA can determine the proportion of ions that are clustered and ions that are homogeneously distributed. Maurice *et al* has found that the proportion of clustered ions could be up to 52 % for Er dopant concentrations of 2500 ppm [121]. Thus the effective concentration is 52% less than the expected concentration. Evidence of clustering can also be found by measuring the green fluorescence arising from ESA of the 980 nm pump [122]. Inspection of the green fluorescence as a function of pump power show double saturation behavior with single ion saturation at low pump powers and clustered ion saturation at high pump power. This double saturation is modelled by separately treating single ions and clustered ions, then adding their contributions to the excited state populations. Quimby *et al* found that clustered ions contributed more in assisting ESA than unclustered ions leading to observation of double saturation in the fluorescence [122]. Clustering did not contribute significantly to the 1550 nm fluorescence indicating that the observed fluorescence was predominantly from homogeneously distributed ions.

The strong intra-cluster energy transfer processes severely deplete the ion population in the  ${}^4I_{13/2}$  metastable level but do not contribute to the 1550 nm fluorescence. The fluorescence that is observed is therefore due to the homogeneously distributed ions. In addition, the intra-cluster processes are rapid and their lifetimes are very fast compared to the homogeneous decay lifetime. If it is assumed that clustered ions do not interact with non-clustered ions, then intra-cluster processes do not affect the fluorescence lifetime of the homogeneous processes. Thus intra-cluster processes could not be observed on the time scale of the homogeneous fluorescence decay, hence, is not included in the modelling. The degree of clustering can be reduced by the addition of high concentrations of aluminium as described in the previous chapter.

Another assumption that is made in this model is that all other processes that terminate at the  ${}^4I_{13/2}$  state are also considered fast compared to the time scale of the 1550 nm fluorescence. These processes include cascading phonon decays originating from the  ${}^4F_{7/2}$  state and the  ${}^4I_{9/2}$  and  ${}^4I_{11/2}$  states. Their contributions to the  ${}^4I_{13/2}$  state population are implicitly included in  $n_2(0)$  in the model at the onset of decay.

### 4.1.3 Experimental Arrangement

The experimental setup used for measuring the fluorescence lifetime is shown in figure 4.3. Light from a 975 nm high-NA fibre-pigtailed laser diode was collimated and focussed into the erbium-doped fibre by a  $\times 20$  microscope objective to increase coupling efficiency. This magnification power was required to produce a spot size small enough to focus into the core. The 1550 nm fluorescence from the doped fibre was filtered by a narrow pass filter centered around 1535 nm with a FWHM of 10 nm and collected by an InGaAs detector. The fluorescence was captured on a digital oscilloscope and recorded on to a computer via GPIB connection from the oscilloscope. The doped fibres were 10-15 cm long. The resulting fluorescence peaked at 1535 nm. Side fluorescence was detected so as to reduce any influence due to am-

plified spontaneous emission (ASE). Fluorescence at the start of the dope fibre at the pump end was collected to reduce the effects of pump power decay along the fibre.

For measurement of lifetimes, it is necessary to pulse-pump the erbium-doped fibre and observe the fluorescence immediately after the pump is turned off. The off time of the pump cycle should be at least three times as long as the maximum expected lifetime for adequate sampling of the fluorescence decay since the lifetime is defined as the time taken for the decay to reduce to  $\frac{1}{e}$  of its initial value. For the 1535 nm fluorescence, the expected lifetime is in the order of 10 ms (or 100 Hz) [83]. Thus the pumping period should be no less than 30 ms (or no more than 33 Hz). In these experiments, the pump was modulated at 5 Hz. The long pump time also allowed the fluorescence levels to reach steady state equilibrium before the onset of decay.

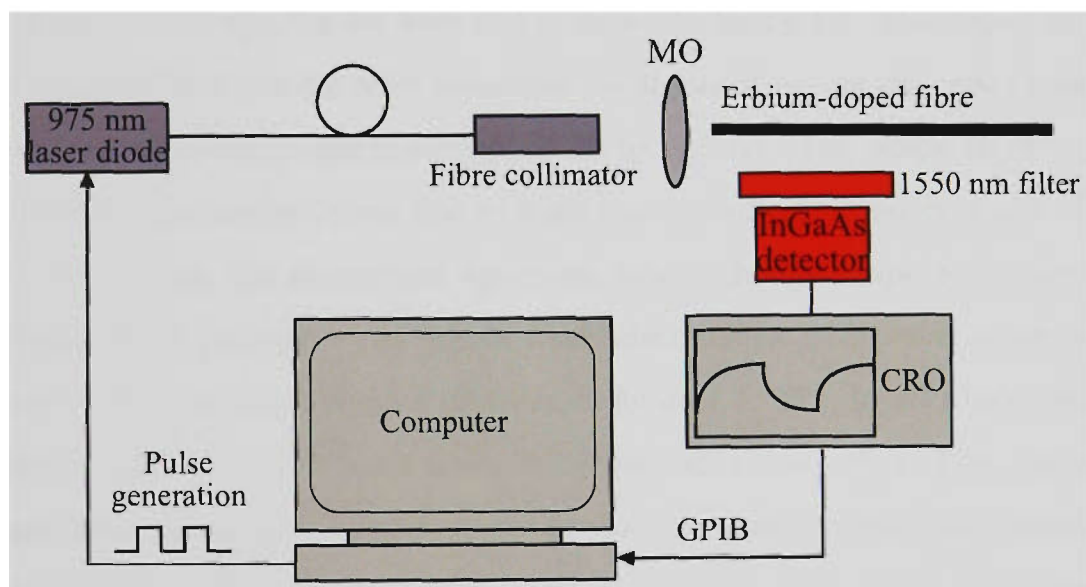


**Figure 4.3:** Experimental arrangement for measuring the 1535 nm fluorescence lifetime in fibres. 975 nm light from a laser diode was collimated and launched into the EDF using a  $\times 20$  microscope objective (MO). The side fluorescence from the EDF was filtered with a 1535 nm filter and collected using an InGaAs detector. The decay was observed on a digital oscilloscope (CRO) before being recorded on to a computer. The computer also controlled the modulation of the laser diode using square waves.

The fall time of the modulation source must be fast compared to the fluorescence

decay time to ensure that the excitation pulse dies quickly and the observed decay is that of the intrinsic fluorescence and not due to the excitation source. The response time of detection must also be much quicker than the decay time of the fluorescence to ensure reliable measurement of the lifetime. The response time of the detection system was limited by the load resistance across the photodiode detector and was measured to be 15  $\mu\text{s}$ .

#### 4.1.4 Experimental Results

Fluorescence decays were captured for all the erbium-doped fibres. For each fibre, the fluorescence was measured at different pump powers from 4 to 50 mW. The pump power was measured between the microscope objective and the doped fibre in figure 4.3. Prior to measuring the fluorescence decay, the fluorescence spectra was observed with pumping in continuous-wave mode using an optical spectrum analyzer. Fluorescence spectra for fibre Er4 is shown in figure 4.4. The doped fibre was 10 cm long and the spectra were measured co-propagating (as this was experimentally easier to do) for pump powers from 20 to 50 mW. The shape of the spectra is consistently maintained from low to high powers indicating no evidence of ASE. When ASE occurs the absorption spectrum would change shape and some Stark transitions would increase while others would decrease as ASE power is taken away from them. This is not strongly noticeable in figure 4.4. The doped fibres used were coated with silicone, which has a lower refractive index than silica. This can act like a second cladding allowing more fluorescence to propagate longitudinally outside the core and reducing the effects of ASE. With the lack of ASE in the co-propagating fluorescence, it can be assumed that there is no ASE in the transverse fluorescence.

The decay traces were averaged 256 times using the averaging feature of the digital oscilloscope. Up to 20 averaged decays were made at each pump power. Before the decay curves could be fitted to the model, it was necessary to convert equation 4.9 from units of a normalized population to a voltage as measured by the detector. The normalized initial population,  $n_2(0)$ , is related to the decay amplitude by the

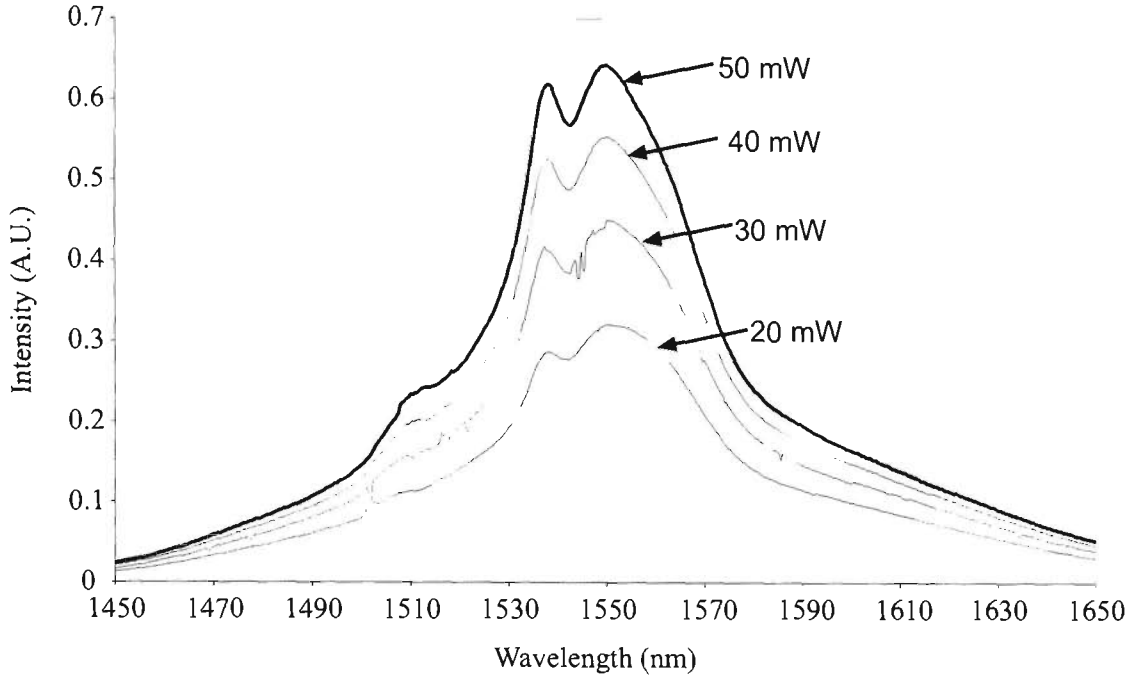


**Figure 4.4:** 1550 nm fluorescence spectra of Er4 pumped at 20 to 50 mW.

relation

$$n_2(0) = \frac{N_2(0)}{\rho} = \frac{V(0)}{V_{sat}} \quad (4.22)$$

where  $V(0)$  is the decay voltage amplitude (maximum voltage at time  $t = 0$ ) and  $V_{sat}$  is the pump saturation voltage. In fitting the model to the decay, equation 4.9 was simplified to ease the fitting process. This simplification involved replacing  $\alpha\rho$  with a single variable  $\beta$ . Equation 4.9 then became

$$V(t) = \frac{2A_{21}V(0)}{2A_{21}\exp(A_{21}t) + \beta\left(\frac{V(0)}{V_{sat}}\right)\exp(A_{21}t) - \beta\left(\frac{V(0)}{V_{sat}}\right)} + C \quad (4.23)$$

where  $C$  is an offset voltage due to biasing of the photodetector and background noise and is independent of the properties of the fibre. Equation 4.21 was also modified to convert from physical units into electrical units.

$$V(0) = \frac{-(A + P) + \sqrt{P^2 + (2A + 2BV_{sat})P + A^2}}{B} \quad (4.24)$$

where  $A$ ,  $B$  and  $V_{sat}$  are fitted parameters representing  $A_{21}$ ,  $\alpha$  and  $\rho$  respectively,  $P$  is the pump power. The conversion takes into account conversion efficiencies and factors including solid angle of detection, detector sensitivity and responsivity as

well as pump absorption.  $V(0)$  was measured as shown in the inset of figure 4.5. The pump saturation was determined by fitting the amplitudes against pump power for each fibre using equation 4.24 as shown in figure 4.5 for fibre Er1. The conversion factors cancel out when  $V(0)$  is normalized against  $V_{sat}$ . With the normalized populations determined, the decay curves were then fitted to equation 4.23 to the first 90 ms of data to obtain the parameters  $A_{21}$ , and  $\beta$ . The up-conversion coefficient,  $\alpha$ , could be then extracted by knowing the dopant concentration  $\rho$ . The lifetimes were then calculated using equation 4.11.

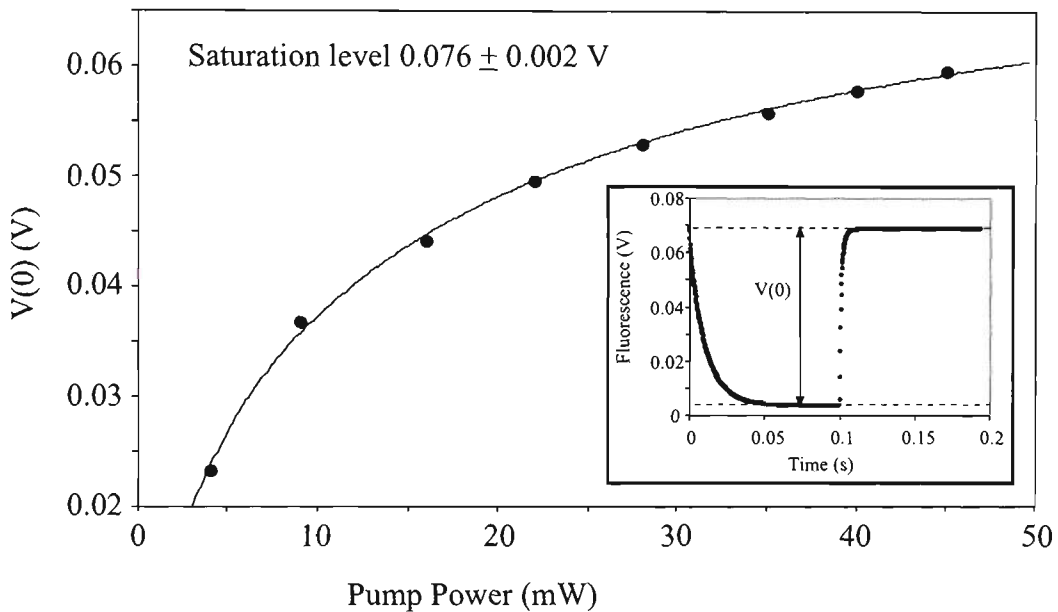


**Figure 4.5:** Plot of the decay amplitude as a function of pump power for fibre Er1. The plot was fitted using equation 4.24 to determine the fluorescence saturation. An example of measuring the decay amplitude is shown as an inset for the fibre pumped at 50 mW.

As a comparison, the decay curves were also fitted to a single exponential function to extract the decay lifetime directly. The results for the two methods were in good agreement with each other with variations in the lifetimes being less than 5% for all the fibres except Er6. In the case of Er6, a faster component of the decay was observed and the decay no longer fitted the single exponential. There were significant differences in the lifetimes for the two methods. The model yielded better fits for all the fibres, including Er6, with the regression squared coefficient ( $r^2$ ), a

measure of the quality of the fit, being higher than that of the single exponential. A comparison of the model fit and the single exponential fit is shown in figure 4.6 for fibres Er1 and Er6.

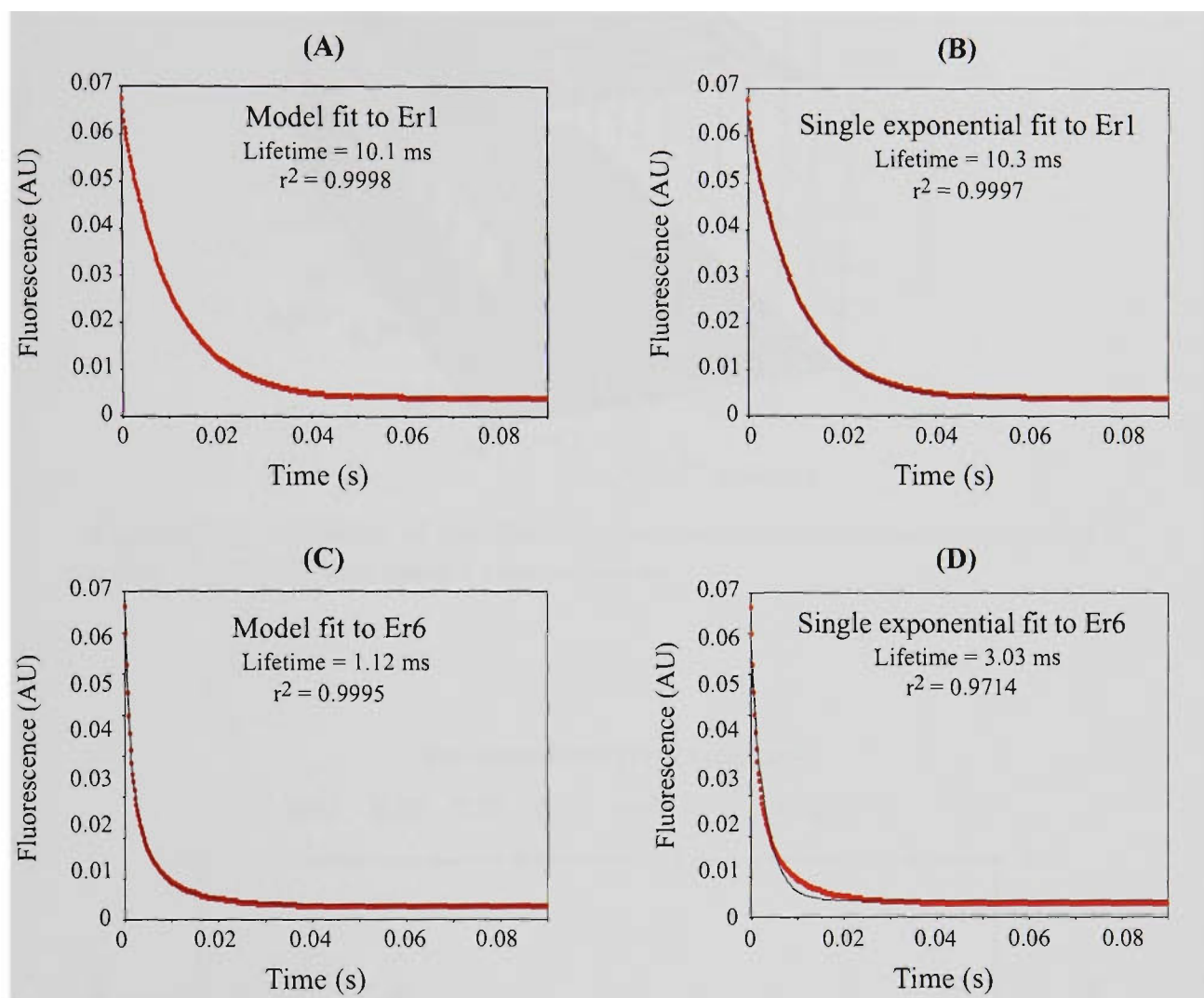


**Figure 4.6:** Fit to the 1550 nm fluorescence decay of Er1 and Er6 pumped at 50 mW. (A) model fit to Er1; (B) single exponential fit to Er1; (C) model fit to Er6 and (D) single exponential fit to Er6. The fitted lifetimes and the regression squared coefficients ( $r^2$ ) for each fit are shown as an inset.

The lifetime results are shown in figure 4.7. The lifetime is plotted as a function of the dopant concentration as determined using absorption measurements as described in the previous chapter instead of the effective concentration when clustering is considered. This is so that the trend in the lifetime could be compared to the “true”, or expected concentration instead of the effective concentration resulting

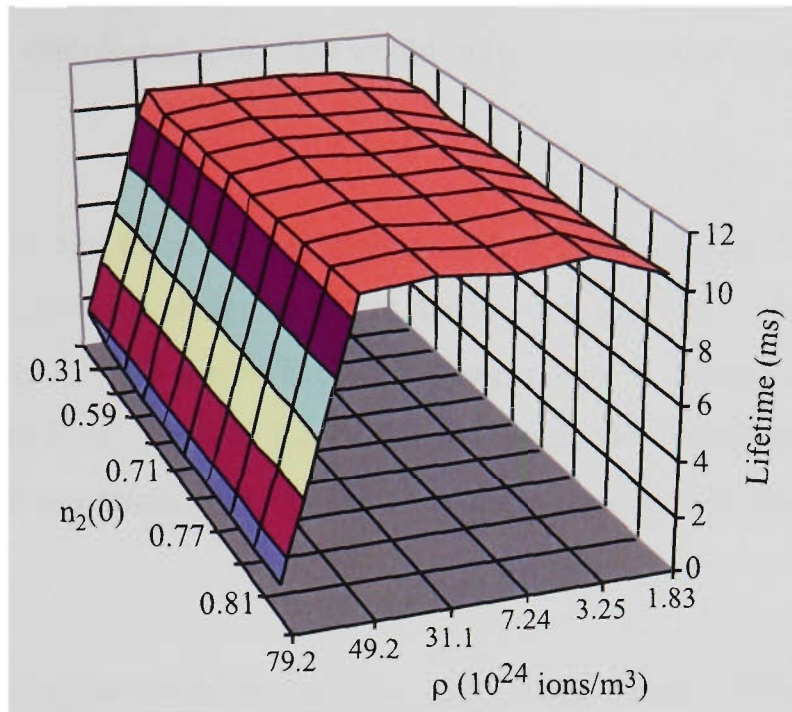


**Figure 4.7:** Variation of the 1535 nm fluorescence lifetime as a function of initial population and dopant concentration

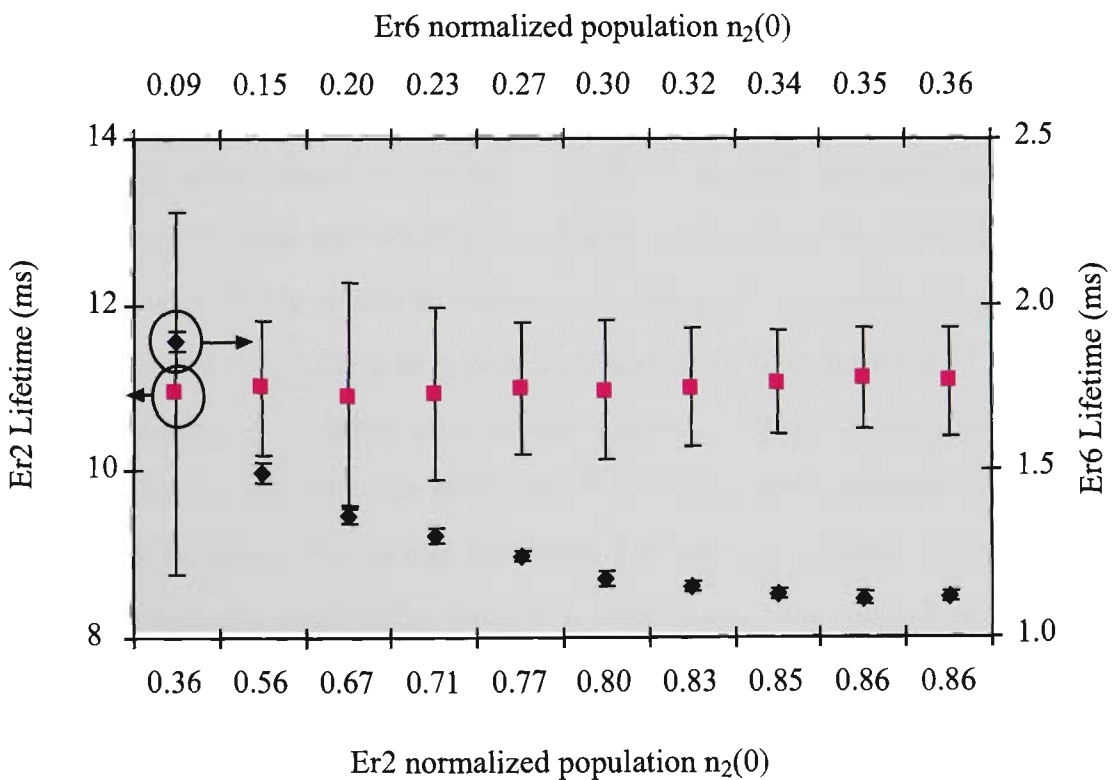


**Figure 4.8:** The fluorescence lifetime of Er2 and Er6 as a function of normalized population.

from clustering. Although clustering would reduce the effective concentration of the homogeneously distributed ions, this would only compress the trend in the lifetime graphs.

The variation in the fluorescence lifetime with normalized population, which relates to pump power, is shown in figure 4.8 for Er2 and Er6. The figure shows a clear decrease in the lifetime of Er6 with pump power as predicted by the model. The large errors in the lifetime for Er2 at low pump powers are due to low signal strengths and a degradation in the signal to noise ratio at low pump and low concentration.

As expected, the radiative decay rate,  $A_{21}$ , did not vary with concentration or pump power. Using the fit,  $A_{21}$  was determined to vary between 102 and 86  $\text{s}^{-1}$ . The fitted values for  $A_{21}$  are shown in figure 4.9. The variations are most probably due to slight differences in the host composition and in the fabrication of the fibres. The radiative decay rates for Er6 were found to vary much more than other samples. As the radiative decay rate is dependent on the host, the variations in  $A_{21}$  for Er6 are most likely due to the crystallization of the preform during fabrication. The average value for  $A_{21}$  was calculated to be 90  $\text{s}^{-1}$  with a standard deviation of 3  $\text{s}^{-1}$ .

The parameter  $\alpha$ , was extracted from  $\beta$  and a plot of  $\alpha$  as a function of dopant concentration and pump power is shown in figure 4.10.  $\alpha$  is also plotted solely as a function of concentration for pump powers 9 and 50 mW in figure 4.11. Both figures show an anomaly in the value of  $\alpha$  at the highest concentration (fibre Er6). The highest value for  $\alpha$  obtained was  $9.97 \times 10^{-23} \text{ m}^3/\text{s}$  for Er6 pumped at 4 mW. However, this may be more due to the fact that Er6 was crystallized during fabrication of the sample and the large value for  $\alpha$  is a reflection of the change in the structure and properties of the fibre. With the exception of Er6, the remaining data in figure 4.11 do show a general decrease in  $\alpha$  with concentration, although this trend is not clear.

In the modelling presented here, the up-conversion coefficient,  $\alpha$ , was assumed to be

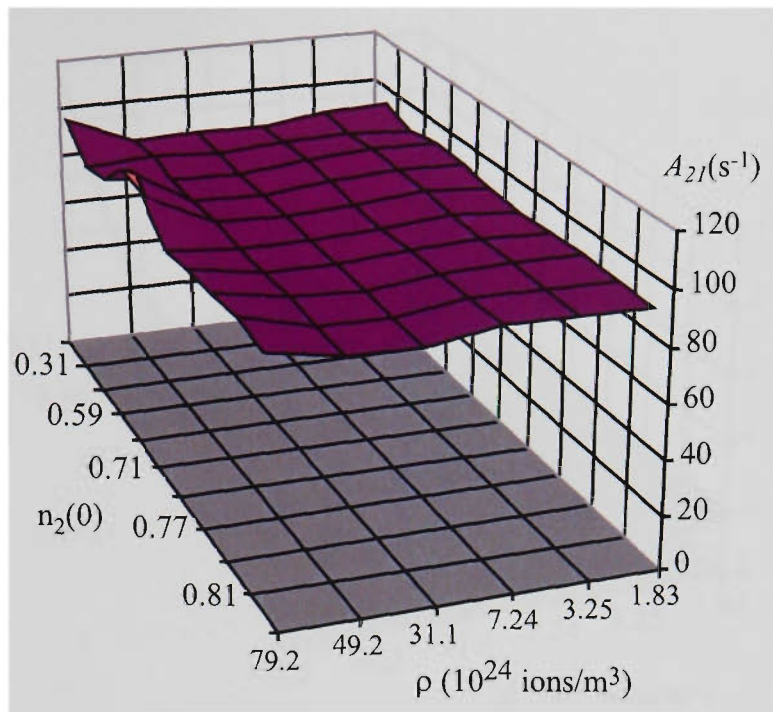


**Figure 4.9:** Variation of the radiative decay rate  $A_{21}$  as a function of initial population and dopant concentration.

constant. Although other reports have also modelled the up-conversion coefficient as being constant, many results have shown  $\alpha$  to vary with concentration. Hehlen *et al* found that the CFUC coefficient increased with  $\text{Er}^{3+}$  concentration in soda lime and aluminosilicate bulk glasses for concentrations up to  $6 \times 10^{26}$  ions/ $\text{m}^3$  [123]. Hwang *et al* also found the CFUC coefficient to increase with  $\text{Er}^{3+}$  concentration in bulk phosphate glass [117]. Others have found the coefficient to be independent of concentration [114] while this work indicates a decrease with concentration, with the exception of Er6. A comparison of values obtained in this work and by others is shown in table 4.1. This table lists the up-conversion coefficients found by other authors for various silica-based hosts.

Inspection of table 4.1 shows a wide range in the values for  $\alpha$  indicating  $\alpha$  to be very host dependent. Hehlen found that the up-conversion coefficients for bulk aluminosilicate glasses were higher than that for bulk soda lime glasses. Even for hosts that are similar,  $\alpha$  can vary by few orders of magnitudes. Take for instance the results found by Blixt *et al* [114] and this work for similar sample types, the difference in  $\alpha$  is two orders of magnitude for the same concentration level. Both van den Hoven

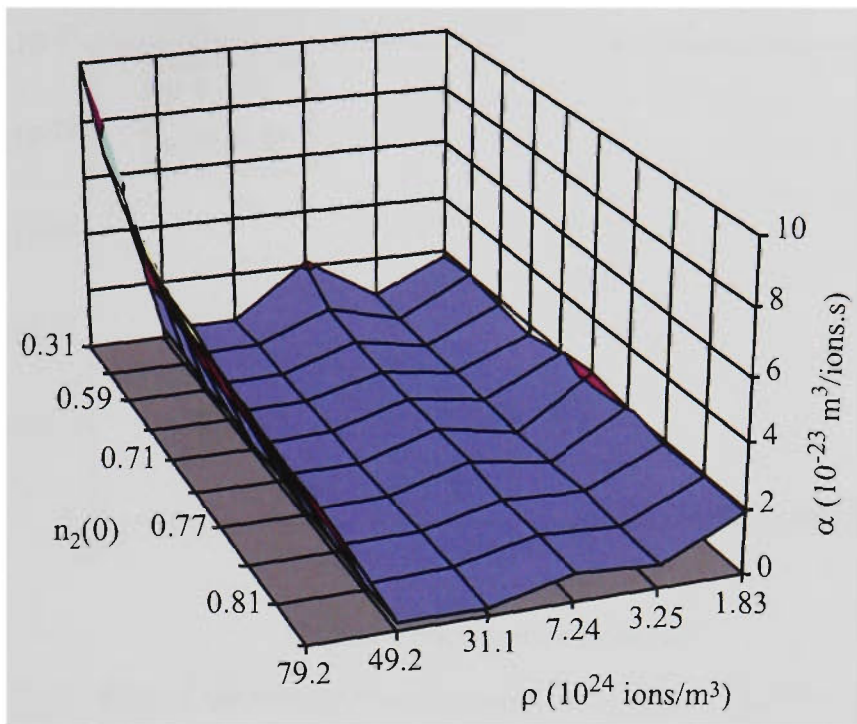


**Figure 4.10:** Variation of the energy transfer coefficient  $\alpha$  as a function of pump power and dopant concentration.

*et al* [125] and Kik *et al* [126] used Er-implanted  $\text{Al}_2\text{O}_3$  waveguides pumped at  $1.48 \mu\text{m}$ , but van den Hoven found the up-conversion coefficient to be two orders of magnitude less than Kik. In addition, the values obtained for  $\alpha$  also show a strong dependence on the method of doping. In the case of Kik *et al* two different doping techniques were applied to two samples of the same host material with same dopant concentrations, there is two orders of magnitude difference in  $\alpha$  for the two samples. Kik concluded that different doping processes affect the inhomogeneous atomic scale spatial distribution of the erbium ions. This would most likely explain the large discrepancy in the values obtained for Er6 and the other fibres. The crystallization of Er6 during preform fabrication would have altered the glass structure of the fibre. Additional stress placed on the glass during fibre drawing would also affect the host characteristics.

Green fluorescence was observed during excitation at high pumping in Er6 and, to a less extent, in Er5. This green fluorescence arises because the combination of high dopant concentration and high pump power increases the probability of ESA from the  $^4I_{11/2}$  level to the  $^4F_{7/2}$  (refer to figure 2.3) [2, 127]. Subsequent relaxation

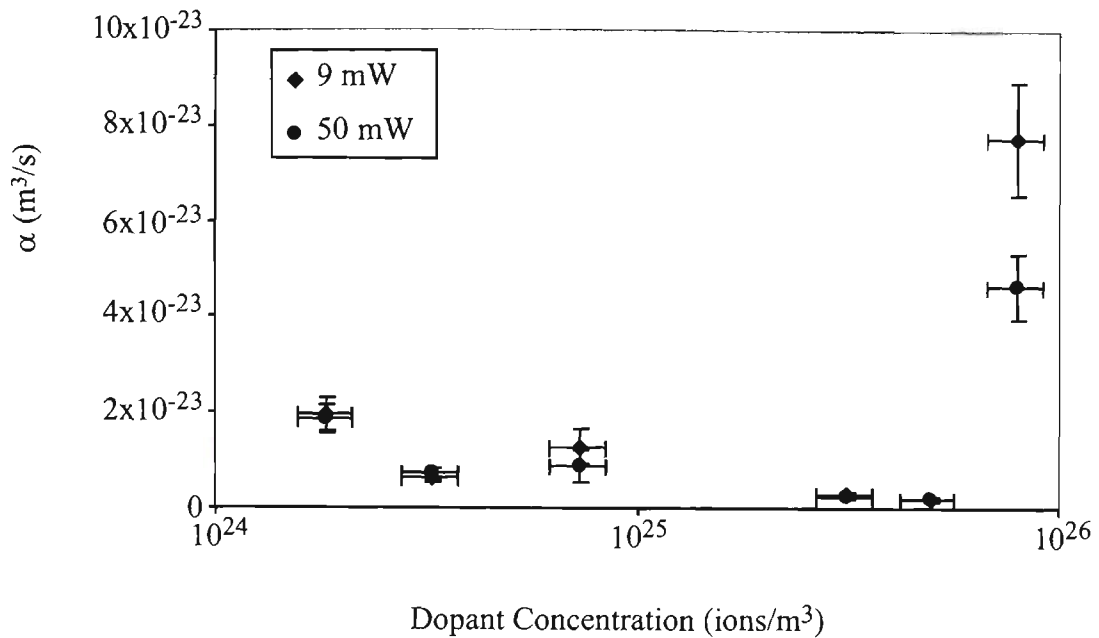


**Figure 4.11:** Plot of the energy transfer coefficient,  $\alpha$ , as a function of dopant concentration for pump powers 9 and 55 mW.

from this level to the ground state produces green emission at around 550 nm via the  $^4S_{3/2}$  excited state. This results in a reduction in the number of ions returning from the  $^4I_{11/2}$  level to the  $^4I_{13/2}$  level and, consequently a reduction in intensity of the 1535 nm fluorescence. This process may also be enhanced by cooperative frequency up-conversion (CFUC) between neighbouring ions in the  $^4I_{11/2}$  level that use the same transitions as that for CFUC in the presence of clustering as discussed previously. Philipsen *et al.* showed this to be possible by comparing the green fluorescence with the 1550 nm fluorescence to obtain quantitative information about the energy transfer up-conversion, although quantitative information about clustering could not be obtained due to the fast nature of processes involving clusters [128]. The high dopant concentration may also increase the probability of three-ion energy exchanges (process f in figure 2.4), having the effect of further increasing the green fluorescence while decreasing the 1535 nm fluorescence.

## 4.2 550 nm Fluorescence

Thus far, the investigation of the 1535 nm fluorescence lifetime has shown this lifetime to be of little practical use as a means of determining concentration. This

Er <sup>3+</sup> conc. (ions/m <sup>3</sup> )	$\alpha$ (m <sup>3</sup> /s)	Glass host	Ref.
$1.83 \times 10^{24} - 7.92 \times 10^{25}$	$1.8 \times 10^{-24} - 9.97 \times 10^{-23}$	Ge/Al/P silica fibre	this work
$2 \times 10^{26} - 4 \times 10^{26}$	$1.6 \times 10^{-24} - 2.2 \times 10^{-24}$	phosphate bulk glass	[117]
$10^{26}$	$3.8 \times 10^{-24}$	sodalime silicate waveguide	[124]
$1.2 \times 10^{26}$	$4 \times 10^{-24}$	ion-implanted Al <sub>2</sub> O <sub>3</sub> waveguide	[125]
$3.43 \times 10^{24}$	$2 \times 10^{-22}$	Ge/Al/P silica fibre	[114]
$5 \times 10^{25} - 5.98 \times 10^{26}$	$2.6 \times 10^{-24} - 1.2 \times 10^{-24}$	sodalime silicate bulk glass	[123]
$4 \times 10^{25} - 4.77 \times 10^{26}$	$3.2 \times 10^{-25} - 1.4 \times 10^{-24}$	aluminosilicate bulk glass	[123]
$3.0 \times 10^{26}$	$3.5 \times 10^{-20}$	ion-cosputtered Al <sub>2</sub> O <sub>3</sub> waveguide	[126]
$2.7 \times 10^{26}$	$4.1 \times 10^{-22}$	ion-implanted Al <sub>2</sub> O <sub>3</sub> waveguide	[126]

**Table 4.1:** Comparison of the up-conversion coefficient measured in this work and by others.

is due to the insensitivity of the lifetime to concentration for dopant levels below  $5 \times 10^{25}$  ions/m<sup>3</sup>. The other dominant fluorescence in erbium-doped silica fibre will now be looked at.

The 550 nm fluorescence originates from the  $^4S_{3/2}$  excited state and terminates at the  $^4I_{15/2}$  ground state. This fluorescence can be produced by direct pumping of the  $^4S_{3/2}$  energy level using 532 nm pump or to higher energy levels such as the  $^4F_{7/2}$  state using 488 nm pump. Alternatively, the  $^4S_{3/2}$  excited state could be populated by excited state absorption of 800 nm and 980 nm photons from the  $^4I_{13/2}$  and  $^4I_{11/2}$  excited states respectively (refer to figure 2.3). Of these two excited state transi-

tions, the 800 nm transition is much stronger because of the longer lifetime of the originating level. Direct pumping to the  $^4S_{3/2}$  state is more efficient than excitation by excited state absorption.

### 4.2.1 Modelling

For the fluorescence lifetime to vary with concentration, there must be cooperative energy transfer effects that take place involving the energy level from which the fluorescence originates. The 550 nm fluorescence originates from the  $^4S_{3/2}$  excited state as shown in figure 4.12 for  $\text{Er}^{3+}$ , and in particular, show that there are more resonant CET transitions involving the  $^2H_{11/2}$  excited state compared to the  $^4S_{3/2}$  excited state.

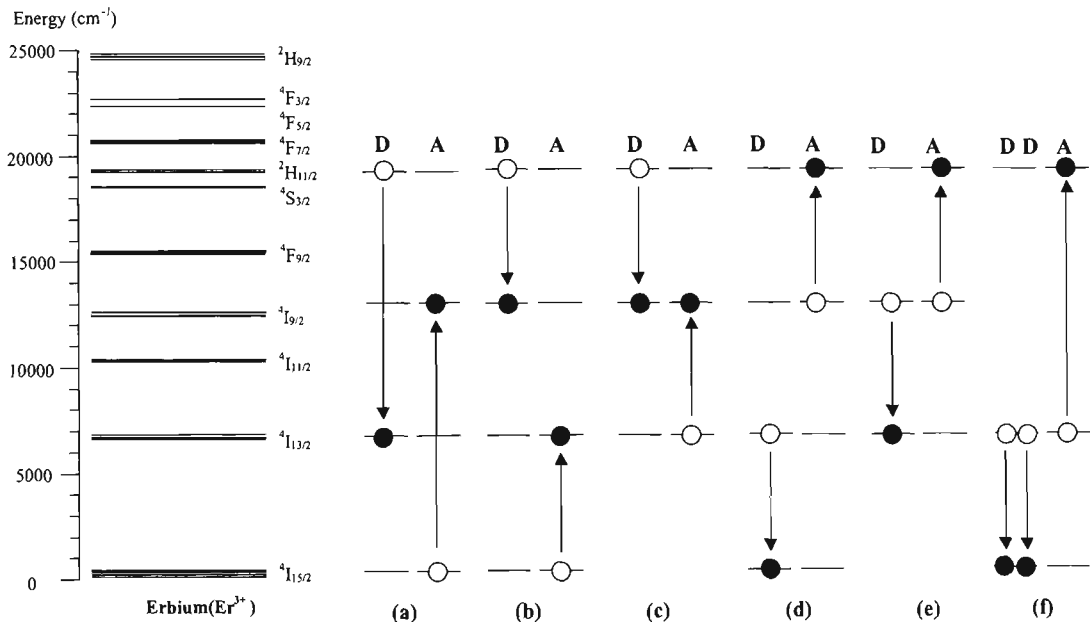


**Figure 4.12:** Simplified diagram of some possible resonant transitions that involve the  $^4S_{3/2}$  excited state that could lead to cooperative energy transfer. The donor is labelled D and the acceptor is labelled A. Open and filled dots represent ions before and after energy transfer respectively.

The close spacing between the  $^2H_{11/2}$  and  $^4S_{3/2}$  states ( $\approx 685 \text{ cm}^{-1}$ ) make them thermally coupled and, in thermal equilibrium, the  $^2H_{11/2}$  state population would only be 3% of the  $^4S_{3/2}$  state population at room temperature. Of the six pro-

cesses shown in figure 4.12 labelled a to f, some are more probable than others as they compete with each other. Transitions where the originating energy levels have longer lifetimes will have higher probabilities than energy levels that have shorter lifetimes. In transition e, both the donor and acceptor originates from the  $^4I_{9/2}$  excited state. The phonon rate for this energy level is high at  $2.91 \times 10^7 \text{ s}^{-1}$  in silica (table 2.2), thus depopulation from this level is rapid and its population is negligible. Cooperative energy transfer with donor ions originating from this level is unlikely in preference of the other processes. The same could be said for level  $^4I_{11/2}$ . This argument also eliminates process d which has one donor originate from the the  $^4I_{9/2}$  state.

Of the three processes a to c, processes a and b are more likely than process c since one of their originating states is the ground state. These three processes have at least one donor originating from the  $^2H_{11/2}$  state. Due to the thermal coupling of the  $^2H_{11/2}$  state with the  $^4S_{3/2}$  state and the short lifetime of the  $^4S_{3/2}$  state, the likelihood of cooperative energy transfer is reduced. Process f involves three ions originating from the  $^4I_{13/2}$  state. The  $^4I_{13/2}$  state has an appreciably long lifetime, thus an appreciable population. Process f would serve to increase the fluorescence lifetime, but its probability is reduced for a three-ion process. Thus, by the process of elimination, one can assume that no cooperative energy transfer takes place that involves the  $^4S_{3/2}$  excited state, hence there is no concentration dependence in the green fluorescence lifetime. Experiments were carried out to measure the lifetime of the green fluorescence by pumping with 488 nm and 800 nm excitation.

## 4.2.2 Experimental arrangement

The experimental arrangement used to produce 550 nm fluorescence is shown in figure 4.13. An argon ion-pumped Ti:Sapphire laser operating at 795 nm was passed through an acousto-optic modulator (AOM). The modulator operated at 10 kHz. This frequency is sufficiently fast but still allowed the  $^4S_{3/2}$  excited state to reach steady state equilibrium before the offset of the pump pulse. The zero order beam was directed to a beam dump while the first order beam was directed towards a dichroic beamsplitter (DB). The beamsplitter, which reflects at 800 nm and trans-

mits at 550 nm, directed the pump beam into the erbium-doped fibre. The counter-propagating fluorescence produced in the erbium-doped fibre passed back through the dichroic beamsplitter and through to a 540 nm notch filter before being detected by a photomultiplier tube (PMT). For pumping using 488 nm pump, the Ti:Sapphire laser was replaced by a single-line argon ion laser operating at 488 nm. The dichroic beamsplitter was replaced by another dichroic beamsplitter with transmission at 488 nm and reflection at 540 nm. The pump and detection arms were swapped such that the pump passed through the beamsplitter whilst the fluorescence signal was reflected from the beamsplitter.

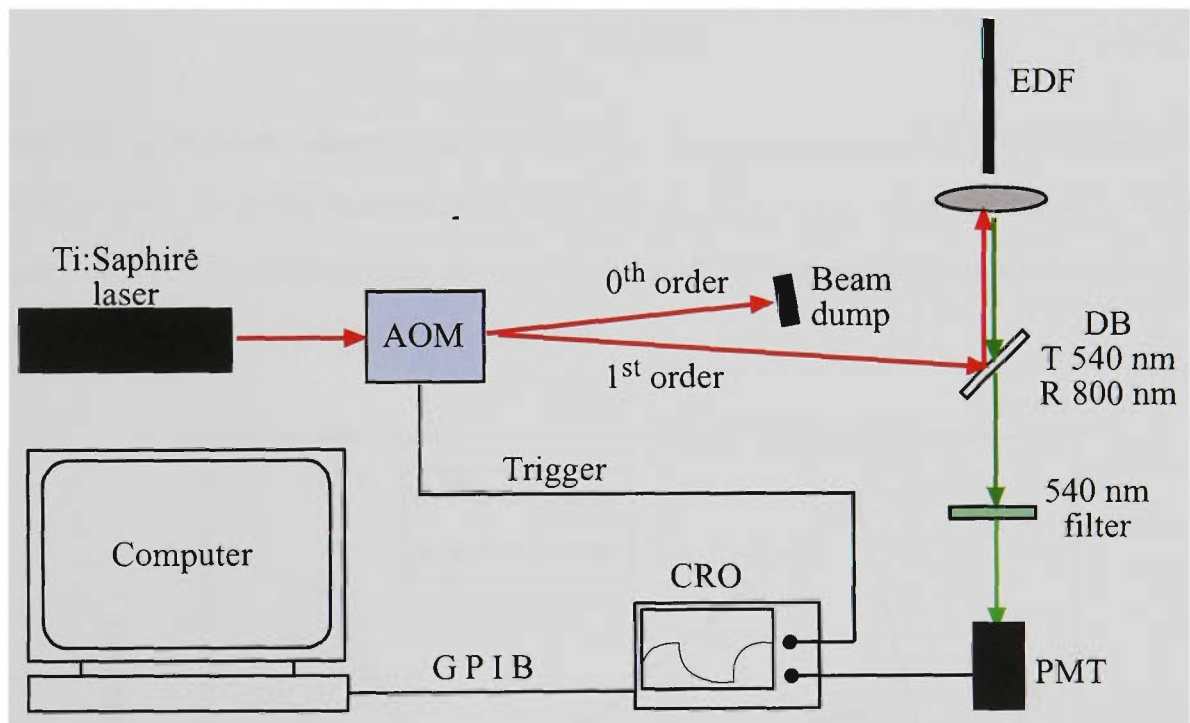


**Figure 4.13:** Experimental arrangement for measuring the 540 nm fluorescence lifetime in  $\text{Er}^{3+}$ -doped fibre pumped at 795 nm.

The modulated signal from the photomultiplier tube was captured on a digital oscilloscope and averaged over 256 traces. The averaged data was recorded on a computer via a GPIB connection. The best response time of modulation and detection obtained was 200 ns. This detection response is long compared to the expected lifetime of the green fluorescence of around 1  $\mu\text{s}$  and adds a 0.02  $\mu\text{s}$  error in the

measured lifetime according to:

$$\tau_{tot} = \sqrt{\tau^2 + \tau_{err}^2} \quad (4.25)$$

where  $\tau$  is the expected lifetime and  $\tau_{err}$  is the response of the detection system.

### 4.2.3 Experimental results

All the fluorescence decays showed single exponential behaviour and were fitted to a single exponential decay described by

$$I(t) = I_0 \exp\left(\frac{-t}{\tau}\right) \quad (4.26)$$

where  $I(t)$  is the time-dependent fluorescence intensity (expressed as a voltage from the detector),  $I_0$  is the fluorescence intensity at time  $t = 0$ ,  $\tau$  is the lifetime of the decay. All of the fluorescence decays fitted well to the single exponential and no multi-exponential behaviour was observed.

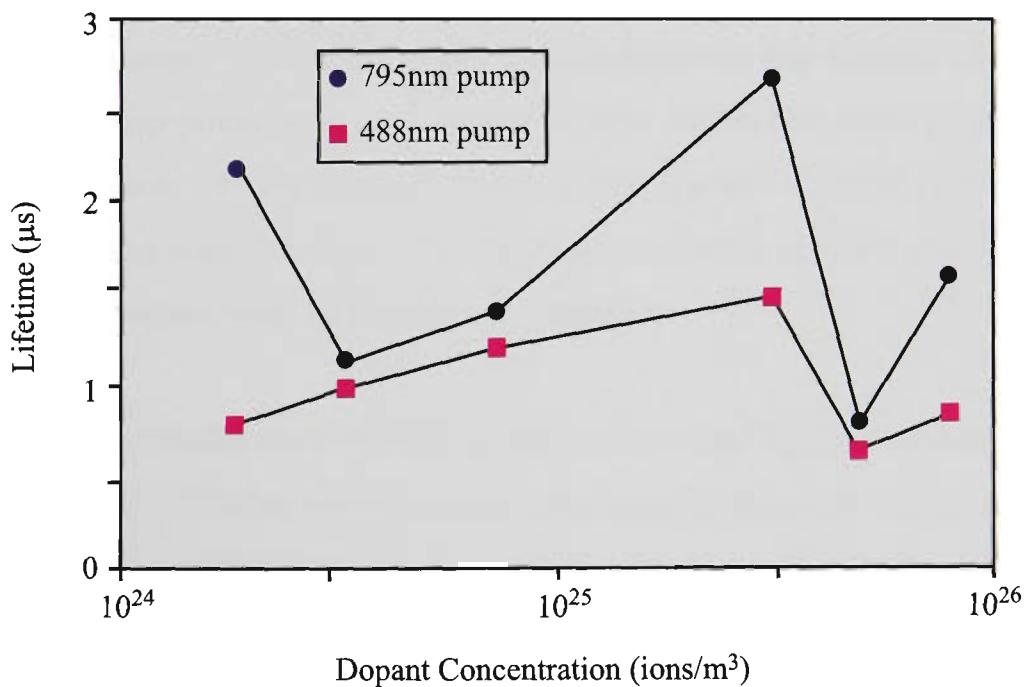


**Figure 4.14:** 540 nm fluorescence lifetime as a function of erbium concentration pumped at 488 nm and 795 nm.

Figure 4.14 shows the lifetime of the 540 nm fluorescence as a function of erbium concentration pumped with 488 nm and 795 nm. The results show little correlation between the lifetimes and erbium concentration suggesting that there are no cooperative energy transfers involving the  $^4S_{3/2}$  excited state, hence no concentration dependence in its lifetime. The measured lifetimes were somewhat erratic showing lack of trend of any sort, suggesting errors in the experiment. However, the exponential fits to the decay curves were good with fitting errors being less than 1% for all cases. Coupled with the 2 % error associated with the slow detection response, the resulting errors were still acceptable. The experiments were repeated several times but all repeats showed consistent lifetime variations suggesting that the behaviours may be more dependent on the glass and fabrication properties.

### 4.3 Conclusion

In this chapter, the lifetimes of the 1535 nm and the 540 nm fluorescence in  $\text{Er}^{3+}$ -doped silica fibre were studied. For the 1550 nm fluorescence, a single model was developed that predicted the dependence of the lifetime on dopant concentration as well as pump power. The model shows a dependence on the lifetime with concentration and pump power with two distinct regions in the behaviour of the lifetime with concentration. At low concentrations, below  $5 \times 10^{25}$  ions/ $\text{m}^3$ , the lifetime is not influenced by concentration. At high concentrations, above  $5 \times 10^{25}$  ions/ $\text{m}^3$ , the lifetime decreases with increasing concentration

Experimental results for the 540 nm fluorescence from the  $^4S_{3/2}$  excited state suggests that there is no correlation between the fluorescence lifetime and erbium concentration. This indicates that there are no concentration-dependent cooperative energy transfer processes taking place involving the  $^4S_{3/2}$  state, hence this transition could not be used for determining erbium concentration.

## Chapter 5

# Yb:Er-codoped Fibre Preforms

Ytterbium is the 14th rare earth element and its energy structure is relatively simple. There are only two energy levels in the optical spectrum, these being the  ${}^2F_{5/2}$  excited state and the  ${}^2F_{7/2}$  ground state. The energy separation between the excited state and the ground state is about  $10200\text{ cm}^{-1}$  [129]. This results in very high quantum efficiencies for excited ions returning to the ground state. In addition, the absorption from the ground state to the excited state is strong compared to other rare earth ions. There is very large Stark splitting within these levels resulting in very broad absorption and emission bands.

By chance, the energy separation in ytterbium corresponds to a wavelength of approximately 980 nm, matching well with the pump band of erbium doped fibre lasers and amplifiers. Due to its strong absorption, ytterbium efficiently absorbs the pump at 980 nm and can transfer this pump energy to erbium. This process is more efficient than directly pumping the erbium alone. Thus, ytterbium has found an important application for increasing the efficiency of pumping Er-doped fibres through the process typically referred to as “sensitization” where  $\text{Yb}^{3+}$  ions act as the sensitizer and  $\text{Er}^{3+}$  ions are the activator [130]. Sensitization using ytterbium with other dopants, such as praseodymium, thulium, holmium, chromium and manganese have also been demonstrated [131, 132, 133, 134, 135]. In this chapter, the fluorescence lifetime of Yb:Er-codoped fibre preforms is investigated. In particular, the motivation is to show a dependence on the lifetime of the  $\text{Yb}^{3+}$  as a function of  $\text{Yb}^{3+}$  and/or  $\text{Er}^{3+}$  concentration. This would provide a means for determining whether the lifetime could be used for determining the concentrations of one or both of the rare earth species.

## 5.1 Modelling

The cooperative energy transfer between  $\text{Yb}^{3+}$  and  $\text{Er}^{3+}$  ions have been studied extensively in bulk glass and optical fibre for many different host types [130, 136, 137, 138]. Figure 5.1 shows some possible energy transfer transitions from  $\text{Yb}^{3+}$  to  $\text{Er}^{3+}$  ions.

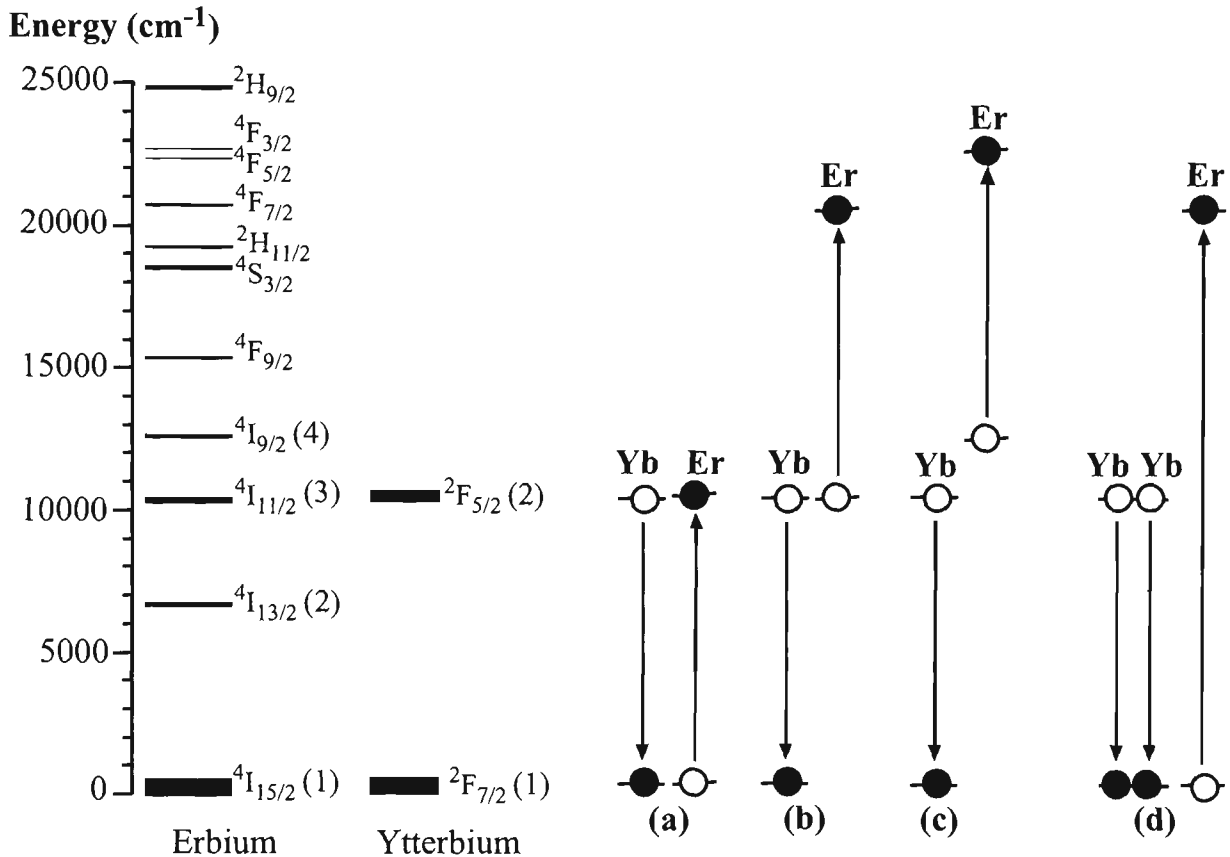


**Figure 5.1:** Schematic diagram of energy transfer transitions between  $\text{Yb}^{3+}$  and  $\text{Er}^{3+}$ . All donors in these processes are  $\text{Yb}^{3+}$  ions whilst the acceptors are  $\text{Er}^{3+}$  ions.

The most dominant of these transitions is process (a) and rate equations governing this process can be readily found in literature. In this work, the fluorescence lifetime of the  $\text{Yb}^{3+}$  component of the codoped system was chosen for investigation. The primary reason for this was the simple energy structure exhibited by  $\text{Yb}^{3+}$  ions. Consider the following model developed based on process (a) in figure 5.1. The rate

equations for the  $\text{Yb}^{3+}$  system can be written as;

$$\frac{dN_{y2}}{dt} = RN_{y2} - A^{rad}N_{y2} - \beta N_{y2}N_{e1} \quad (5.1)$$

$$\frac{dN_{y1}}{dt} = -RN_{y1} + A^{rad}N_{y2} + \beta N_{y2}N_{e1} \quad (5.2)$$

where the subscript letters denote the dopant species and the subscript numbers denote energy levels from their respective dopants as shown in figure 5.1.  $R$  is the pump rate,  $A^{Rad}$  is the natural radiative decay rate of ytterbium and  $\beta$  is the energy transfer coefficient between ytterbium and erbium. Because of the fast nonradiative decay of the level  $^4I_{11/2}$  in erbium, there is negligible back-transfer from  $\text{Er}^{3+}$  to  $\text{Yb}^{3+}$  ions [138]. The following substitution is made for normalised concentrations;

$$\rho_y n_y = N_y \quad (5.3)$$

$$\rho_e n_e = N_e \quad (5.4)$$

With pump off, equation 5.1 reduces to;

$$\frac{dn_{y2}}{dt} = -(A^{rad}n_{y2} + \beta\rho_e n_{y2}n_{e1}) \quad (5.5)$$

At low pumping there is relatively low depopulation of the ground level in erbium, so the assumption can be made that  $n_{e1} \approx 1$  [59]. Equation 5.5 will then have a solution of the form;

$$n_{y2}(t) = n_{y2}(0)\exp^{-(A^{rad} + \beta\rho_e)t} \quad (5.6)$$

and the lifetime,  $\tau_e$ , is given by;

$$\frac{1}{\tau_e} = A^{rad} + \beta\rho_e \quad (5.7)$$

The solution shows that the lifetime of the  $^2F_{5/2}$  level in ytterbium is dependent only on the erbium concentration and is independent of its own concentration. This is expected as ytterbium's simple energy structure does not permit any cross-relaxation between its own kind. This result is similar to that of Golding *et al* in their work with

sensitization from erbium to praseodymium in  $\text{Er}^{3+}:\text{Pr}^{3+}$ -codoped glass [139]. Golding found that the effective lifetime of erbium was dependent on the praseodymium concentration only and independent of its own concentration. Similar modelling has been performed by other authors [117, 138, 140].

## 5.2 Experiment

A typical absorption and emission spectra for  $\text{Yb}^{3+}$  in silica is shown in figure 5.2. Fluorescence corresponding to the transition from the first Stark level of the  $^2F_{5/2}$  excited state to the second Stark level of the ground state was chosen to ensure that the detected radiative emission had indeed originated from  $\text{Yb}^{3+}$  ions. This transition corresponds to a wavelength of around 1040 nm and is shown as transition (d) in the inset in figure 5.2. Although emission at 980 nm is the strongest in ytterbium, this emission wavelength was not chosen because erbium also emits at 980 nm. In addition, the 980 nm wavelength was too close to the pump wavelength.

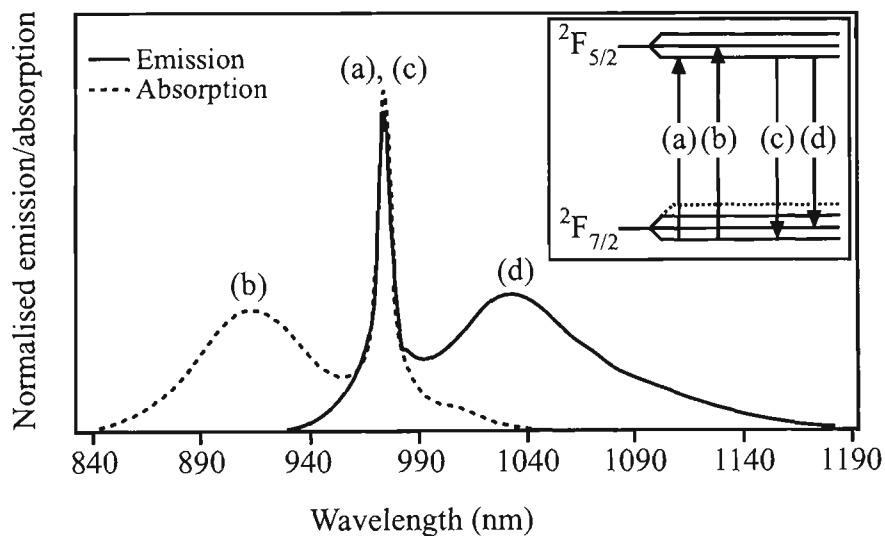


**Figure 5.2:** Normalised emission and absorption spectra for  $\text{Yb}^{3+}$ -doped silica showing the two major peaks for absorption and emission. The inset shows the energy level structure for  $\text{Yb}^{3+}$ . The energy levels in the inset are not drawn to scale [141].

The experimental arrangement used in this section is similar to that shown in figure 4.3. Pump radiation from a 975 nm fibre-pigtailed laser diode was collimated and

focussed into the codoped fibre preform by a  $\times 10$  microscope objective. Side fluorescence from the preform was collected by an InGaAs detector after passing through a narrow-bandpass filter centered around 1032 nm with a FWHM of 10 nm. The fluorescence was captured on a digital oscilloscope and recorded on to a computer via GPIB connection from the oscilloscope. The laser diode was modulated at 40 Hz. The response of the detection circuitry was 15  $\mu\text{s}$ . Fluorescence lifetimes were measured for the five samples labelled as YbEr1 to YbEr5. The preforms were 8.4 to 8.8 mm in diameter and 20 mm long with the core diameters being 0.91 to 0.98 mm. The preforms were fabricated by the author using the MCVD technique and solution doped as described in chapter 3. The solution for YbEr5 was prepared with an equal concentration of  $\text{Yb}^{3+}$  and  $\text{Er}^{3+}$ . This solution was subsequently diluted to vary the concentration for making the other preforms and the ratio of the  $\text{Yb}^{3+}$  to  $\text{Er}^{3+}$  remained fixed at 1:1 for all samples. The modelling indicates that the  $\text{Yb}^{3+}$  fluorescence lifetime was independent of  $\text{Yb}^{3+}$  concentration, hence it was easier to vary the concentration in this way. The Yb/Er concentrations ranged from  $1.30 \times 10^{24}$  to  $3.11 \times 10^{25}$  ions/ $\text{m}^3$  for preforms YbEr1 to YbEr5 respectively.

Fluorescence decays were measured for the five codoped fibre preforms for pump powers from 9 to 50 mW. The pump power was measured before entering the preform. The decays were fitted to an exponential decay described by

$$I(t) = I_0 \exp\left(\frac{-t}{\tau}\right) \quad (5.8)$$

where  $I(t)$  is the time-dependent fluorescence intensity,  $I_0$  is the fluorescence intensity at time  $t = 0$  and  $\tau$  is the lifetime of the decay. All fluorescence decays fitted well to the single exponential and no non-exponential behaviour was observed. This is illustrated in figure 5.3 showing the fluorescence decay and the single exponential fit.

The inset in figure 5.3 shows the first 0.5 ms of decay. The transfer of energy from ytterbium to erbium ions typically occurs on the time of scale of  $\approx 10 \mu\text{s}$ , however, this could not be seen due to the 15  $\mu\text{s}$  response of the detection and there was

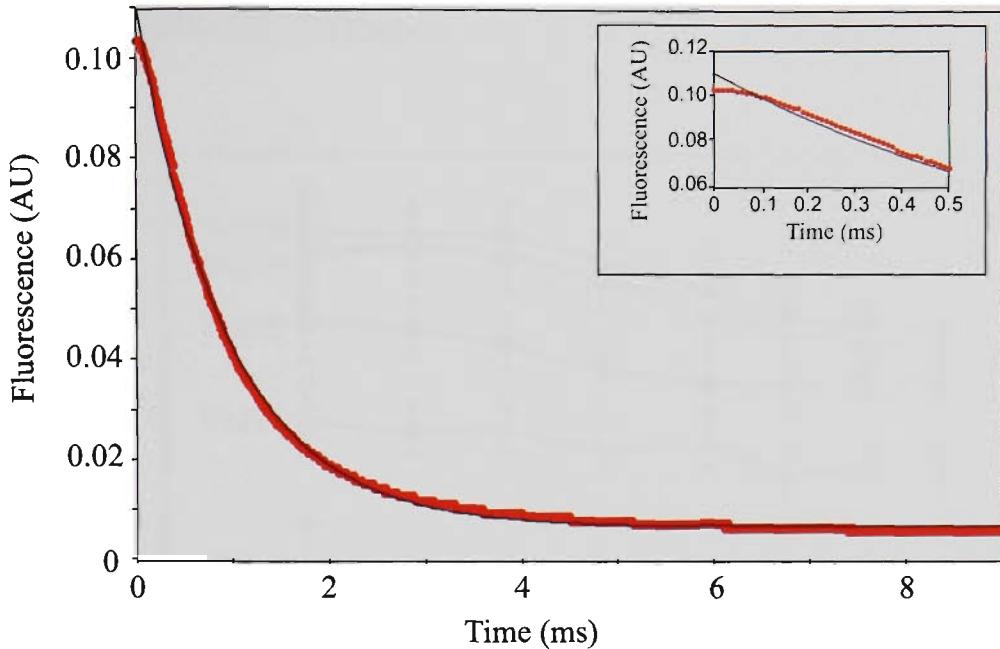


**Figure 5.3:** Plot of the fluorescence decay of YbEr5 as a function of time and fitted with a single exponential using equation 5.8

no fast component present in the decay. The resulting decay is purely fluorescence of ytterbium ions as evident from the single exponential behaviour. For the fitting, the first  $100 \mu\text{s}$  of fluorescence was ignored to improve accuracy of the fit. Equation 5.8 was fitted to data in the fluorescence decay in the range  $10^{-4}$  to  $9 \times 10^{-3}$  s after the pump was turned off to extract the fluorescence lifetime.

### 5.3 Results

The fluorescence lifetimes are shown in figure 5.4 as a function of pump power and in figure 5.5 as a function of erbium concentration. Figure 5.4 shows a general decrease in the fluorescence lifetime with pump power while figure 5.5 shows two distinct trends in the lifetime as a function of concentration. The first (region (i) in figure 5.5) is an increase in lifetime with increasing concentration at concentrations below  $10^{25}$  ions/ $\text{m}^3$ . This is followed by (region (ii) in figure 5.5) a decrease in lifetime at higher concentrations above  $10^{25}$  ions/ $\text{m}^3$ . To ensure that the observed trend was not an experimental anomaly, the experiment was repeated several times. All repeated results showed the same trend in the lifetime with concentration. This non-monotonic trend in the ytterbium excited state lifetime is not in agreement with the

model presented earlier in the chapter.

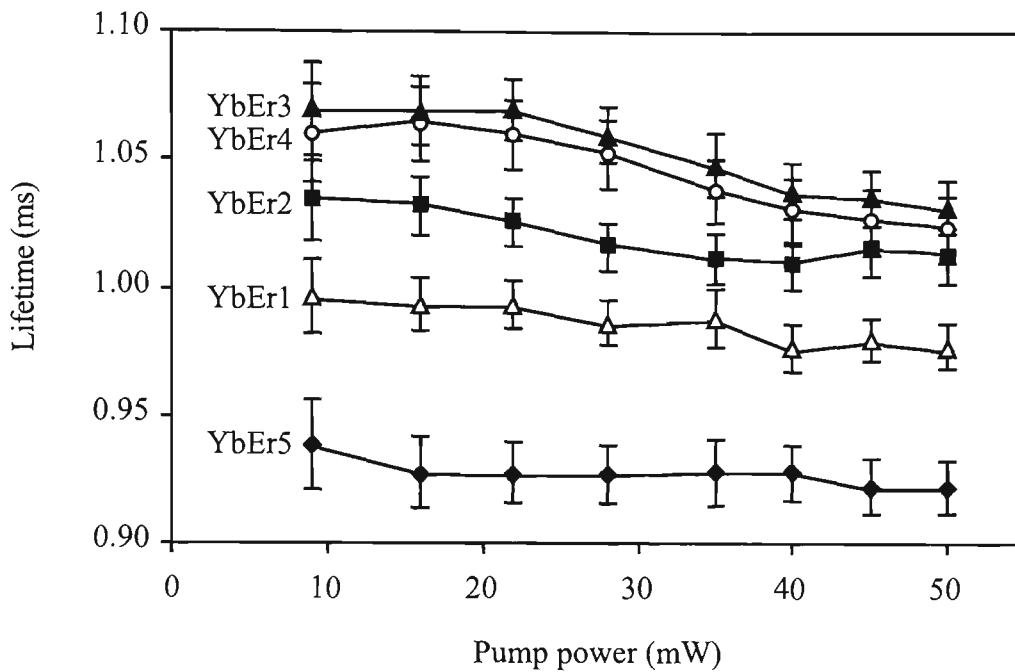


**Figure 5.4:** 1032 nm Fluorescence lifetime of  $\text{Yb}^{3+}$  as a function of 975 nm pump power. The lines joining the data points are for the purpose of aiding the eye only and not intended to be a fit of any type.

While figure 5.5 displays the lifetime as a function of erbium concentration, the increase in ytterbium lifetime is not likely to be attributed to erbium but rather to ytterbium. In order for erbium to increase the fluorescence lifetime of ytterbium, the erbium system must act to transfer energy back to the ytterbium system by repopulating the  $\text{Yb}^{3+} {}^2F_{5/2}$  excited state. This is not expected in here as the phonon rates for the  ${}^4I_{11/2}$  state in erbium resulting in fast decay to the lower lying  ${}^4I_{13/2}$  erbium state and negligible back transfer to ytterbium [117, 138]. Figure 5.5 could also be expressed in terms of ytterbium concentration since the ratio of ytterbium to erbium concentration was unity. Immediately, the conclusion can be drawn that the ytterbium fluorescence lifetime could not be used as a means of determining the concentration of either dopants for the samples used here.

The author speculates that the increase in lifetime at low concentrations may be attributed to self-absorption of ytterbium. Because of the quasi-two level nature of  $\text{Yb}^{3+}$  and spectral overlap between its peak emission and absorption wavelength

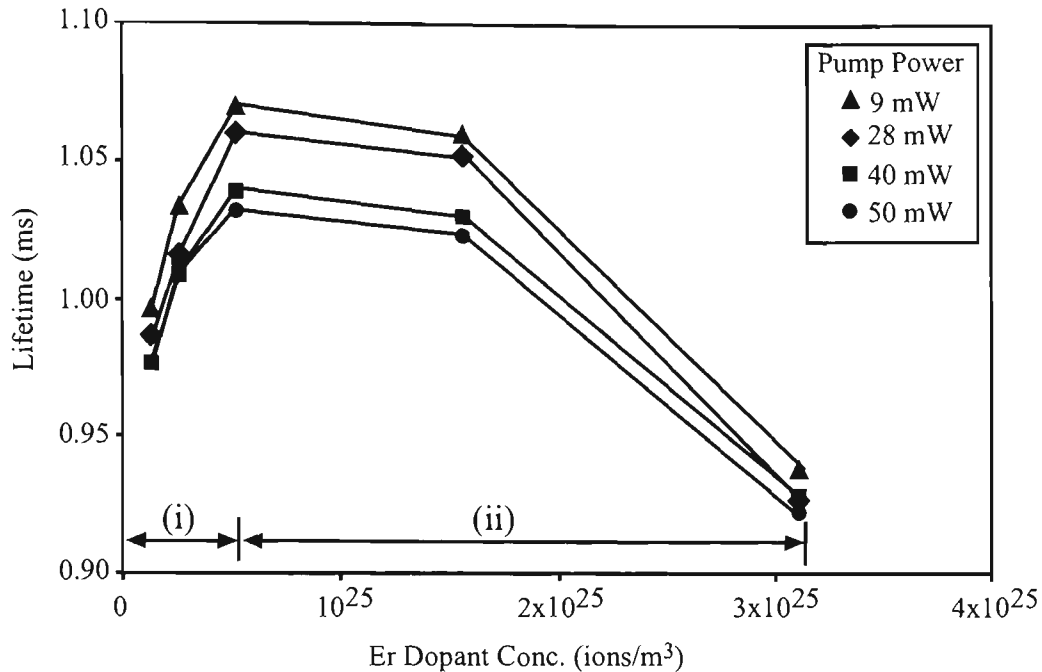


**Figure 5.5:** 1032 nm Fluorescence lifetime of Yb<sup>3+</sup> as a function of Yb/Er dopant concentration.

(around 980 nm), Yb<sup>3+</sup> tends to exhibit self-absorption. This is particularly true in bulk samples where the radiation interaction volume is increased, thereby, increasing the probability of self-absorption. Self-absorption of Yb<sup>3+</sup> fluorescence has been observed in many host materials including Y<sub>2</sub>O<sub>3</sub>, YAG and phosphate glass [142, 102]. However, a search of current literature have not yielded reports of self-absorption of Yb<sup>3+</sup> in silica. The decrease in the lifetime at higher concentrations may be attributed to cooperative energy transfer and concentration quenching.

An explanation of the results is made complicated by the fact that the ytterbium to erbium ratio is made at unity. This does not allow for mechanisms such as concentration quenching due to ytterbium ions to be studied since other mechanisms such as energy transfer also reduces the lifetime. In hindsight, this represents a fundamental error in the selection of appropriate samples for study.

## 5.4 Mechanisms Affecting the Lifetime

There are many processes that affect the fluorescence lifetime to either increase or decrease the lifetime. The observed lifetime is the net result of these processes. They

are discussed in more detail below. In general, the measured decay lifetime can be expressed by equation 2.1 as the sum of the radiative and non-radiative rates:

$$\frac{1}{\tau} = A^{Rad} + A^{non-rad} \quad (5.9)$$

where  $\frac{1}{\tau}$  is the measured fluorescence decay rate. The radiative decay rates include the natural spontaneous emission and self-absorption. The non-radiative decay rates can include such mechanisms as phonon decay, phonon and impurity-assisted concentration quenching, resonant energy transfer and cooperative energy transfer. The following sections discuss these mechanisms in more detail.

### 5.4.1 Spontaneous Emission

The spontaneous emission probability  $A^{Rad}$  gives rise to the natural radiative lifetime of the  ${}^2F_{5/2}$  excited state.  $A^{Rad}$  can be determined by extrapolating fluorescence lifetime measurements as a function of concentration in the limit of zero concentration [60]. Alternatively, it can be calculated from measurements of the absorption spectra and can be given by [102]

$$A^{Rad} = \frac{1}{\tau_{Rad}} = \frac{8\pi cn^2}{\lambda_p^4 N} \frac{g}{g'} \int \sigma_{abs}(\lambda) d\lambda \quad (5.10)$$

where  $c$  is the speed of light,  $n$  is the refractive index at the mean absorption wavelength,  $\lambda_p$  is the peak absorption wavelength,  $N$  is the concentration of Yb<sup>3+</sup> ions,  $g$  and  $g'$  are the degeneracies of the  ${}^2F_{7/2}$  and  ${}^2F_{5/2}$  energy levels respectively and  $\sigma_{abs}$  is the absorption coefficient. Extrapolation of the lifetimes in figure in figure 5.5 yields a natural radiative lifetime of 0.93 ms.

### 5.4.2 Self-absorption

Self-absorption, also called self-trapping or radiation-trapping, is a process where a spontaneously emitted photon is re-absorbed by an ion in the ground state instead of escaping the host medium. This leads to repopulation of the excited state another ion. In turn this second ion re-emits the photon after some time, leading to an ef-

fective lifetime increase. This process can occur many times before the final photon escapes the system. The result is an apparent ‘trapping’ or delay in the effective rate of spontaneous emission. This photon can only be absorbed by an ion whose excitation transition is resonant with the energy of the photon. This normally means that the absorbing ion is of the same type as the emitting ion, hence the term ‘self-absorption’. The absorption coefficient of  $\text{Yb}^{3+}$  is strong and broad which increases the spectral overlap between absorption and emission and increases the likelihood of self-absorption. A schematic representation of self-absorption is shown in figure 5.6.

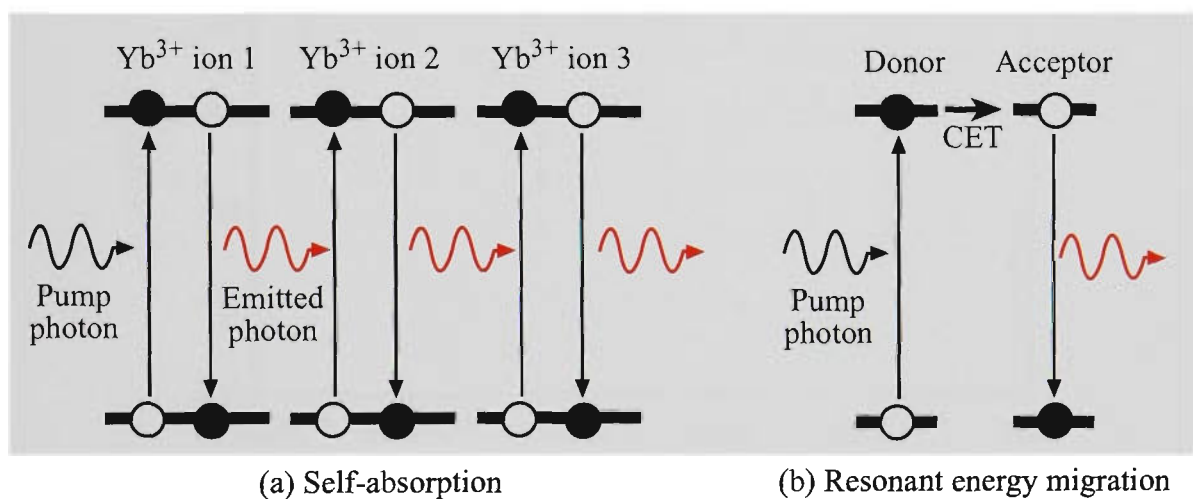


**Figure 5.6:** Schematic diagram of (a) self-absorption and (b) resonant energy migration. The open dots represent ions before absorption and the solid dots represent ions after emission.

Self-trapping can be verified by application of a simple calculation.

$$\omega = \frac{1}{t_e} - \frac{1}{t_0} \quad (5.11)$$

where  $t_e$  is the measured lifetime,  $t_0$  is the intrinsic radiative lifetime (lifetime in the limit of zero concentration) and  $\omega$  is the additional contribution to the lifetime by self-absorption.  $\omega$  can be plotted against the inverse of the square of the average distance ( $R$ ) between adjacent  $\text{Yb}^{3+}$  ions [113]. The  $\text{Yb}^{3+}$  concentration is proportional to  $\frac{1}{R^2}$ , thus  $\omega$  is proportional to  $\text{Yb}^{3+}$  concentration. A linear decrease in  $\omega$  will indicate self-trapping whereas a linear increase will indicate non-radiative quenching

[129]. A non-linear variation would indicate multi-ion, or concentration-dependent processes such as CET. Figure 5.7 shows  $\omega$  plotted against  $\frac{1}{R^2}$  for the concentrations in the range where there is an increase in lifetime. There are only three concentrations in this range, thus it cannot be concluded whether the relationship between  $\omega$  and concentration in figure 5.7 is linear or not. More data points would be required for more conclusive evidence of self-trapping.

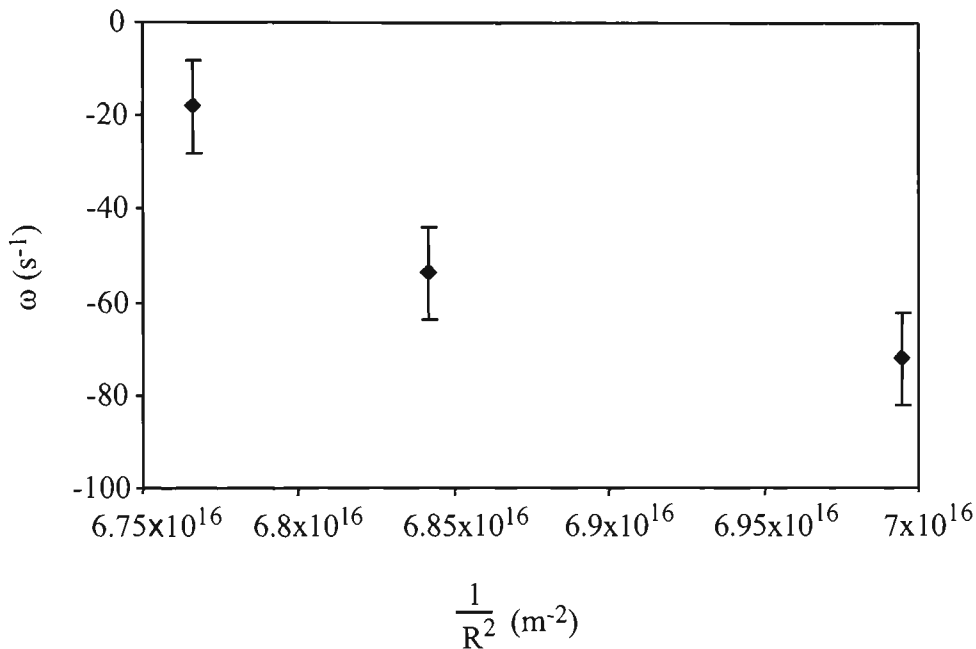


**Figure 5.7:** Plot of  $\omega$  as a function of 1 over the square of the average distance between Yb<sup>3+</sup> ions.

### 5.4.3 Resonant Energy Migration

Resonant energy migration (REM) is the non-radiative equivalent to self-absorption and occurs when there is CET between an excited ion and a ground state ion as shown in figure 5.6. In REM, an excited ion will transfer its energy non-radiatively to a neighbouring ion that is close enough to permit this CET. REM occurs at high concentrations where individual ions are closely spaced to each other and in clusters. The effect of self-absorption and REM is an increase in the effective macroscopic lifetime.

#### 5.4.4 Phonon Decay

The ground state manifolds and excited state manifolds are separated by a large energy gap ( $\approx 10200 \text{ cm}^{-1}$ ), much larger than the phonon energy of silica. This would require at least 10 phonons to bridge the energy gap. Thus it may be expected that there is no phonon decay within the  $\text{Yb}^{3+}$  system or phonon decay is negligible. The radiative efficiency from singly-doped  $\text{Yb}^{3+}$  systems is near unity.

#### 5.4.5 Concentration Quenching

Because of ytterbium's simple two-level energy structure, there is no excited state absorption, cooperative up-conversion or cross-relaxation within the  $\text{Yb}^{3+}$  system itself to quench the  $^2F_{5/2}$  excited state. However, measurements of the fluorescence lifetimes have varied from 1.3 to 2.7 ms for silicate glass with different host compositions [143] suggesting concentration quenching due to impurities in the host [142, 144]. These impurities may also lead to multi-phonon quenching of the  $\text{Yb}^{3+}$  fluorescence. Burshtein *et al* has found that the rate of impurity multi-phonon quenching increases with  $\text{Yb}^{3+}$  concentration due to local site deformation caused by the  $\text{Yb}^{3+}$  ions [129]. The increase in  $\text{Yb}^{3+}$  concentration causes an increase in the phonon-band density which enhances the non-radiative decay probability. In addition to quenching by impurities such as germanium, the fluorescence lifetime may also be quenched by OH ions [102]. In the case of a codoped system like the preforms used here, the presence of both ytterbium and erbium would increase the probability of multi-phonon quenching. The quenching caused by individual dopants could not be determined with the samples used in this work.

#### 5.4.6 Cooperative Luminescence

An interesting phenomenon that may occur in  $\text{Yb}^{3+}$  involves virtual states resulting in emissions of radiation in the visible [145, 146, 147]. This occurs when two excited ions simultaneously relax to the ground state and emit a single photon of twice the energy and half the wavelength of the transition. The observation of the virtual photon gives the impression that the photon was emitted from a virtual state which has

resulted from cooperative up-conversion but that does not physically exist. No such virtual transitions were observed in these samples. Although visible fluorescence was observed, its wavelength was centered around 540 nm corresponding to the radiative decay from the  $^4S_{3/2}$  state in  $\text{Er}^{3+}$ . Any visible fluorescence due to virtual states would have a wavelength centered at half the peak emission wavelength of  $\text{Yb}^{3+}$  (i.e., around 490 nm). This was not observed, thus the only cooperative energy transfer mechanism is the transfer of energy from  $\text{Yb}^{3+}$  to  $\text{Er}^{3+}$  ions.

## 5.5 Limitations Of This Work

While various authors have treated each of the processes described above individually, a collective interpretation has not been reported, certainly not for glass samples doped with multiple rare earth dopants. This is primary due to the fact that some processes can not be experimentally discriminated from others, such as concentration quenching due to multi-phonon decay and cooperative energy transfer between rare earth ions. In addition, some processes compete with each other and resultant measured rates may hide the weaker processes. This presents a problem for modelling the lifetime and processes such as self-absorption are not typically included in rate equations. Because the codoped samples used here had equal amounts of erbium to ytterbium, separating their effects is difficult. What is required is more samples in which one dopant concentration was made constant while the codopant varied with the samples and vice versa. This way, some of the effects such as concentration quenching could be studied in more detail and a better understanding of the concentration effects could be obtained.

## 5.6 Conclusion

In this chapter the 1032 nm fluorescence lifetime from  $\text{Yb}^{3+}$  ions in Yb:Er-doped fibre preforms were studied. The lifetime of the  $\text{Yb}^{3+}$  fluorescence was found to be not monotonic, increasing in the lifetime at low concentrations before decreasing at higher concentrations. It is suspected that the lifetime increase in the low concen-

tration regime is attributed to self-absorption where as the decrease in the lifetime at higher concentrations is more likely to be due to cooperative energy transfer from  $\text{Yb}^{3+}$  to  $\text{Er}^{3+}$  ions. This increase in lifetime, if caused by self-absorption, is the first such observation for ytterbium doped in a silica host.

The non-monotonic dependence of the lifetime on concentration prevents the use of the lifetime from this fluorescence to determine concentration, since a single lifetime value may correspond to two different dopant levels. It is concluded that the lifetime of the 1032 nm fluorescence can not be used for determining concentrations. Further work needs to be done by using samples where the concentration of  $\text{Yb}^{3+}$  is fixed while the concentration of  $\text{Er}^{3+}$  varies and vice versa.

## Chapter 6

# Praseodymium-doped glass

Praseodymium, the third element within the rare earth group, has attracted interest in optical communications as well as other areas, such as sensing. Praseodymium-doped fibre amplifiers operating in the 1.3  $\mu\text{m}$  telecommunication window have been demonstrated [148] as well as amplification at the 632.8 nm HeNe laser wavelength [149]. Lasing action has been observed in  $\text{Pr}^{3+}$ -doped fluoride glass fibres with wavelengths in the range 490 to 910 nm [12, 150, 151].  $\text{Pr}^{3+}$  has also been shown to be a useful probe for temperature sensing in the range  $-45^\circ\text{C}$  to  $255^\circ\text{C}$  [96]. The possibility of simultaneous temperature and strain sensors in praseodymium-doped fibres have also been proposed [152]. The possibility of producing light in the blue, green and red has identified praseodymium as a possible candidate for colour laser displays [153, 154, 155].

Imaging of the concentration profile of praseodymium has already been performed using the fluorescence lifetime technique. This was done by Petreski *et al* who found that the decay rate of the 635 nm fluorescence in  $\text{Pr}^{3+}$ :ZBLAN glass was linearly proportional to the  $\text{Pr}^{3+}$  concentration [60]. This provided a convenient method for imaging the concentration profile in  $\text{Pr}^{3+}$ :ZBLAN fibre [59]. However, it has been shown that the lifetime from this fluorescence has a strong dependence on temperature with the lifetime increasing with temperature [156]. The sensitivity of this temperature-dependence also varies for different dopant concentrations. In this chapter, the 635 nm fluorescence lifetime is revisited and the use of this lifetime for concentration imaging is reassessed. The results presented in this chapter have been published by the author in *Optics Communications* in 2000 [90].

## 6.1 Modelling

The energy levels of interest in this work are the  ${}^3P_0$ ,  ${}^3P_1$  and  ${}^1I_6$  excited states in  $\text{Pr}^{3+}$  doped ZBLAN glass. The  ${}^3P_1$  and  ${}^1I_6$  levels are sufficiently close to each other that they can be considered as a single energy level. In this work,  ${}^3P_1$  will be used to denote both energy levels. The energy separation of the  ${}^3P_0$  and  ${}^3P_1$  states is sufficiently small ( $\Delta E = 616 \text{ cm}^{-1}$ ) such that the levels are thermally coupled and their relative populations may be determined by a Boltzmann distribution. There are many possible transitions, both radiative and non-radiative, that may originate from the  ${}^3P_0$  energy level [98]. Radiative transitions from these excited states to the  ${}^3F_2$  lower excited state give rise to strong fluorescence centered around 635 nm that is easily detected. An energy level diagram of  $\text{Pr}^{3+}$  is shown in figure 2.5 on page 31.

The fluorescence lifetime arising from the  ${}^3P_0$  energy level has been modelled in various ways by several different authors. Petreski *et al* modelled the concentration dependence of this 635 nm fluorescence lifetime based on rate equations that included cross-relaxation between two ions in the  ${}^3P_0$  excited state [60]. The temperature-dependence of the lifetime can be seen using a thermodynamical approach [157]. In this work, the two methods are combined. The thermodynamic model is adopted as a starting point to determine the temperature dependence in the fluorescence lifetime at different dopant concentrations. This model shows that for two thermally coupled excited energy levels separated by energy,  $\Delta E$ , the relaxation rate has a temperature dependence that is given by [157]:

$$\Gamma = \frac{\Gamma_{10} + \Gamma_{20} \frac{g_2}{g_1} \exp\left(-\frac{\Delta E}{k_B T}\right)}{1 + \frac{g_2}{g_1} \exp\left(-\frac{\Delta E}{k_B T}\right)} \quad (6.1)$$

where  $T$  is the absolute temperature,  $\Gamma_{10}$  and  $\Gamma_{20}$  are the decay rates of the lower ( ${}^3P_0$ ) and upper ( ${}^3P_1$ ) excited states to the terminating level at  $T = 0$  respectively.  $g_1$  and  $g_2$  are the lower and upper degeneracies with the ratio  $g_2/g_1$  being 16 for these particular levels, and  $k_B$  is the Boltzmann constant.

## 6.2 Experimental Arrangement

Fluorescence decay from the  ${}^3P_0$  excited state was measured using the experimental arrangement shown in figure 6.1. The argon ion pump laser operated at 476.5 nm with a nominal output power of 450 mW. The pump beam was modulated by a mechanical chopper, which was centered at the common focus of two  $\times 20$  microscope objectives to minimise the rise and fall time of the modulation. The rise and fall time of the pulse modulation was measured to be  $4 \mu\text{s}$  when modulated at 2 kHz. The 635 nm fluorescence from the  ${}^3P_0 \rightarrow {}^3F_2$  transition was filtered using a narrow band filter with a FWHM of 11 nm centered at 633 nm and collected using a silicon PIN photodiode. The glass samples were housed in an aluminium holder which sat on a heat reservoir. The reservoir was heated using a hotplate and cooled using liquid nitrogen.

Fluorescence data were collected using a Tektronix TDS-320 digital oscilloscope and averaged over 256 captures. The captured fluorescence decay curves were fitted with an exponential function to determine the fluorescence lifetime.

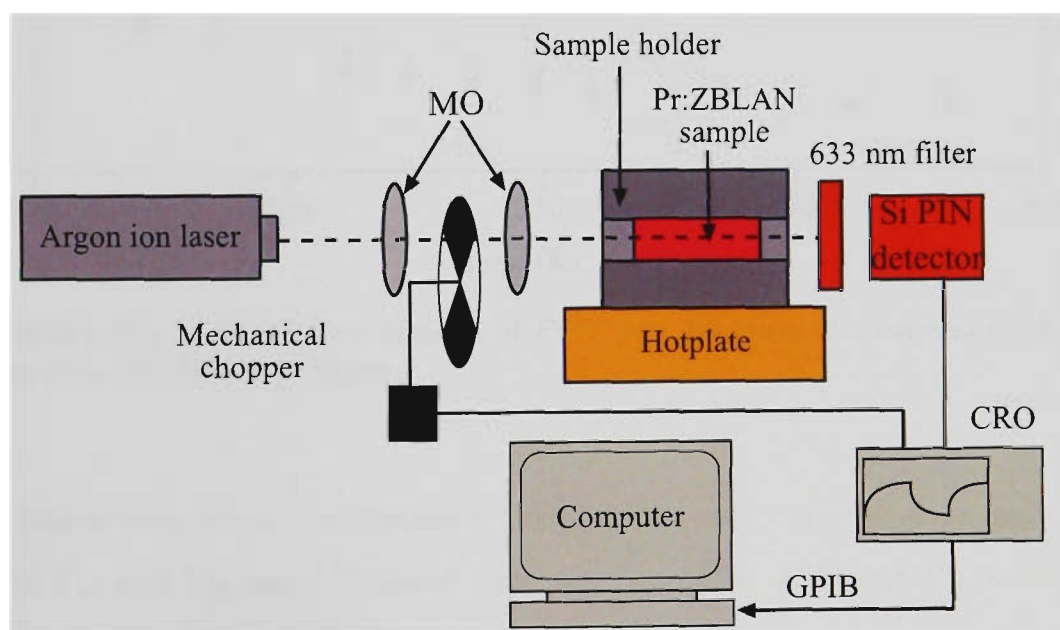


**Figure 6.1:** Experimental arrangement for measuring fluorescence lifetimes of  $\text{Pr}^{3+}$ ZBLAN glass. Pump light from an argon ion laser was focussed then expanded using two  $\times 20$  microscope objectives (MO). The pump light was modulated using a mechanical chopper. The fluorescence was filtered using a 633 notch filter and collected using a silicon PIN detector.

### 6.3 Results

The fluorescence lifetimes ( $1/\Gamma$ ) of the  $^3P_0$  state were measured over the temperature range 193 to 513 K, for four dopant concentrations and are plotted in figure 6.2. The results show that for low dopant concentrations, the lifetime increases with temperature. This rise in lifetime with temperature becomes smaller as the dopant concentration increases. At the highest concentration (Pr4), the lifetime has decreased with temperature.

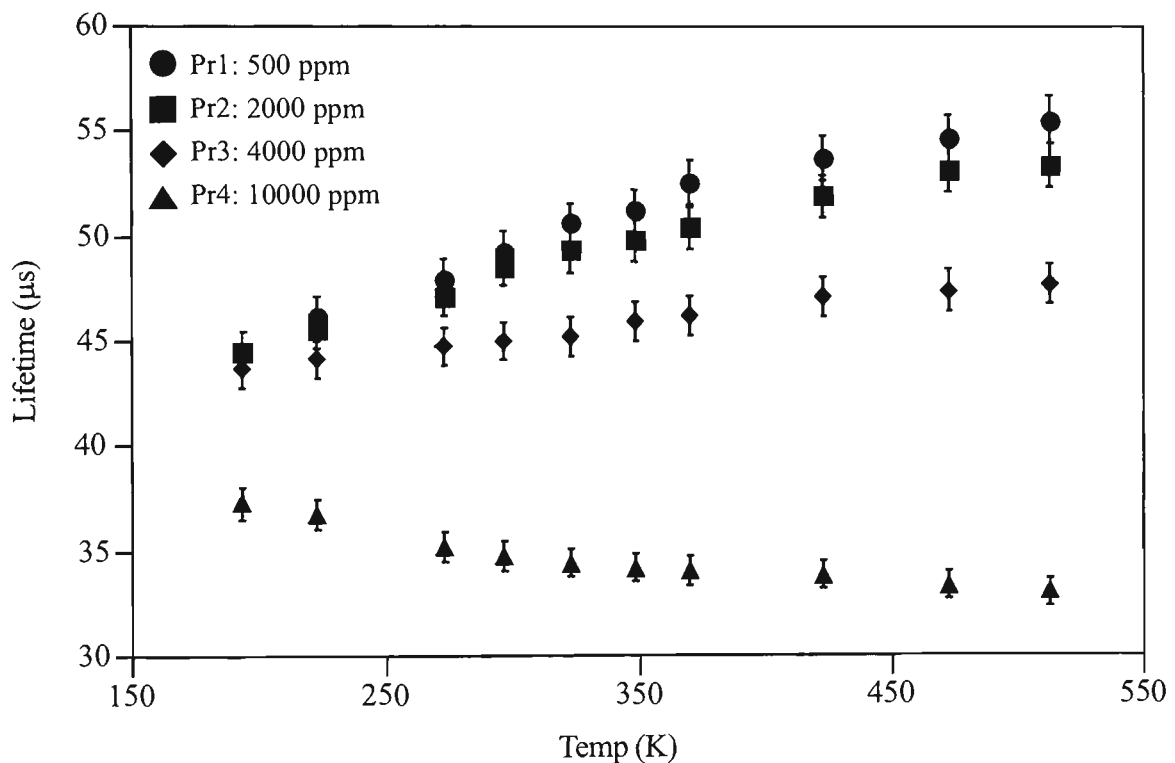


**Figure 6.2:** Fluorescence lifetime of  $\text{Pr}^{3+}$  as a function of temperature for the four Pr:ZBLAN samples.

The lifetimes were fitted to equation 6.1 for each dopant concentration and the parameters  $\Gamma_{10}$  and  $\Gamma_{20}$  were obtained from the fits. The values for  $\Gamma_{10}$  and  $\Gamma_{20}$  are shown in figure 6.3 as a function of concentration. Quadratic fits were applied to the parameters and is also shown in the figure.

The results show that for  $\Gamma_{10}$  there is a small variation with concentration in com-

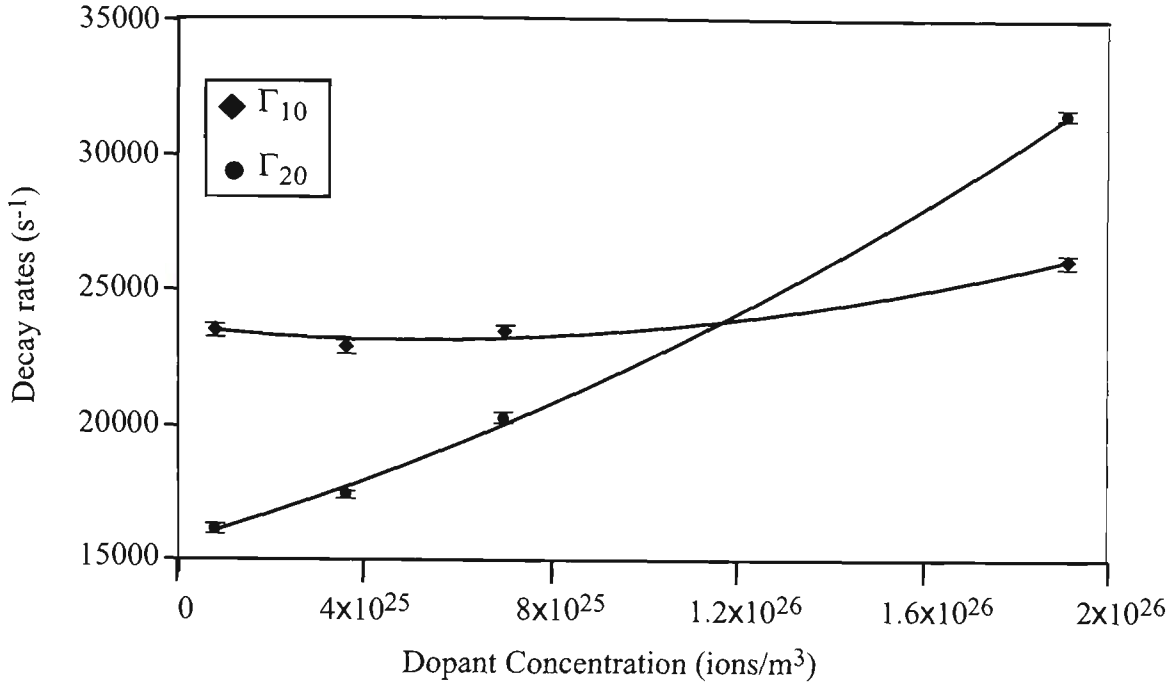


**Figure 6.3:** The decay rates  $\Gamma_{10}$  and  $\Gamma_{20}$  as a function of dopant concentration. The solid lines are least squares fits of a quadratic function  $\alpha + \beta\rho + \gamma\rho^2$ .

parison to the  $\Gamma_{20}$ .  $\Gamma_{20}$  seems to fit well with the empirically fitted quadratic. This allows the concentration dependence to be included in the model in a simple manner by replacing  $\Gamma_{20}$  in equation 6.1 with a quadratic in concentration ( $\alpha + \beta\rho + \gamma\rho^2$ ). In addition to this modification, the finite spectral widths of the  $^3P_0$  and  $^3P_1$  energy levels were taken into account by integrating the separation of the participating levels over their average spectral widths,  $\delta e$ . This was necessary as the spectral widths of the excited states are comparable with the energy separation between them. The modified expression for the decay rate then becomes

$$\Gamma = \frac{1}{\delta e} \int_{E-\delta e}^{E+\delta e} \frac{\Gamma_{10} + (\alpha + \beta\rho + \gamma\rho^2) \frac{g_2}{g_1} \exp\left(-\frac{x}{k_B T}\right)}{1 + \frac{g_2}{g_1} \exp\left(-\frac{x}{k_B T}\right)} dx \quad (6.2)$$

Equation 6.2 can be simultaneously fitted to all data points for all dopant concentrations over the specified temperature range. The result of the fit is shown in figure 6.4 with the fluorescence lifetime ( $1/\Gamma$ ) as a function of temperature, and replotted in figure 6.5 as a function of dopant concentration. The fitting yields a single set of values for the free parameters defined in equation 6.2. The parameters are summarised in table 6.1. The spectral widths of the  $^3P_1$  and  $^3P_0$  levels were approximately equal

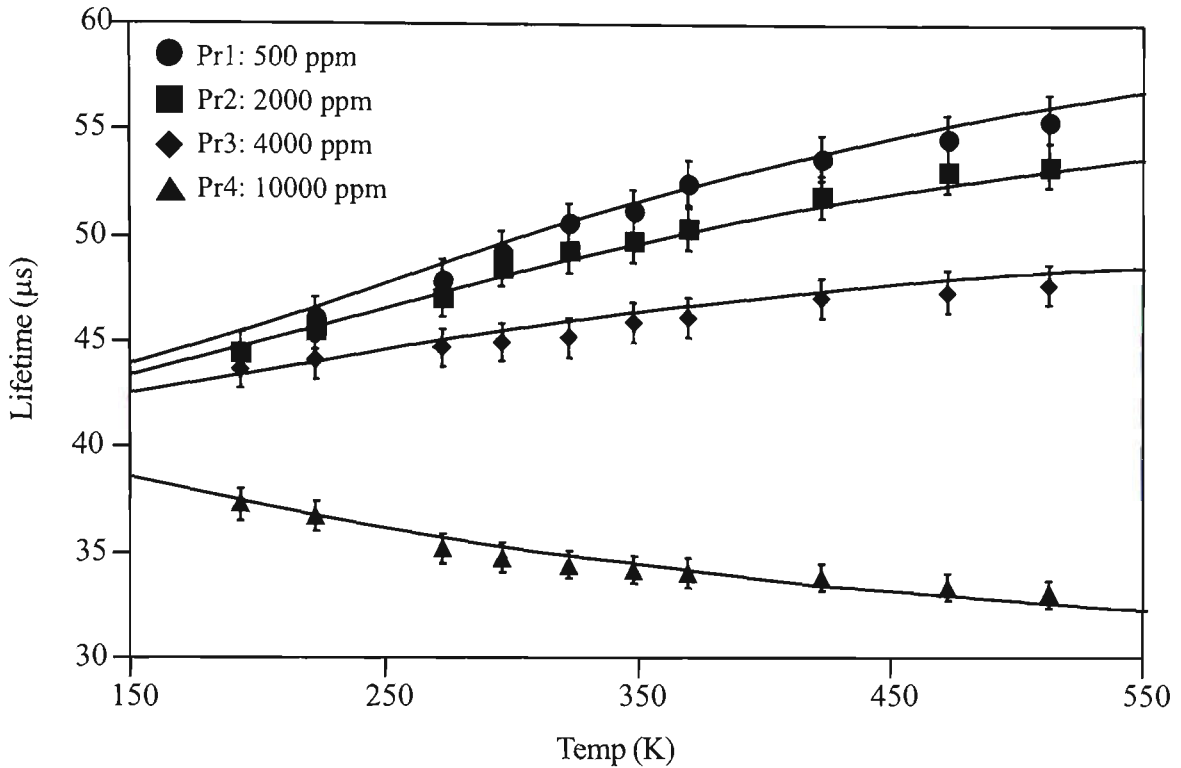


**Figure 6.4:** The fluorescence lifetime of the 635 nm emission from the  $^3P_0$  excited state as a function of temperature for the four dopant concentrations fitted using equation 6.2.

and calculated to be  $471 \pm 5 \text{ cm}^{-1}$  by analysis of absorption spectra obtained from reference [158]. This value agrees well with the fitted value obtained for  $\delta e$  from the fit.

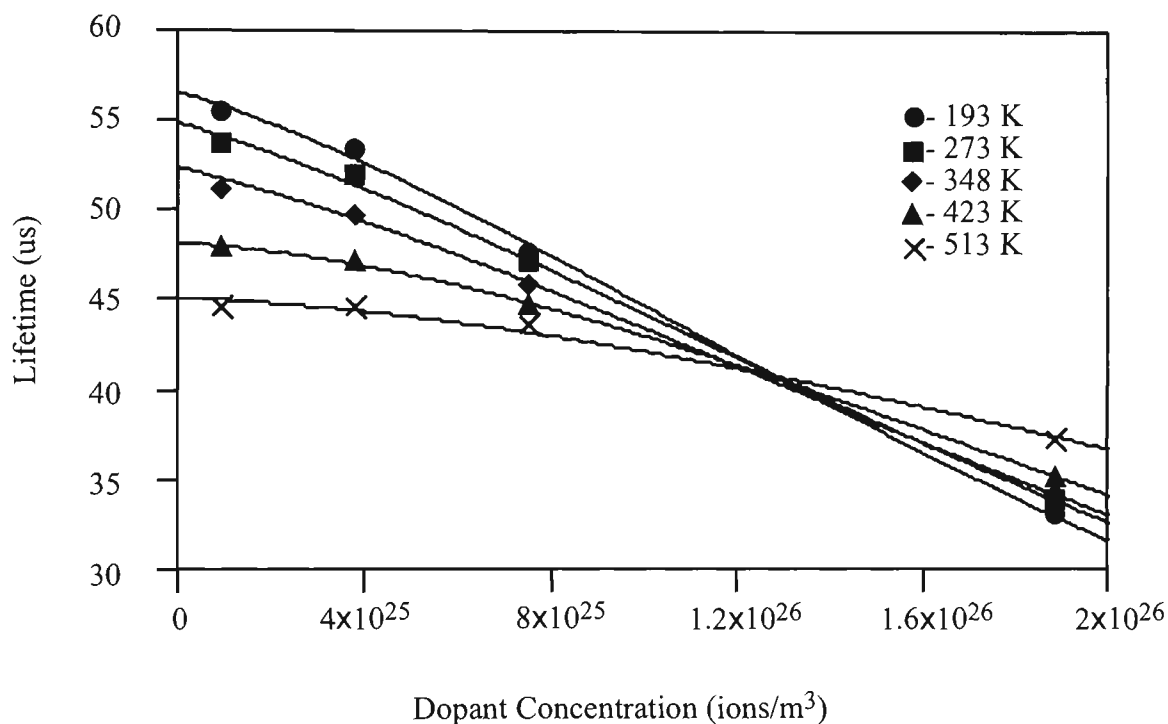
## 6.4 Temperature Dependence

Figure 6.4 shows that the fluorescence lifetime of the three lowest concentrations increased with increasing temperature, whereas the fluorescence lifetime of the highest concentration decreased with temperature. This change in trend suggests a critical concentration at which the fluorescence lifetime is independent of temperature. This can be seen in figure 6.5 where the lines of constant temperature cross at approximately  $(1.30 \pm 0.04) \times 10^{26} \text{ ions/m}^3$ . The lifetime increases with temperature at concentrations below  $1.30 \times 10^{26} \text{ ions/m}^3$  and decreases with temperature at con-

Parameters	Fitted Values
$\Gamma_{10}$	$24500 \text{ s}^{-1} (\pm 0.5\%)$
$\alpha$	$14800 \text{ s}^{-1} (\pm 1.3)\%$
$\beta$	$3.5 \times 10^{-23} \text{ m}^3/\text{ion} \cdot \text{s} (\pm 13\%)$
$\gamma$	$3.7 \times 10^{-49} \text{ m}^6/\text{ion}^2 \dots (\pm 6\%)$
$\delta e$	$470 \text{ cm}^{-1} (\pm 5.4\%)$

**Table 6.1:** Fitted values for the parameters defined in equation 6.2 for modelling the  $\text{Pr}^{3+}$  fluorescence lifetime.

centrations above this level.



**Figure 6.5:** The fluorescence lifetime of the 633 nm emission from the  $^3P_0$  excited state as a function of nominal dopant concentration for selected temperatures.

The sensitivity of the lifetime to temperature is greater at low temperatures but reduces as the temperature increases. This can be seen in figure 6.4 as the lifetime curves flatten out towards higher temperatures. This is better illustrated in figure 6.6 showing the sensitivity of the lifetime to temperature. In figure 6.6 the sensitivity is expressed as a fractional change in lifetime per unit temperature.

$$S = \frac{1}{\tau} \frac{d\tau}{dT} \quad (6.3)$$

The temperature sensitivity is less than 0.1 % but is comparable to the temperature sensitivity to other rare earths and could be suited for temperature sensing [159, 160].

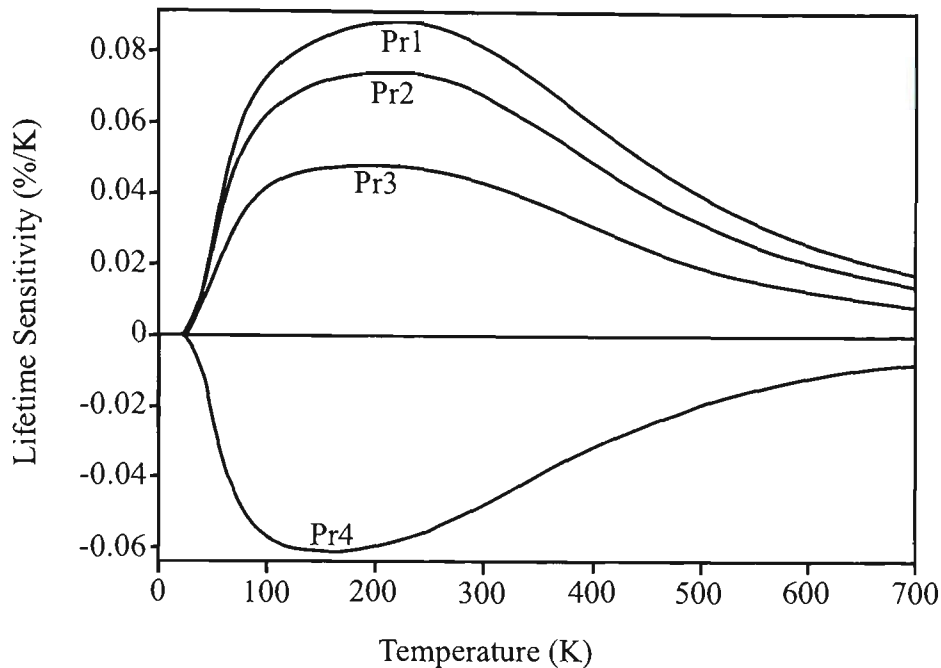


**Figure 6.6:** Plot of the sensitivity of the fluorescence lifetimes with respect to temperature.

## 6.5 Concentration-Dependent Processes

The physical origin of the parameters  $\alpha$ ,  $\beta$  and  $\gamma$  can be elucidated by considering a rate equation analysis which includes energy transfer between neighbouring ions. From the empirical evidence shown in figure 6.3, the concentration-dependent effects were modelled as originating from the  $^3P_1$  excited state. The concentration-dependent effects from the  $^3P_0$  state were considered negligible, as evident by the low error and the small change in  $\Gamma_{10}$ , and therefore ignored. This differs somewhat from Petreski *et al* [60] in their analysis of the same transition. Petreski *et al* modelled the fluorescence lifetime solely on the  $^3P_0$  state and ignored the  $^3P_1$  state. Consequently, state specific concentration-dependent effects were not considered.

Petreski explained the concentration effects by use of rate equations and by con-

considering all possible decay processes from the  $^3P_0$  state. The same approach can be taken here by considering all possible decay processes from the  $^3P_1$  state. The total decay rate is the sum of all possible decay processes (radiative and non-radiative). Figure 6.7 shows some possible cross-relaxation processes that may originate from the  $^3P_1$  state. Processes (a), (b) and (c) involve energy transfer between two ions. These three processes are indistinguishable by the detection technique used here because the originating energy levels are the same for all three processes. For the purpose of modelling, they can be characterised by a single cross-relaxation coefficient  $\beta$ . Processes (d) and (e) involve energy transfer between a single ion from the  $^3P_1$  level and two ions from the ground level. These three ion processes can be characterised by a single coefficient  $\gamma$ .

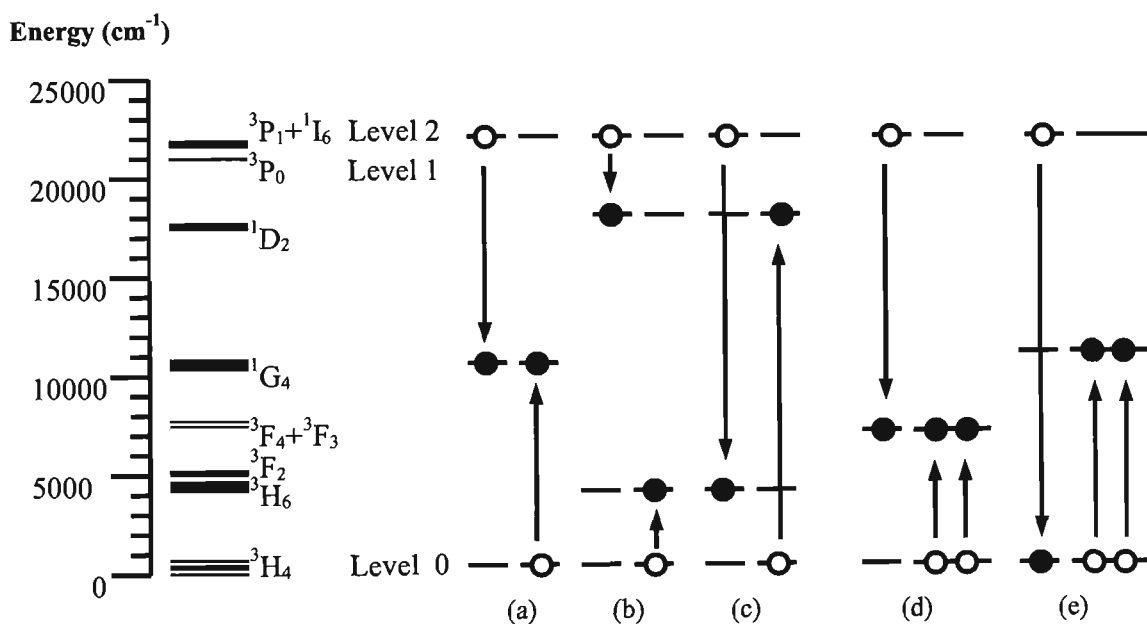


**Figure 6.7:** Simplified schematic energy diagram of Pr<sup>3+</sup> doped ZBLAN glass showing some possible cross-relaxation processes originating from the  $^3P_1$  and the ground state. Processes (a), (b) and (c) involve two ions. Processes (d) and (e) involve three ions. The clear and solid dots represent ions before and after energy transfer respectively.

The time evolution of the population of the  $^3P_1$  state immediately after excitation

can then be written as

$$\frac{dn_2}{dt} = \omega_{12}n_1 - \omega_{21}n_2 - \alpha n_2 - \beta\rho n_2 n_0 - \gamma\rho^2 n_2 n_0^2 \quad (6.4)$$

where  $\omega_{12}$  and  $\omega_{21}$  are transfer rates between the  ${}^3P_0$  and  ${}^3P_1$  states,  $\alpha$  is the decay rate in the limit of zero concentration,  $\rho$  is the dopant concentration and  $n_0$ ,  $n_1$  and  $n_2$  are the normalised populations of the ground state, the  ${}^3P_0$  state and  ${}^3P_1$  state respectively. Because the  ${}^3P_0$  and  ${}^3P_1$  states are thermally coupled, in equilibrium  $\omega_{12}n_1 = \omega_{21}n_2$  [26] and equation 6.4 is reduced to

$$\frac{dn_2}{dt} = -n_2(\alpha + \beta\rho n_0 + \gamma\rho^2 n_0^2) \quad (6.5)$$

If the pump rate is kept relatively low, there is negligible depletion of the ground state, and  $n_0$  can be approximated to unity. Equally, the excited state probability,  $n_2$ , will also be small, justifying the neglect of terms involving powers of  $n_2$  in equation 6.4. Under this condition, equation 6.5 will have a solution of the form

$$n_2(t) = n_2(0)\exp(-\Gamma_2 t) \quad (6.6)$$

where

$$\Gamma_2 = \alpha + \beta\rho + \gamma\rho^2 \quad (6.7)$$

Here,  $\Gamma_2$  is the total decay rate from level  ${}^3P_1$ . This expression is the same in form as the empirical substitution for  $\Gamma_{20}$  in equation 6.2. Thus the substitution  $(\alpha + \beta\rho + \gamma\rho^2)$  in equation 6.2 describes a physical process and  $\beta$  and  $\gamma$  may be defined as the energy transfer coefficients for the cross-relaxation processes that are occurring. Indeed, the value for  $\beta$  obtained in this work compares well with the value obtained by Petreski *et al* for the same parameter, even though the  ${}^3P_1$  state was ignored in Petreski's model [60]. This is because the  ${}^3P_1$  and  ${}^3P_0$  states are thermally coupled and their fluorescence decay rates are the same in thermal equilibrium regardless of whether cross-relaxation originated from the  ${}^3P_1$  state or the  ${}^3P_0$  state.

## 6.6 Conclusion

In this section, a model has been developed that explains the observed dopant concentration and temperature dependence of the fluorescence lifetime of the  $^3P_0$  and  $^3P_1$  excited state in  $\text{Pr}^{3+}:\text{ZBLAN}$  glass. This strong temperature dependence arises from the close proximity of these two states and, consequently, the thermal coupling between them. The concentration dependence arises from cross-relaxation processes involving excited ions in the  $^3P_1$  state and not from the  $^3P_0$  state as suggested by other authors [60]. However, these processes affect the  $^3P_0$  state because of the thermal coupling between the two levels. This may have consequences for the optimisation of applications that utilises the  $^3P_0$  excited state such as amplification at the HeNe wavelength.

The model here also predicts a concentration in which the fluorescence lifetime is independent of temperature. This finding has consequences for fluorescence lifetime-based sensing applications in which  $\text{Pr}^{3+}:\text{ZBLAN}$  is used as the sensor probe. Temperature sensors should avoid dopant levels near the critical concentration because of the reduced temperature sensitivity. On the other hand, strain sensors should be doped near the critical concentration to reduce temperature effects because the fluorescence lifetime is independently affected by temperature and strain [161].

In using the fluorescence lifetime of the  $^3P_0$  and  $^3P_1$  excited states as a means of determining dopant concentration and concentration imaging, fluorescence from the  $^3P_1$  state is preferred as this level has a greater concentration dependence. The  $^3P_0$  and  $^3P_1$  levels are separated by  $616\text{ cm}^{-1}$ , or approximately 38 nm. The fluorescence peaks from the two levels can thus be sufficiently separated by choice of appropriate narrow-band filters. The decay rate for  $^3P_1$  then has a simple quadratic dependence with dopant concentration.

## Chapter 7

# Conclusion

Knowledge of dopant concentration and dopant distribution is important in modelling and predicting the performance and behaviour of photonic devices made from rare earth-doped fibres and waveguides. A simple method capable of determining such concentration information for different sample types, in particular fibres, is needed. In this thesis, the possibility of using the fluorescence lifetimes of the rare earth dopants was investigated as a means for determining their concentrations in various sample types. This work investigated the fluorescence lifetime properties of  $\text{Er}^{3+}$ -doped fibres,  $\text{Yb}^{3+}:\text{Er}^{3+}$ -codoped fibre preforms and  $\text{Pr}^{3+}$ -doped bulk glass to determine the suitability of their fluorescence lifetimes for determining dopant concentration.

### 7.1 Summary of Findings

#### 7.1.1 Fluorescence lifetime in Er-doped fibres

In chapter 4 the fluorescence lifetimes of the 1535 nm emission and the 540 nm emission in  $\text{Er}^{3+}$ -doped silica fibres were studied. A consolidated model was developed for the 1535 nm fluorescence lifetime based on rate equations that governed the time-dependent population of the  $^4I_{13/2}$  excited state. The model showed that the fluorescence lifetime has a logarithmic dependence on the dopant concentration as well as pump power. This logarithmic dependence reveals two very distinct regions in the behaviour of the fluorescence lifetime with concentration. At concentrations below  $5 \times 10^{25}$  ions/ $\text{m}^3$  the lifetime was insensitive to concentration. Also below this dopant level the fluorescence lifetime did not seem to be affected by pump power. However, above  $5 \times 10^{25}$  ions/ $\text{m}^3$ , the fluorescence lifetime decreased as a function

of both dopant concentration and pump power. This decrease has been attributed to cooperative energy transfer between neighboring ions in the  $^4I_{13/2}$  excited state. The up-conversion coefficient that describes this energy transfer process appeared to decrease with concentration.

Investigation of the 540 nm fluorescence indicate that its lifetime appears not to be concentration-dependent. A spectroscopic study of the energy levels and transitions in  $\text{Er}^{3+}$ -doped silica glass showed no appreciable cooperative energy transfer effects that may alter the lifetime of the 540 nm fluorescence. Measurement of the 540 nm lifetime, when pumped at both 795 nm and 488 nm, did not show any correlation with erbium concentration.

### 7.1.2 Fluorescence lifetime in Yb:Er-codoped fibre preforms

In chapter 5 the 1032 nm fluorescence lifetime from the  $^2F_{5/2}$  excited state of  $\text{Yb}^{3+}$  in  $\text{Yb}^{3+}:\text{Er}^{3+}$ -codoped fibre preforms was studied. The results found that this emission lifetime exhibited non-monotonic behaviour with concentration firstly increasing with increasing concentration at concentrations below  $10^{25}$  ions/ $\text{m}^3$  before decreasing at higher concentrations. The increase in lifetime at low concentrations has been attributed to self-absorption of the fluorescence emission whilst the decrease in lifetime is attributed to cooperative energy transfer from  $\text{Yb}^{3+}$  to  $\text{Er}^{3+}$ .

A model was proposed to describe the observed fluorescence lifetime. However, owing to the ratio of the  $\text{Yb}^{3+}$  to  $\text{Er}^{3+}$  ions being the same for all the samples the model could not predict which of the dopant species are responsible for the decay processes identified. It could not be established whether the observed behaviour was due to  $\text{Yb}^{3+}$  or  $\text{Er}^{3+}$ . Further work would be necessary involving samples with constant levels of  $\text{Yb}^{3+}$  and varying levels of  $\text{Er}^{3+}$  and vice versa. More work is also required to verify the evidence of self-trapping, principally involving more concentrations in the lower regime where an increase in lifetime is observed. If self-trapping is indeed occurring, then this would be the first observation of the effect in  $\text{Yb}^{3+}$ -doped silica-to the best of the author's knowledge.

### 7.1.3 Fluorescence lifetime in Pr-doped bulk glass

In chapter 6 the fluorescence lifetime of the 635 nm emission from the  $^3P_0$  excited state to the  $^3F_2$  excited state in praseodymium-doped fluoride glass was investigated. The results show that while there is a general decrease in the lifetime with dopant concentration, this decrease is strongly dependent on temperature. The rate of change in the lifetime is greater at higher temperatures. At concentrations below  $1.30 \times 10^{26}$  ions/m<sup>3</sup>, the lifetime increases with temperature while above  $1.30 \times 10^{26}$  ions/m<sup>3</sup>, the lifetime decreases with temperature. At  $1.30 \times 10^{26}$  ions/m<sup>3</sup>, the fluorescence lifetime would appear to be independent of temperature and does not change. This was not experimentally verified as there was no sample at this concentration available at the time.

It was found that the concentration-dependent energy transfer effects occurred with ions in the  $^3P_1$  excited state and the  $^1I_6$  state instead of ions in the  $^3P_0$  as previously thought. The natural decay rates for the  $^3P_1$  and  $^3P_0$  coupled excited states were found to be 14800 and 24500 s<sup>-1</sup> respectively.

## 7.2 Concentration Determination and Imaging

In this thesis, four fluorescence emissions were studied for three different rare earth dopants to assess the possibility of their use for determining and imaging their respective dopant concentrations using the lifetime technique. This technique requires that the relationship between the fluorescence lifetime and the dopant concentration must be monotonic. That is, for each value of the lifetime, there must be only one corresponding value for the concentration.

Of the four emissions studied, only the 635 nm fluorescence in Pr<sup>3+</sup>-doped ZBLAN glass was found suitable for imaging using the lifetime technique. There is a monotonic relationship between the fluorescence lifetime and concentration for all concentrations in the range studied. None of the two main emissions in Er<sup>3+</sup> was found to be suitable. The 1032 nm fluorescence lifetime in the Yb<sup>3+</sup>:Er<sup>3+</sup>-codoped sample

is clearly not suitable for use by this technique because of the quadratic behaviour with concentration.

In the case of the 1535 nm fluorescence in  $\text{Er}^{3+}$ , while the fluorescence lifetime exhibits monotonic behaviour with concentration, this behaviour is not well suited to concentration determination or imaging. The behaviour of the lifetime falls into two regimes. The lifetime is insensitive to concentration at concentrations below  $5 \times 10^{25}$  ions/ $\text{m}^3$  while decreasing with concentration at concentrations above  $5 \times 10^{25}$  ions/ $\text{m}^3$ . Many  $\text{Er}^{3+}$ -doped devices, such as fibre amplifiers, use concentrations that are typically much less than  $5 \times 10^{25}$  ions/ $\text{m}^3$ . In these devices, the use of lifetimes to measure concentration is of little practical use. Intensity-based imaging would be more suited for this emission where the fluorescence intensity is not affected by the cooperative energy transfer and is thus, directly related to the dopant concentration and pump power. Near-field microscopy could be used here to produce high-resolution intensity images of the dopant profile. In the high concentration regime, with applications such as fibre lasers, there is a monotonic decrease in the lifetime with concentration. However, the model shows that there is also a pump power dependence in the fluorescence lifetime arising from the 2-ion interaction. This would require careful transmission calibration of the imaging system and thus removes the inherent advantages of pure fluorescence lifetime imaging.

In conclusion, this work has shown that some transitions exhibit suitable lifetime characteristics and can be used for determining dopant concentration, while others do not. While only four transitions were investigated here, there are many other transitions that could also be investigated. For example,  $\text{Er}^{3+}$ -doped silica fibre also emits at 980 nm and 800 nm although these emissions are weak compared to the 1550 nm and 540 nm and their detection may not be easy.  $\text{Er}^{3+}$ -doped fluoride glass also emits at 2.7  $\mu\text{m}$ . In addition, each transition will vary in characteristic for different host compositions. For example, the behaviour of  $\text{Er}^{3+}$  in a glass host varies greatly with  $\text{Er}^{3+}$  doped in a crystal host. The addition of other dopants such as tin, aluminium and antimony can greatly influence the behaviour of the rare

earth dopants. But for those transitions that are found to be suitable, the use of the fluorescence lifetime can provide a simple, non-destructive method of determining and imaging dopant concentrations that is applicable to both optical fibre as well as bulk waveguides.

# Bibliography

- [1] D. N. Payne and J. P. Dakin. Emerging fibre technologies. In *OFS2000: 14<sup>th</sup> International Conference on Optical Fiber Sensors*, page We1, Giorgio Cini Foundation, Island of San Giorgio Maggiore, Venice, Italy, 2000.
- [2] E. Desurvire. *Erbium-Doped Fiber Amplifiers: Principles and Applications*. John Wiley & Sons Inc., 1994.
- [3] R. J. Mears, L. Reekie, I. M. Jauncey, and D. N. Payne. Low-noise erbium-doped fibre amplifier at 1.54  $\mu\text{m}$ . *Elect. Lett.*, 23(19):1026–1028, 1987.
- [4] E. Snitzer. Optical maser action in  $\text{Nd}^{3+}$  in barium crown glass. *Phys. Rev. Lett.*, 7:444–446, 1961.
- [5] A. Takada and H. Miyazawa. 30 GHz picosecond pulse generation from actively mode-locked erbium-doped fibre laser. *Elect. Lett.*, 26(3):216–217, 1990.
- [6] R. Armitage, R. Wyatt, B. J. Ainslie, and S. P. Craig-Ryan. Highly efficient 980 nm operation of an  $\text{Yb}^{3+}$ -doped silica fiber laser. *Elect. Lett.*, 1989.
- [7] S. D. Jackson and T. A. King. Efficient gain-switched operation of a Tm-doped silica fiber laser. *I.E.E.E. J. Quant. Electronics*, 34(5):779–789, 1998.
- [8] S. C. Goh, R. Pattie, C. Byrne, and D. Coulson. Blue and red laser action in  $\text{Nd}^{3+}:\text{Pr}^{3+}$  co-doped fluorozirconate glass. *Appl. Phys. Lett.*, 67(6):768–770, 1995.
- [9] M. C. Farries, P. R. Morkel, and J. E. Townsend. The properties of samarium fibre laser. In *Fiber laser sources and amplifiers.*, pages 271–278, Proc. SPIE 1171, 1991.
- [10] S. D. Jackson and T. A. King. CW operation of a 1.064 nm pumped Tm-Ho-doped silica fiber laser. *I.E.E.E. J. Quant. Electronics*, 34(9):1578–1587, 1998.
- [11] J. Y. Allain, M. Monerie, and H Poignant. Blue upconversion fluorozirconate fibre laser. *Elect. Lett.*, 26(3):166–186, 1990.
- [12] R. G. Smart, D. C. Hanna, A. C. Tropper, S.T. Davey, S. F. Carter, and D. Szebesta. CW room temperature upconversion lasing at blue, green and red wavelengths in infrared-pumped  $\text{Pr}^{3+}$ -doped fluoride fibre. *Elect. Lett.*, 27(14):1307–1309, 1991.
- [13] S. J. Matthews. Bright light from glass wires. *Laser Focus World*, 38(1):131–136, 2002.

- [14] V. Gapontsev and K. William. Fiber lasers grow in power. *Laser Focus World*, 38(8):83–87, 2002.
- [15] J. Connolly. New pump lasers power raman amplifiers. *WDM Solutions*, 3(6):57–62, June, 2001.
- [16] G. Monnom, B. Dussadier, E. Maurice, A. Saïssy, and D. B. Ostrowsky. Fluorescence and superfluorescence line narrowing and tunability of Nd<sup>3+</sup>-doped fibers. *I.E.E.E. J. Quant. Electronics*, 30(10):2361–2367, 1994.
- [17] H. C. Lefèvre. Fundamentals of the interferometric fiber-optic gyroscope. *Optical Review*, 4(1A):20–27, 1997.
- [18] J. Hecht. S-band amplification challenges developers. *Laser Focus World*, 38(7):79–84, 2002.
- [19] B. P. Petreski, M. M. Murphy, S. F. Collins, and D. J. Booth. Amplification in Pr<sup>3+</sup>-doped fluorozirconate optical fibre at 623.8 nm. *Elect. Lett.*, 29:1421–1423, 1993.
- [20] D. W. Hewak, J. A. Medeiros Neto, B. Sampson, R. S. Brown, and K. P. Jedrzejewski. Quantum-efficiency of praseodymium doped Ga:La:S glass for 1.3  $\mu\text{m}$  optical fibre amplifiers. *I.E.E.E. Photonics Tech. Lett.*, 6(5):609–612, 1994.
- [21] P. Cancio, P. Zeppini, P. De. Natale, S. Taccheo, and P. Laporta. Noise characteristics of a high-power ytterbium-doped fibre amplifier at 1083 nm. *Appl. Phys. B*, 70:763–768, 2000.
- [22] E. Rochat, K. Haroud, and R. Dändliker. High power Nd-doped fiber amplifier for coherent intersatellite links. *I.E.E.E. J. Quant. Electronics*, 35:1419–1423, 1999.
- [23] P. K. Y. Ko, S. Demokan, and H. Tam. Distributed temperature sensing with erbium-doped fiber amplifiers. *J. Lightwave Tech.*, 14(10):2236–2244, 1996.
- [24] G. W. Baxter, E. Maurice, and G. Monnom. Thermal variation of absorption in Yb<sup>3+</sup>-doped silica fibre for high temperature sensor applications. In *European Symposium on Optics for Environmental and Public Safety*, Munich, June 1995.
- [25] E. Maurice, G. Monnom, B. Dussardier, A. Saïssy, Ostrowsky D. B., and G. W. Baxter. Erbium-doped silica fibers for intrinsic fiber optic temperature sensors. *Appl. Opt.*, 34(34):8019–8025, 1995.
- [26] T. Sun, Z. Y. Zhang, K. T. V. Grattan, A. W. Palmer, and S. F. Collins. Temperature dependence of the fluorescence lifetime in Pr<sup>3+</sup>:ZBLAN glass for fiber optic thermometry. *Rev. Sci. Instrum.*, 68(9):3447–3451, 1997.
- [27] M. C. Farries, J. E. Townsend, and S. B. Poole. Very high rejection optical fibre filters. *Elect. Lett.*, 22:1126–1128, 1986.

- [28] R. I. Epstein, M. I. Buchwald, B. C. Edwards, Gosnell T. R., and Mungan C. E. Observation of laser-induced fluorescent cooling of a solid. *Nature*, 377:500–503, 1995.
- [29] T. R. Gosnell. Laser cooling of a solid by 65 K starting from room temperature. *Opt. Lett.*, 24:1041–1043, 1999.
- [30] B. C. Edwards, M. I. Buchwald, and R. I. Epstein. Development of the Los Alamos solid-state optical refrigerator. *Rev. Sci. Instrum.*, 69(5):2050–2055, 1998.
- [31] E. Rochat. *High power optical fiber amplifiers for coherent inter-satellite communication*. L'Université de Neuchâtel, Swiss, 2000.
- [32] E. Desurvire and J. R. Simpson. Amplification of spontaneous emission in erbium-doped single mode fibers. *J. Lightwave Tech.*, 7:835–845, 1989.
- [33] J. L. Wagener, P. F. Wysocki, M. J. F. Digonnet, H. J. Shaw, and D. J. DiGiovanni. Effect of concentration on the efficiency of erbium-doped silica fiber lasers. In *SPIE vol.1789 Fiber Sources and Amplifiers IV*, pages 80–88, 1992.
- [34] J. C. Martín. Erbium transversal distribution influence on the effectiveness of a doped fiber: optimization of its performance. *Opt. Comm.*, 194:331–339, 2001.
- [35] J. C. Martín, J. M. Alvarez, and M. A. Rebolledo. Erbium-doped fiber characterization by fluorescence dynamics measurement. *I.E.E.E. J. Quant. Electronics*, 10:1737–1741, 1996.
- [36] Th. Pfeiffer and H. Bülow. Analytical gain equation for erbium-doped fiber amplifiers including mode field profiles and dopant distribution. *I.E.E.E. Photonics Tech. Lett.*, 4(5):449–451, 1992.
- [37] M. N. Zervas, R. I. Laming, J. E. Townsend, and D. N. Payne. Design and fabrication of high gain-efficiency erbium-doped fiber amplifiers. *I.E.E.E. Photonics Tech. Lett.*, 4(12):1342–1344, 1992.
- [38] A. Soufiane, K. Dowling, and C. Houghton. New designs increase functionality of specialty fiber. *WDM Solutions*, 4(2):39–42, 2002.
- [39] M. Shimizu, M. Yamada, M. Horiguchi, and E. Sugita. Concentration effect on optical amplification characteristics of Er-doped silica single-mode fibers. *I.E.E.E. Photonics Tech. Lett.*, 2(1):43–45, 1990.
- [40] N. Kagi, A. Oyobe, and K. Nakamura. Gain characteristics of Er<sup>3+</sup>-doped fiber with a quasi-confined structure. *I.E.E.E. J. Lightwave Technology*, 8(9):1319–1322, 1990.
- [41] N. Kagi, A. Oyobe, and K. Nakamura. Temperature dependence of the gain in erbium-doped fibres. *I.E.E.E. J. Lightwave Technology*, 9(2):261–265, 1991.

- [42] W. L. Barnes, R. I. Laming, E. J. Tarbox, and P. R. Morkel. Absorption and emission cross-sections of  $\text{Er}^{3+}$ -doped silica fibers. *I.E.E.E. J. Quant. Electronics*, 27(4):1004–1009, 1991.
- [43] T. Kashiwada, M. Shigematsu, T. Kougo, H. Kanamori, and M. Nishimura. Erbium-doped fiber amplifier pumped at 1.48  $\mu\text{m}$  with extremely high efficiency. *I.E.E.E. Photonics Tech. Lett.*, 3(8):721–723, 1991.
- [44] B. J. Ainslie, S. P. Craig, S. T. Davey, and B. Wakefield. The fabrication assessment and optical properties of high-concentration  $\text{Nd}^{3+}$ -and  $\text{Er}^{3+}$ -doped silica fibres. *Material Lett.*, 6(5-6):139–144, 1988.
- [45] J. F. Marcerou, B. Jacquier, A. M. Brancion, J. C. Gacon, H. Fevrier, and J. Auge. Rare earth concentration and localization in  $\text{Nd}^{3+}$ -and  $\text{Er}^{3+}$ -doped fibre amplifiers. *J. Luminescence*, 45(1-6):108–110, 1990.
- [46] D. W. Oblas, M. P. Pink, F. and Singh, J. Connolly, D. Dugger, and T. Wei. In *Digest of Materials Research Society Annual Meeting*, page J6.3, MRS Pittsburgh, Pa, 1992.
- [47] A. Montaser, J. A. McLean, H. Liu, and J-M. Mermet. An introduction to icp spectrometries for elemental analysis. In A. Montaser, editor, *Inductively Couple Plasma Mass Spectrometry*. Wiley-VCH Inc., NY, 1998.
- [48] T. J. Manning and W. R. Grow. Inductively coupled plasma-atomic emission spectroscopy. *The Chemical Educator*, 2(1), 1997.
- [49] I. D. Aggarwal and G. Lu. *Fluoride glass fiber optics*. Academic Press Inc., CA, 1991.
- [50] G. E. Ice. *Methods in Material Research: A Current Protocols*. John Wiley & Sons Inc., NY, 2000.
- [51] S. Hayakawa, S. Tohno, K. Takagawa, A. Hamamoto, Nishida Y., M. Suzuki, Y. Sato, and Hirokawa T. Ultra trace characterization using an x-ray microprobe at spring-8 bl39xu. *Analytical Sciences*, 17 Supplement:i115–i117, 2001.
- [52] S. Inoué. Foundation of confocal scanned imaging in light microscopy. In J. B. Pawley, editor, *Handbook of biological confocal microscopy*. Plenum Press, NY, 1995.
- [53] S. T. Huntington, S. Ashby, J. D. Love, and M. Elias. Direct measurement and modeling of core dopant diffusion within fused biconical fibre couplers. In *24th Australian Conference on Optical Fibre Technology*, University of Sydney, Sydney, 1999.
- [54] M. Fornoni, A. Bulou, J. M. Breteau, J. Y. Gesland, and M. Rousseau. Neodymium concentration measurements in Nd:YLF laser rods: a nondestructive method. *Appl. Opt.*, 29(12):1758–1764, 1990.

- [55] S. Rogard, H. Bulou, A. Poignant, and M. Rousseau. Non-destructive concentration measurements of erbium-doped ZBLAN fluorozirconate glass. *Optical Materials*, 4:557–563, 1995.
- [56] A. Bulou, A. Coudreuse, M. Fornoni, M. Rousseau, A. Fornier, and H. Poignant. Non-destructive concentration measurements of rare earth ions in doped glasses. *J. Non-Cryst. Solids*, 161:231–234, 1993.
- [57] D. Uttamchandani, A. Othonos, A. T. Alavie, and M. Hubert. Determination of erbium distribution in optical fibers using confocal optical microscopy. *I.E.E.E. Photonics Tech. Lett.*, 6(3):437–439, 1994.
- [58] A. Othonos, J. Wheeldon, and M. Hubert. Determining erbium distribution in optical fibers using phase sensitive confocal microscopy. *Opt. Eng.*, 34(12):3451–3455, 1995.
- [59] B. P. Petreski, S. P. Schilders, P. M. Farrell, and M. Gu. Imaging concentration profiles of praseodymium-doped optical fibres. *Elect. Lett.*, 33(10):889–891, 1997.
- [60] B. P. Petreski, P. M. Farrell, and S. F. Collins. Cross-relaxation in praseodymium-doped fluorozirconate glass. *Opt. Comm.*, 132:89–93, 1996.
- [61] B. P. Petreski, S. P. Schilders, P. M. Farrell, and M. Gu. Determination of the concentration profile of praseodymium doped optical fibre by confocal microscopy. In *IQEC 96*, page J6.3, Sydney, 1996.
- [62] G. Nykolak, P. C. Becker, J. Shumlovich, Y. H. Wong, D. J. DiGiovanni, and A. J. Bruce. Concentration-dependent  $^4I_{13/2}$  lifetimes in  $\text{Er}^{3+}$ -doped fibers and  $\text{Er}^{3+}$ -doped planar waveguides. *I.E.E.E. Photonics Tech. Lett.*, 5(9):1014–1016, 1993.
- [63] M. D. Shinn, W. A. Sibley, M. G. Drexhage, and R. N. Brown. Optical transitions of  $\text{Er}^{3+}$  ions in fluorozirconate glass. *Phys. Rev. B*, 27(11):6635–6648, 1993.
- [64] J. G. Edwards and J. N. Sandoe. A theoretical study of the Nd:Yb:Er glass laser. *J. Phys. D*, 7:1078–1095, 1974.
- [65] P. Laporta, S. Longhi, S. Taccheo, and O. Svelto. Analysis and modeling of the erbium-ytterbium glass laser. *Opt. Comm.*, 100:311–321, 1993.
- [66] O. Barbosa-Garcia, E. Jonguitud-Isurieta, L. A. Diaz-Torres, and C. W. Struck. The non-radiative energy transfer in high acceptor concentration codoped Nd,Ho:YAG and Nd:Er:YAG. *Opt. Comm.*, 129:273–283, 1996.
- [67] S. K. Sekatskii and V. S. Letokhov. Scanning optical microscopy with nanometer spatial resolution based on resonance excitation of fluorescence from one-atom excited center. *JETP Lett.*, 63(5):319–323, 1996.

- [68] P. Wu and L. Brandt. Resonance energy transfer: methods and applications. *Anal. Biochem.*, 218:1–13, 1994.
- [69] A. Draaijer, R. Sanders, and H. C. Gerrisen. Fluorescence lifetime imaging, a new tool in confocal microscopy. In J. B. Pawley, editor, *Handbook of biological confocal microscopy*. Plenum Press, New York, 1995.
- [70] D. I. Pattison, A. J. MacRobert, A. D. Waite, D. Phillips, K. Henbest, A. W. Parker, C. De. Lara, and P. O'Neill. *A study of the subcellular localisation of photosensitisers in V79/4 fibroblasts and model systems by time-resolved fluorescence microscopy*. Central Laser Facility Annual Report 1997/1998, Rutherford Appleton Laboratory, Oxfordshire, 1998.
- [71] O. Holub, M. J. Seufferheld, C. Gohlke, and R. M. Clegg. Fluorescence lifetime imaging (FLI) in real-time- a new technique in photosynthesis research. *Photosynthetica*, 38(4):581–599, 2000.
- [72] S. Murata, P. Herman, and J. R. Lakowicz. Texture analysis of fluorescence lifetime images of nuclear DNA with effect of fluorescence resonance energy transfer. *Cytometry*, 43:94–100, 2001.
- [73] G. J. Dixon. Time-resolved spectroscopy defines biological molecules. *Laser Focus World*, 33(10):115–121, 1997.
- [74] K. Dowling, M. J. Dayel, M. J. Lever, P. M. W. French, J. D. Hares, and A. K. L. Dymoke-Bradshaw. Fluorescence lifetime imaging with picosecond resolution for biomedical applications. *Opt. Lett.*, 23(10):810–812, 1998.
- [75] S. E. D. Webb, Y. Gu, S. L ev eque-Fort, J. Siegel, M. J. Cole, K. Dowling, R. Jones, P. M. W. French, M. A. A. Neil, R. Juškaitis, L. O. D. Sucharov, T. Wilson, and M. J. Lever. A wide-field time-domain fluorescence lifetime imaging microscope with optical sectioning. *Rev. Sci. Instrum.*, 73(4):1898–1907, 2002.
- [76] T. Wilson. The role of the pinhole in confocal imaging system. In J. B. Pawley, editor, *Handbook of biological confocal microscopy*. Plenum Press, New York, 1995.
- [77] R. C. Dunn, G. R. Holtom, L. Mets, and X. S. Xie. Near-field fluorescence imaging and fluorescence lifetime measurement of light harvesting complexes in intact photosynthesis membranes. *J. Phys. Chem.*, 98(12):3094–3098, 1994.
- [78] M. B ohmer, F. Pampaloni, M. Wahl, H. Rahn, R. Erdmann, and J. Enderlein. Time-resolved confocal scanning device for ultrasensitive fluorescence detection. *Rev. Sci. Instrum.*, 72(11):4145–4152, 2001.
- [79] In J. Pawley, editor, *Handbook of biological confocal microscopy*. Plenum Press, New York, 1995.
- [80] S. Sudo. Outline of optical fibre amplifiers. In S. Sudo, editor, *Optical Fiber Amplifiers: Materials, devices and Applications*. Artech House Inc., MA, 1997.

- [81] W. J. Miniscalco. Optical and electronic properties of rare earth ions in glasses. In M. J. F. Digonet, editor, *Rare Earth Doped Fiber Lasers and Amplifiers: 2nd Ed, revised and Expanded*. Marcel Dekker Inc., NY, 2001.
- [82] C. P. Flynn and M. B. Salamon. Single-crystal nonstructures. In K. A. Gscheidner Jr. and L. Eyring, editors, *Handbook on the physics and chemistry of rare earths. Vol 22*. Elsevier, Science B. V., The Netherlands, 1996.
- [83] E. Desurvire. Erbium-doped fiber amplifier: Basic physics and characteristics. In M. J. Digonet, editor, *Rare earth doped fiber amplifiers*. Marcel Dekker Inc., New York, 1993.
- [84] Y. W. Lee and B. Lee. High resolution cryogenic optical fiber sensor system using erbium-doped fiber. *Sensors and Actuators A*, 96:25–27, 2002.
- [85] R. Reisfeld and C. K. Jörgensen. Excited state phenomena in vitreous materials. In K.A. Gschneidner and L. Eyring, editors, *Handbook on the Physics and Chemistry of Rare Earths*. Elsevier, Amsterdam, 1987.
- [86] T. Tellert, F. D. Di Pasquale, and M. Federighi. Theoretical analysis of the dynamic behavior of highly efficient erbium/ytterbium codoped fiber lasers. *I.E.E.E. Photonics Tech. Lett.*, 8(11):1462–1464, 1996.
- [87] F. Gan, J. Wang, and Y Chen. UV upconversion luminescence of Nd<sup>3+</sup> and Er<sup>3+</sup> ions in fluorozirconate glasses. *J. Non-Cryst. Solids*, 231& 214:261–265, 1997.
- [88] T. Sandrock, A. Dening, and G. Huber. Laser emission of erbium-doped fluoride bulk glasses in the spectral range from 2.7 to 2.8  $\mu\text{m}$ . *Opt. Lett.*, 24(6):382–384, 1999.
- [89] B. Moine, A. Brenier, and C. Pedrini. Fluorescence dynamics of Er<sup>3+</sup> and ions and energy transfer in some fluoride glasses. *I.E.E.E. J. Quant. Electronics*, 25(1):88, 1989.
- [90] T. B. Nguyen, S. Trpkovski, P. M. Farrell, G. W. Baxter, and S. F. Collins. Dependence of the fluorescence lifetime on dopant concentration and temperature in praseodymium doped fluoride glass. *Opt. Comm.*, 186:277–281, 2000.
- [91] L. B. Shaw, B. B. Harbison, B. Cole, J. S. Sanghera, and I. D. Aggarwal. Spectroscopy of the IR transitions in Pe<sup>3+</sup>-doped heavy metal selenide glasses. *Optics Express*, 1(4):87–96, 1997.
- [92] J. Y. Allain, M. Monerie, and H Poignant. Tunable cw lasing around 610, 635, 695, 715, 885 and 910 in praseodymium-doped fluorozirconate fibre. *Elect. Lett.*, 27(3):189–191, 1991.
- [93] Y. Shi and O. Poulsen. High-power broadband singlemode Pr<sup>3+</sup>-doped fibre superfluorescence light source. *Elect. Lett.*, 29:1945–1946, 1993.

- [94] S. Tanabe, K. Taku, and T. Hanada. Energy transfer in 1.3  $\mu\text{m}$  emission in Pr-Yb codoped tellurite glasses. *J. Non-Cryst. Solids*, 274:55–61, 2000.
- [95] A. C. Tropper, J. N. Carter, R. D. T. Lauder, D. C. Hanna, S. T. Davey, and D. Szebesta. Analysis of blue and red laser performance of the infrared-pumped praseodymium-doped fiber laser. *J. Opt. Soc. Am. B*, 11(5):886–893, 1994.
- [96] E. Maurice, G. Monnom, G.W. Baxter, S.A. Wade, B.P. Petreski, and S.F. Collins. Blue LED-pumped point temperature sensor based on the fluorescence intensity ratio in  $\text{Pr}^{3+}$ :ZBLAN glass. *Optical Review*, 4(1A):89–91, 1997.
- [97] Y. Nishida, M. Yamada, T. Kanamori, K. Kobayashi, J. Temmyo, S. Sudo, and Y. Ohishi. Development of an efficient praseodymium-doped fiber amplifier. *I.E.E.E. J. Quant. Electronics*, 34(8):1332–1339, 1998.
- [98] S. T. Davey and P. W. France. Rare earth-doped fluoro-zirconate glass for fiber devices. *Br. Telecommun. Technol. J.*, 7:58, 1988.
- [99] E. Maurice, S. A. Wade, S. F. Collins, G. Monnom, and G. W. Baxter. A self-referenced point temperature sensor based on a fluorescence intensity ratio in  $\text{Yb}^{3+}$ -doped silica fibre. *Appl. Opt.*, 36:8264–8269, 1997.
- [100] M. J. F. Digonnet. Broadband fiber sources. In M. J. Digonnet, editor, *Rare earth doped fiber amplifiers, 2nd Ed.* Marcel Dekker Inc., New York, 2001.
- [101] S. A. Wade, S. F. Collins, and Baxter. Fluorescence intensity ratio technique for optical fiber point temperature sensing. *J. Appl. Phys.*, 94(8):in press, 2003.
- [102] S. Dai, J. Yang, L. Wen, L. Hu, and Z. Jiang. Effect of radiative trapping on measurement of the spectroscopic properties of  $\text{Yb}^{3+}$ :phosphate glasses. *J. Luminescence*, 104:55–63, 2003.
- [103] G. W. Baxter, G. Monnom, and E. Maurice. Thermal variation of absorption in  $\text{Yb}^{3+}$ -doped silica fibre for high temperature sensor applications. In *European Symposium on Optics for Environmental and Public Safety*, Munich, June 1995.
- [104] M. Poulain. Fluoride glass composition and processing. In I. D. Aggarwal and G. Lu, editors, *Fluoride glass fiber optics*. Academic Press, CA, 1991.
- [105] P. W. France. *Fluoride glass optical fibres*. Blackie & Son, London, 1990.
- [106] J. R. Simpson. Rare earth doped fiber fabrication: Techniques and physical properties. In M. J. Digonnet, editor, *Rare earth doped fiber amplifiers*. Marcel Dekker Inc., New York, 1993.
- [107] A. Bjarklev. *Optical Fiber Amplifiers: Design and System Applications*. Artech House Inc., MA, 1993.

- [108] S. Takahashi and H. Iwasaki. Preform and fiber fabrication. In I. D. Aggarwal and G. Lu, editors, *Fluoride glass fiber optics*. Academic Press, CA, 1991.
- [109] Y. Kimura. Rare-earth-doped fibre fabrication methods. In S. Shimida and H. Ishio, editors, *Optical Amplifiers and their Applications*. John Wiley and Sons, England, 1994.
- [110] K. Patek. *Glass lasers*. Butterworth, London, 1970.
- [111] I. Camlibel, D. A. Pinnow, and F. W. Dabby. *Appl. Phys. Lett.*, 26(186), 1975.
- [112] E. Desurvire. Basic physics and theoretical modeling. *Int. J. High Speed Electronics*, 2(1,2):89–114, 1991.
- [113] G. Monnom. *Private communication*. Laboratoire de Physique de la Matière Condensée, Nice, France, 1999.
- [114] P. Blixt, J. Nilsson, T. Carlнас, and B. Jaskorzynska. Concentration-dependent upconversion in  $\text{Er}^{3+}$ -doped fiber amplifiers: experiments and modeling. *I.E.E.E. Transactions Photonics Tech. Lett.*, 3(11):996–998, 1991.
- [115] T. B. Nguyen, G. Koltovski, G. W. Baxter, P. M. Farrell, and A. Roberts. Determination of the concentration profile of rare earth-dopants in optical fibres. In *AOS99 - The Australian Optical Society Annual Conference*, University of Sydney, Sydney, 1999.
- [116] T. B. Nguyen, G. W. Baxter, and P. M. Farrell. Modelling of the fluorescence lifetime dependence on concentration in rare earth-doped optical fibres. In *Proc. SCIRF'99- Collaborative Research Forum*, Victoria University of Technology, Melbourne, 1999.
- [117] B.-C. Hwang, S. Jiang, T. Luo, J. Watson, G. Sorbello, and N. Peyghambarian. Cooperative upconversion and energy transfer of new high  $\text{Er}^{3+}$ - and  $\text{Yb}^{3+}$ - $\text{Er}^{3+}$ -doped phosphate glasses. *J. Opt. Soc. Am. B*, 17(5):833–839, 2000.
- [118] M. K. Davis, M. J. F. Digonnet, and R. H. Pantell. Characterization of clusters in rare earth-doped fibers by transmission measurements. *I.E.E.E. J. Lightwave Technology*, 13(2):120–126, 1995.
- [119] P. F. Wysocki. Erbium-doped fiber amplifiers: Advanced topics. In M. J. Digonnet, editor, *Rare earth doped fiber amplifiers, 2nd Ed.* Marcel Dekker Inc., New York, 2001.
- [120] E. Develaque, T. Georges, M. Monerie, P. Mamouler, and J. F. Bayon. Modeling of pair-induced quenching in erbium-doped silicate fibers. *I.E.E.E. Photonics Tech. Lett.*, 5(1):73–75, 1993.
- [121] E. Maurice, G. Monnom, B. Dussardier, and D. B. Ostrowsky. Clustering-induced nonsaturable absorption phenomenon in heavily erbium-doped silica fibers. *Opt. Lett.*, 20(24):2487–2489, 1995.

- [122] R. S. Quimby, W. J. Miniscalco, and B. Thompson. Quantitative characterization of clustering in erbium-doped silica glass fibers. In *SPIE vol.2073 Fiber Laser Sources and Amplifiers V*, pages 2–12, 1993.
- [123] M. P. Hehlen, N. J. Cockroft, T. R. Gosnell, A. J. Bruce, G. Nykolak, and J. Shmulovich. Uniform upconversion in high-concentration  $\text{Er}^{3+}$ -doped soda lime silicate and aluminosilicate glasses. *Opt. Lett.*, 22(11):772–774, 1997.
- [124] E. Snoeks, G. N. van den Hoven, A. Polman, B. Hendriksen, M. B. J. Diemeer, and F. Priolo. Cooperative upconversion in erbium-implanted soda-lime silicate glass waveguides. *J. Opt. Soc. Am. B*, 12:1468–1474, 1995.
- [125] G. N. van den Hoven, E. Snoeks, A. Polman, C. van Dam, J. W. M. van Uffelen, and M. K. Smit. Upconversion in Er-implanted  $\text{Al}_2\text{O}_3$  waveguides. *J. Appl. Phys.*, 79(3):1258–1266, 1996.
- [126] P. G. Kik and A. Polman. Cooperative upconversion as the gain-limiting factor in Er doped miniature  $\text{Al}_2\text{O}_3$  optical waveguide amplifiers. *Optics Express*, 10(16):832–839, 2002.
- [127] M. G. Sceats, P. A. Krug, G. R. Atkins, S.C. Guy, and S. B. Poole. Nonlinear excited state absorption in  $\text{Er}^{3+}$  doped fiber with high power 980 nm pumping. In *Proc. 2nd Top. Meet. Opt. Amplifiers Appl.*, pages 48–51, Snowmass Village, CO, 1991.
- [128] J. L. Philipsen, J. Broeng, A. Bjarklev, S. Helmfrid, D. Bremberg, B. Jaskorzynska, and B. Pálsdóttir. Observation of strongly nonquadratic homogeneous upconversion in  $\text{Er}^{3+}$ -doped silica fibers and reevaluation of the degree of clustering. *I.E.E.E. J. Quant. Electronics*, 35(11):1741–1749, 1999.
- [129] Z. Burshtein, Y. Kalisky, S. Z. Levy, P. Le Boulanger, and S. Rotman. Impurity local phonon nonradiative quenching in  $\text{Yb}^{3+}$  fluorescence in ytterbium-doped silicate glasses. *I.E.E.E. J. Quant. Electronics*, 36(8):1000–1007, 2000.
- [130] W. L. Barnes, S. B. Poole, J. E. Townsend, L. Reekie, D. J. Taylor, and D. N. Payne.  $\text{Er}^{3+}$ - $\text{Yb}^{3+}$  and  $\text{Er}^{3+}$  doped fiber lasers. *J. Lightwave Tech.*, 7(10):1461–1465, 1989.
- [131] S. Tanabe, K. Touda, and T. Hanada. Excited energy migration and fluorescence decay in yb-doped and yb/pr-codoped tellurite glasses. *Optical Materials*, 12:35–40, 1999.
- [132] Y. Mita, T. Ide, M. Togashi, and H. Yamamoto. Energy transfer processes in  $\text{Yb}^{3+}$  and  $\text{Tm}^{3+}$  ion-doped fluoride crystals. *J. Appl. Phys.*, 85(8):4160–4164, 1999.
- [133] A. V. Kir'yanov, V. Aboites, A. M. Belovolov, M. I. Timoshechkin, M. J. Damzen, and A. Minassian. Powerful visible (530–770 nm) luminescence in  $\text{Yb,Ho:GGG}$  with IR diode pumping. *Optics Express*, 10(16):832–839, 2002.

- [134] Y. G. Choi, K. H. Kim, Y. S. Han, and J. Heo. Sensitizing effect of  $\text{Yb}^{3+}$  on near-infrared fluorescence emission of  $\text{Cr}^{4+}$ -doped calcium aluminate glasses. *J. Materials Research*, 15(2):278–281, 2000.
- [135] R. Valiente, O. S. Wenger, and H. U. Güdel. Near-infrared-to-visible photon upconversion process induced by exchange interactions in  $\text{Yb}^{3+}$ -doped  $\text{RbMnCl}_3$ . *Phys. Rev. B*, 63(16):165102/1–11, 2001.
- [136] M. P. Hehlen, N. J. Cockroft, and T. R. Gosnell. Spectroscopic properties of  $\text{Er}^{3+}$ - and  $\text{Yb}^{3+}$ -doped soda-lime silicate and aluminosilicate glasses. *Phys. Rev. B*, 56(15):9302–9318, 1997.
- [137] C. Wyss, W. Lüthy, Weber H. P., Rogin P., and Hulliger J. Energy transfer in  $\text{Yb}^{3+}:\text{Er}^{3+}:\text{YLF}$ . *Opt. Comm.*, 144:31–35, 1997.
- [138] P. Peterka, J. Kanka, M. Karsek, P. Honztko, and F. Abdelmalek. Characterisation and modelling of Er/Yb codoped fibres. In M. Hrabovsk, P. Tomnek, and M. Miler, editors, *Photonics Devices and Systems*. Proceedings of SPIE, vol. 4016, 2000.
- [139] P. S. Golding, S. D. Jackson, T. A. King, and M. Pollnau. Energy transfer processes in  $\text{Er}^{3+}$ ,  $\text{Pr}^{3+}$ -codoped zblan glasses. *Phys. Rev. B*, 62(2):856–864, 2000.
- [140] M. Federighi and F. Di Pasquale. The effect of pair-induced energy transfer on the performance of silica waveguide amplifiers with high  $\text{Er}^{3+}/\text{Yb}^{3+}$  concentrations. *I.E.E.E. Photonics Tech. Lett.*, 7(3):303–305, 1995.
- [141] T. B. Nguyen. *Investigation of optically induced cooling of ytterbium-doped optical fibres using a laser*. Honours Thesis, Victoria University, Melbourne, Australia, 1998.
- [142] D. S. Sumida and T. Y. Fan. Effects of radiation trapping on fluorescence lifetime and emission cross section measurements in solid-state laser media. *Opt. Lett.*, 19(17):1343–1345, 1994.
- [143] M. J. Weber, J. E. Lynch, D. H. Blackburn, and D. J. Cronin. Dependence of the stimulated emission cross section of  $\text{Yb}^{3+}$  on host glass composition. *I.E.E.E. J. Quant. Electronics*, QE-19(10):1600–1608, 1983.
- [144] R. Paschotta, J. Nilsson, P. R. Barber, J. E. Caplen, A. C. Tropper, and D. C. Hanna. Lifetime quenching in yb-doped fibres. *Opt. Comm.*, 136(5-6):375–378, 1997.
- [145] G. S. Maciel, A. Biswas, R. Kapoor, and P. N. Prasad. Blue cooperative upconversion in  $\text{Yb}^{3+}$ -doped multicomponent sol-gel-processed silica glass for three-dimensional display. *Appl. Phys. Lett.*, 76(15):1978–1980, 2000.
- [146] E. Montoya, O. Espero, and L. E. Bausa. Cooperative luminescence in  $\text{Yb}^{3+}:\text{LiNbO}_3$ . *J. Luminescence*, 87-89:1036–1038, 2000.

- [147] M. A. Noginov, G. B. Loutts, C. S. Steward, B. D. Lucas, D. Fider, V. Peters, E. Mix, and G. Huber. Spectroscopic study of Yb doped oxide crystals for intrinsic optical bistability. *J. Luminescence*, 96:129–140, 2002.
- [148] P. Urquhart. Praseodymium-doped fiber amplifiers: Theory of 1.3  $\mu\text{m}$  operation. *I.E.E.E. J. Quant. Electronics*, 28(10):1962–1965, 1992.
- [149] B. P. Petreski, P. M. Farrell, and S. F. Collins. Optical amplification on the  $^3p_0 \rightarrow ^3f_2$  transition in praseodymium-doped fluorozirconate fiber. *Fiber and Integrated Optics*, 18(1):21–32, 1999.
- [150] J.S. Sanghera and I.D. Aggarwal. Rare earth doped heavy-metal fluoride glass fibers. In M.J. Digonnet, editor, *Rare Earth Doped Fiber Lasers and Amplifiers*. Marcel Dekker Inc., New York, 1993.
- [151] Y. Zhao, S. Fleming, and S. Poole. 22 mW blue output power from a  $\text{Pr}^{3+}$  fluoride fibre upconversion laser. *Opt. Comm.*, 114(3-4):285–288, 1995.
- [152] S. F. Collins, G. W. Baxter, S. A. Wade, and P. M. Farrell. Strain dependence of fluorescence from rare-earth-doped optical fibres: application to the simultaneous, co-located, measurement of strain and temperature. *Composite Structures*, 58:373–379, 2002.
- [153] H. Zellmer, K. Plamann, G. Huber, H. Schiefe, and A. Tünnermann. Visible double-clad upconversion fibre laser. *Elect. Lett.*, 34(6):565–567, 1998.
- [154] H. Zellmer, P. Riedel, and A. Tünnermann. Visible upconversion lasers in praseodymium-ytterbium-doped fibers. *Appl. Phys. B*, 69:417–421, 1999.
- [155] R. Balda, J. Fernández, A. Mendioroz, and M. Voda. Influence of ytterbium on the infrared to visible upconversion in Praseodymium codoped potassium lead chloride crystal. In *The ElectroChemnica Society-203rd Meeting*, Paris, France, April 27 - May 2, 2003.
- [156] I. R. Mitchell, P. M. Farrell, G. W. Baxter, S. F. Collins, K. T. V. Grattan, and T. Sun. Analysis of dopant concentration effects in praseodymium-based fluorescent fiber optic temperature sensors. *Rev. Sci. Instrum.*, 71(1):100–103, 2000.
- [157] H. Jagannath, A. Sivaram, D. Ramachandra Rao, and P. Venkateswarku. Radiative decay rates in  $\text{F}_2\text{O}:\text{Dy}^{3+}$ . *Chem. Phys. Lett.*, 63(1):90–96, 1979.
- [158] B. P. Petreski. *Ph.D. Thesis: Characterisation of optical fibre amplifiers: amplifiers for the 632.8 nm HeNe wavelegnth in praseodymium-doped ZBLAN*. Victoria University of Technology, Melbourne, Australia, 1997.
- [159] Z. Y. Zhang, K. T. V. Grattan, A. W. Palmer, B. T. Meggitt, and T. Sun. Fluorescence decay-time characteristics of erbium-doped optical fiber at elevated temperatures. *Rev. Sci. Instrum.*, 68(7):2764–2766, 1997.

- [160] T. Sun, Z. Y. Zhang, Grattan K. T. V., and A. Palmer. Intrinsic doped fluorescence decay-time based measurements- strain and temperature characteristics for sensor purposes. *Rev. Sci. Instrum.*, 69(12):4186–4190, 1998.
- [161] T. Sun, Z. Y. Zhang, Grattan K. T. V., and A. Palmer. Intrinsic strain and temperature characteristics of Yb-doped silica-based optical fibers. *Rev. Sci. Instrum.*, 70(2):1447–1451, 1999.

# Appendix A

## Publications

During the course of this project, a number of public presentations have been made by the author which are based on, or related to the work presented in this thesis. They are listed here for reference.

### A.1 Regular Journal Publications

- Thinh B. Nguyen, Steven Trpkovski, Peter M. Farrell, Greg W. Baxter and Stephen F. Collins. Dependence of the fluorescence lifetime on dopant concentration and temperature in praseodymium doped fluoride glass. *Optics Communications*, **186**:277-281, 2000.

### A.2 International Conference Proceedings

- D. Simpson, T. Nguyen, G. Baxter, S. Collins, B. Faure, W. Blanc, B. Dusardier, G. Monnom, P. Peterka. Thulium-doped silica fiber for S-band amplifiers: pump power and host composition effect on the  $^3H_4 \rightarrow ^3F_4$  band. Accepted into *EPS-QEOD Europhoton Conference on "Solid state and fiber coherent light sources"*, Lausanne, Switzerland, August 29 - September 3, 2004.
- Cristina Vergara, Scott Wade, Thinh Nguyen, Peter Farrell, Stephen Collins and Greg Baxter. Optimising the performance of optical temperature sensors. *SPIE's 2000 Symposium on Smart Materials and MEMS*, Sheraton Towers Southgate, Melbourne, 13-15 December 2000.
- Thinh B. Nguyen, Steven Trpkovski, Peter M. Farrell, Greg W. Baxter, Stephen F. Collins. The concentration dependence in  $Pr^{3+}$ :ZBLAN optical fibre temperature sensors. *OFS2000, 14<sup>th</sup> International Conference on Optical Fiber Sensors*, Giorgio Cini Foundation, Island of San Giorgio Maggiore, Venice, Italy, 11-13, October 2000.
- Steven Trpkovski, Thinh B. Nguyen, Peter M. Farrell, Greg W. Baxter, Stephen F. Collins. Temperature and concentration dependence of the lifetime of a Praseodymium excited state in Fluorozirconate glass. *CLEO/Europe 2000*, Nice Acropolis, Nice, France, 10-15 September 2000.

### A.3 Australian Conference Proceedings

- Vince C. Vella, Thinh B. Nguyen, Greg W. Baxter, Stephen F. Collins, Peter J. Newman, Douglas R. MacFarlane. Prediction of temperature independence in fluorescence lifetime of praseodymium-doped glass. Accepted into *AOS04 - 17<sup>th</sup> Conference of the Australian Optical Society*, Australian National University, Canberra, 7-8 July. 2004.
- Thinh B. Nguyen, Greg W. Baxter, Peter M. Farrell, Gérard Monnom. Dependence of the fluorescence lifetime on dopant concentration and pump power in erbium-doped optical fibres. *Australian Institute of Physics 15th Biennial Congress 2002*, Darling Harbour Convention Centre, Sydney, 8-11 Jul. 2002.
- Thinh B. Nguyen, Steven Trpkovski, Peter Corbett, Greg W. Baxter. Determination of erbium dopant concentration in erbium-ytterbium codoped fibres. *ACOLS2001, Australian Conference on Optics, Lasers and Spectroscopy*, University of Queensland, Brisbane, 3-6 Dec. 2001.
- S. Trpkovski, T. B. Nguyen, S. F. Collins, P. M. Farrell, G. W. Baxter, S. A. Wade. Strain and Temperature Measurement using a Combined Fluorescence Intensity Ratio and Fibre Bragg Grating Technique. *ACOLS2001, Australian Conference on Optics, Lasers and Spectroscopy*, University of Queensland, Brisbane, 3-6 Dec. 2001.
- T. B. Nguyen, G. W. Baxter, S. F. Collins and P. M. Farrell. Fluorescence decay rate, temperature and praseodymium concentration in fluoride glasses. *AOS2000 - 13<sup>th</sup> Conference of the Australian Optical Society*, University of Adelaide, Adelaide, 10-15 Dec. 2000.
- Thinh B. Nguyen, Steven Trpkovski, Peter M. Farrell, Greg W. Baxter, Stephen F. Collins. Concentration and temperature dependence of the fluorescence lifetime of  $\text{Pr}^{3+}:\text{ZBLAN}$ . *ACOPT2000, 25th Australian Conference on Optical Fibre Technology*, Australian National University, Canberra, 26-28 June 2000.
- T. B. Nguyen, G. Koltovski, G. W. Baxter, P. W. Farrell, A. Roberts. Determination of the concentration profile of rare earth-dopants in optical fibres. *AOS'99, The Australian Optical Society Annual Conference*, University of Sydney, Sydney, 4-9 July 1999.

### A.4 Others

- Thinh B. Nguyen, Greg W. Baxter and Peter M. Farrell. Modelling of the fluorescence lifetime dependence on concentration in rare earth-doped optical fibres. *Proc. SCIRF'99*, ed. J. Singh, Victoria University of Technology, 18 Nov. 1999.

## Appendix B

# List of Abbreviations

Abbreviaton	Meaning
Al	aluminium
AOM	acousto-optic modulator
ASE	amplified spontaneous emission
Ce	cerium
CET	cooperative energy transfer
CFUC	cooperative frequency up-conversion
CRO	cathode ray oscilloscope
CVD	chemical vapour deposition
DB	dichroic beamsplitter
Dy	dysprosium
EDF	erbium-doped fibre
EDFA	erbium-doped fibre amplifier
EPMA	electron probe microanalysis
Er	erbium
ESA	excited state absorption
Eu	europium
FWHM	full width at half maximum
Gd	gadolinium
Ge	germanium
GPIB	general purpose interface bus
Ho	holmium
ICP	inductively couple plasma
ICP-AES	inductively couple plasma atomic emission spectroscopy
ICP-MS	Inductively coupled plasma mass spectroscopy
InGaAs	indium gallium arsenide
La	lanthanum
LPMC	Laboratoire de Physique de la Matiere Condensee
LSM	laser scanning microscopy
Lu	lutetium
MCVD	modified chemical vapour deposition
MO	microscope objective
MRT	modified rod in tube
NA	numerical aperture
NAA	neutron activation analysis
Nd	neodymium
nm	nanometer
ns	nanoseconds

NSA	non-saturable absorption
O <sub>2</sub>	oxygen
OVD	outside vapour deposition
P	phosphorus
Pm	promethium
PMT	photomultiplier tube
ppm	parts per million
Pr	praseodymium
REM	resonant energy migration
RT	rod in tube
SIMS	secondary ion mass spectroscopy
Sm	samarium
SNOM	scanning near-field optical microscopy
Tb	terbium
Tm	thulium
μm	micrometer
UV	ultra-violet
VAD	vapour axial deposition
XMS	x-ray microprobe spectroscopy
YAG	yttrium aluminium garnet
Yb	ytterbium
YDF	ytterbium-doped fibre
ZBLAN	ZrF <sub>4</sub> -BaF <sub>2</sub> -LaF <sub>3</sub> -AlF <sub>3</sub> -NaF fluoride glass